LYSOZYME PATTERN FORMATION IN EVAPORATING DROPLETS

by

Heather Meloy Gorr

B.A., Penn State University, 2006

M.S., Indiana University of Pennsylvania, 2008

Submitted to the Graduate Faculty of

Swanson School of Engineering in partial fulfillment

of the requirements for the degree of

Doctor of Philosophy

University of Pittsburgh

2013

UNIVERSITY OF PITTSBURGH

SWANSON SCHOOL OF ENGINEERING

This dissertation was presented

by

Heather Meloy Gorr

It was defended on

February 5, 2013

and approved by

Jung-Kun Lee, PhD, Assistant Professor, Department of Mechanical Engineering and Materials Science

Ian Nettleship, PhD, Associate Professor, Department of Mechanical Engineering and Materials Science

Sachin Velankar, PhD, Associate Professor, Chemical and Petroleum Engineering

Dissertation Director: John A. Barnard, PhD, Professor, Department of Mechanical Engineering and Materials Science

LYSOZYME PATTERN FORMATION IN EVAPORATING DROPLETS

Heather Meloy Gorr, PhD

University of Pittsburgh, 2013

Liquid droplets containing suspended particles deposited on a solid, flat surface generally form ring-like structures due to the redistribution of solute during evaporation (the "coffee ring effect"). The forms of the deposited patterns depend on complex interactions between solute(s), solvent, and substrate in a rapidly changing, far from equilibrium system. Solute self-organization during evaporation of colloidal sessile droplets has attracted the attention of researchers over the past few decades due to a variety of technological applications. Recently, pattern formation during evaporation of various biofluids has been studied due to potential applications in medical screening and diagnosis. Due to the complexity of 'real' biological fluids and other multicomponent systems, a comprehensive understanding of pattern formation during droplet evaporation of these fluids is lacking.

In this PhD dissertation, the morphology of the patterns remaining after evaporation of droplets of a simplified model biological fluid (aqueous lysozyme solutions + NaCl) are examined by atomic force microscopy (AFM) and optical microscopy. Lysozyme is a globular protein found in high concentration, for example, in human tears and saliva. The drop diameters, D, studied range from the micro- to the macro- scale (1 μm – 2 mm).

In this work, the effect of evaporation conditions, solution chemistry, and heat transfer within the droplet on pattern formation is examined. In micro-scale deposits of aqueous lysozyme solutions (1 μm < D < 50 μm), the protein motion and the resulting dried residue

morphology are highly influenced by the decreased evaporation time of the drop. The effect of electrolytes on pattern formation is also investigated by adding varying concentrations NaCl to the lysozyme solutions. Finally, a novel pattern recognition program is described and implemented which classifies deposit images by their solution chemistries.

The results presented in this PhD dissertation provide insight into the evaporative behavior and pattern formation in droplets of simplified model biological fluids (aqueous lysozyme + NaCl). The patterns that form depend sensitively on the evaporation conditions, characteristic time and length scales, and the physiochemical properties of the solutions. The patterns are unique, dependent on solution chemistry, and may therefore act as a "fingerprint" in identifying fluid properties.

TABLE OF CONTENTS

LIST OF TABLES

LIST OF FIGURES

NOMENCLATURE

A	Surface area, m^2
Bo	Bond number, $Bo = \frac{\rho_L g R h_0}{\gamma_{LV}}$
c	Vapor concentration
c_p	Heat capacity, 4180 ($J\ kg^{-1}\ K^{-1}$)
c_V	Saturation vapor concentration
c_∞	Ambient vapor concentration
Ca	Capillary number, $Ca = \frac{\eta_0 u_c}{\varepsilon^3 \gamma} = \frac{\eta_0^2}{\varepsilon^3 \rho_L \gamma h_0}$
d	Needle diameter
D	Droplet diameter
D_C	Critical diameter for ring formation
D_i	Inner deposit diameter
D_L	Diffusion coefficient of lysozyme, $D_L = 1\ x\ 10^{-10}\ m^2/s$.
D_V	Vapor diffusivity, water, $21.6 \times 10^{-6} \times (1 + 0.0071T)$
E	Evaporation number, $E = \frac{\kappa \Delta T}{\varepsilon \eta_0 L_V}$
g	Acceleration due to gravity, 9.81 m/s^2
g(x,y)	Gabor function
h	Droplet height

I(x,y)	Image luminance distribution
j	Solvent evaporation rate
J	Evaporative flux
k	Number of orientations in wavelet transform, $\theta = k\left(\frac{\pi}{8}\right)$
k_B	Boltzmann constant, $k_B = 1.38065\ x\ 10^{-23}\ \ \mathrm{m^2 kgs^{-2} K^{-1}}$
Kn	Knusden number, $Kn = \frac{\lambda}{L}$
L	Characteristic length
L_V	Latent heat of vaporization
m	Number of scales in wavelet transform
M_W	Molar mass of water, $18.0152\ \mathrm{g/mol}$
n	Number of molecules in the system
p	Pressure, Pa
P_{VS}	Saturation water vapor pressure $P_{VS} = 610.7 \times 10^{7.5T/237.3+T}$
Pe	Peclet number, $Pe = \frac{uL}{D_L}$
Pr	Prandtl number, $Pr = \frac{c_p \mu}{k}$
R	Droplet radius
R_g	Ideal gas constant, 8.314 J/mol·K
R_p	Particle radius, lysozyme, 2 nm
Re	Reynolds number, $Re = \rho_L u_c h_0 / \eta_0$
RH	Relative humidity
t	Time, s
T	Temperature, K

T_S Substrate temperature, K

u Radial flow velocity, m/s

U Potential energy, J

V Volume, m^3

V_D Deposit volume

V_l Volume of single lysozyme molecule, $21.2\ nm^3$

V_L Liquid drop volume

V_R Volume of ring

V_S Volume of lysozyme in solution

w Width of the deposit ring

w Vertical component of flow velocity, m/s

X_L Mean displacement of lysozyme monomers

Greek Symbols

γ Surface tension, N/m

Γ Spatial aspect ratio

η Viscosity

θ Contact angle

θ_0 Initial contact angle

θ_a Advancing contact angle

θ_D Deposit contact angle

θ_r Receding contact angle

κ Thermal conductivity, water, 0.607 ($W\ m^{-1}\ K^{-1}$)

λ Mean free path of molecules, wavelength

λ_L Mean distance between lysozyme monomers

μ Dynamic viscosity, $(-0.0026T^3 + 0.5874T^2 - 47.598T + 1763.4)x10^6$ Pa s

ν Response of neurons

ρ_L Liquid density, $1000 - 0.0067 \times (T - 3.98)^2 + 5.2 \times 10^{-7} \times (T - 3.98)^4$ kg m^{-3}

σ Standard deviation of Gaussian factor

τ_{evap} Evaporation time

φ Solute concentration

φ_A Azimuthal angle

φ_g Gelation concentration

φ_L Lysozyme solution concentration

φ_N NaCl solution concentration

φ_s Close packing of spheres, $\phi_s \approx 0.5718$

Φ Volume fraction

Φ_N Relative NaCl concentration

$\Psi(x,y)$ Wavelet transform

PREFACE

I would like to sincerely thank my advisor, Dr. John A. Barnard, for giving me the opportunity to work with him. I genuinely appreciate the advice, support, and patience he has shown to me throughout this journey. The many helpful discussions and encouragement has made this a very positive learning experience.

I would also like to thank my committee members: Dr. Ian Nettleship, Dr. Jung-Kun Lee, Dr. Sachin Velankar, and Dr. John A. Barnard for their time and guidance. I also thank my labmates: Joshua Zueger, Ziye Xiong, and Erica Stevens for their support, contributions, and discussions. I must also acknowledge the exceptional faculty, staff, and students of the Mechanical Engineering and Materials Science Department at the University of Pittsburgh.

I am very fortunate to have an incredible support system. My parents have been so supportive and so encouraging, and have been there every step of the way. They gave me the most important education: they taught me to never give up and encouraged me to be strong, work hard, and to follow my dreams. I would also like to thank my siblings, Angela and James, my parents in-law, Elaine and Arthur, and the rest of my family and friends. Thank you for listening and for the love and support.

I very gratefully acknowledge my husband, Matthew Gorr, not only for the emotional support, but for advice, helpful discussions, and assistance with code. I thank you for the love and encouragement and for reminding me to take a break occasionally and enjoy life along the way. You are my inspiration. |-o-|

1.0 INTRODUCTION

The self-organization and redistribution of colloidal particles in an evaporating droplet on a flat, solid surface leads to interesting pattern formation in the dried residue. Solute particles generally accumulate on the substrate in a non-uniform manner forming patterns which are indicative of the multi-scale transport phenomena occurring during evaporation. Although the experimental set up is relatively simple, the evaporating droplet system is a complicated problem, relevant to a variety of scientific disciplines. The complex and coupled fluid dynamics, solute self-organization, and phase transition phenomena make for a rich physical system of fundamental scientific interest. Understanding the drying process for colloidal solutions is also critical for many industrial applications including inkjet and 3D printing,[1-3] lab-on-a-chip applications,[4] carbon nanotube assembly,[5] and DNA microarray production.[6,7]

Recent interest has also emerged in interpreting solute patterns of evaporated biological fluid droplets for medical screening and diagnostic purposes. Researchers[8-13] have observed the self-organization and dehydration of drops of human biological fluids (*biofluids*) and found that the solute patterns reflected the health of a patient. These patterns exhibited unique and distinctive morphological characteristics which can act as markers for various pathological processes. This confirms the importance of the physiochemical properties of the biofluid in addition to the mechanisms of fluid transport in pattern formation. As the automatic identification of patterns in biofluids may play a role in developing rapid disease detection,

quantitative analysis of the patterns is also important. Recent studies have demonstrated success using image analysis[9] and pattern recognition techniques[14] in classifying solute patterns from various fluids.

Due to this diverse range of applications and fundamental scientific interest in the system, a number of studies on colloidal droplet evaporation have been conducted over the past few decades. The commonly observed "coffee ring" structure was first explained by Deegan et al,[15-17] who showed that radial capillary flow induced during evaporation caused solute particles to collect in a ring around the perimeter of the drop. Studies on fundamental physical mechanisms of colloidal droplet evaporation have also been conducted to examine the internal fluid dynamics,[18-20] Marangoni effects,[21] advection-diffusion of particles,[22,23] particle-substrate interactions,[24,25] and particle-particle interactions.[26] Phase transition phenomena have also been reported during evaporation of colloidal sessile droplets as a result of the effective increase in solute concentration during evaporation. For example, gel or glassy transitions have been observed during evaporation of polymer solutions[27-29] and drops of whole blood.[11,12]

Understanding pattern formation in micro-scale droplets is also relevant to phenomena such as micro- and nano-fluidics and MEMS device fabrication. However, the literature is dominated by the study of macroscopic droplets (on the order of millimeters). A number of studies have examined pattern formation in micro-scale drops,[3,23,24,30-32] but a physical interpretation of the dynamics in these smaller scale drops is not yet fully established. In these systems, the patterns depend sensitively on the evaporation time and particle transport properties. Furthermore, the micro-scale deposits can be examined using Atomic Force Microscopy (AFM), which is especially well-suited to drops in this size range. AFM provides three dimensional topographic maps with nano-scale spatial resolution to quantify the topography of the deposits.

An understanding of solute transport mechanisms and coffee ring formation for simplified, model biological fluids can help lay the groundwork for understanding highly complex, 'real' systems. In the original work described here, pattern formation is studied during sessile droplet evaporation of dilute aqueous solutions of lysozyme and NaCl. Lysozyme is a well-studied, globular protein found in high concentration in human biological fluids such as tears and saliva. Optical Microscopy, Atomic Force Microscopy (AFM), Drop Shape Analysis (DSA), Image Analysis, and Pattern Recognition techniques are used to examine the morphology of dried sessile droplets of aqueous lysozyme and NaCl solutions. The droplet diameters in this work range from ~ 1 μm to ~ 2 mm, providing a comprehensive study of pattern formation during evaporation of simplified model biofluid droplets at the micro- and macro-scale.

This PhD Dissertation includes a discussion of fundamental theoretical concepts, a review of relevant literature, a detailed description of the research problem, and an explanation of the experimental details in Chapters 2 – 5. The general evaporative behavior and concentration dependence of the aqueous lysozyme system is discussed in Chapter 6.[33] The resulting morphology (peripheral ring with undulating interior) observed in this study is unlike many findings throughout the literature. The deposit shapes depend sensitively on the characteristic time and length scales of the system and the initial droplet shape. The majority of the deposits in this experiment exhibited ring-like shapes, but uniform, cap-like shapes were observed for deposits with very small diameters and these are discussed in Chapter 7.[34] A minimal size for ring formation was observed, dependent on initial lysozyme concentration. The various shapes are described by comparing the dominant transport mechanisms within the drop. The transport properties of the system are further examined by studying the effect of interfacial temperature on the evaporating lysozyme droplet system, as presented in Chapter 8.

The remaining Chapters (9 and 10) focus on the complex patterns formed during evaporation of lysozyme and NaCl solutions. These unique patterns exhibit distinct regions including an amorphous ring as well as crystalline and dendritic structures in the central region of the deposit. The intricate structures and distinctive patterns leave a "fingerprint" which reflects the solution chemistry of the droplet. The effect of concentration and droplet size on pattern formation in this system is summarized in Chapter 9.[35] Building on these findings, Chapter 10 describes a novel pattern recognition algorithm to classify patterns from varying concentrations of lysozyme and NaCl. This algorithm had a success rate of 97% in classifying drops with 4 different concentrations and thus may be relevant to future research in biomarkers and diagnostics. Finally, the main conclusions and overall impact of the work is discussed as well as opportunities for extending this research.

2.0 THEORY

Several important physical mechanisms related to droplet wetting and evaporation are discussed in this chapter. The fundamental concepts of wetting and surface tension are first discussed, followed by an explanation of Young's equation and contact angle hysteresis. The vapor diffusion model of droplet evaporation is then presented, including the general problem formulation and discussion of the solvent evaporation rate. The governing equations for fluid dynamics and the distribution of solute during evaporation are also described for reference throughout this dissertation.

2.1 WETTING

The physical interaction between a liquid droplet in contact with a solid surface has been studied for two centuries[36,37] but research on this interesting phenomenon still appears in the literature today.[32,38-41] In addition to the fundamental physical aspects of the problem, the concept of wetting is relevant to a wide range of scientific disciplines and industries from printing and coatings to food processing and cosmetics.

When a liquid drop is deposited onto a solid substrate, the equilibrium droplet may assume several shapes, depending on the "wettability" of the system. These equilibrium regimes are characteristic of the nature of the liquid and solid and the behavior of the interface at the

contact line. A contact angle, θ, exists between the liquid and solid surface that is characteristic of the three phases in contact. The main equilibrium shapes are often referred to as complete wetting ($\theta = 0°$), no wetting ($\theta = 180°$), and partial wetting ($0° < \theta < 180°$). Several equilibrium shapes and their contact angles are represented in Figure 2.1.

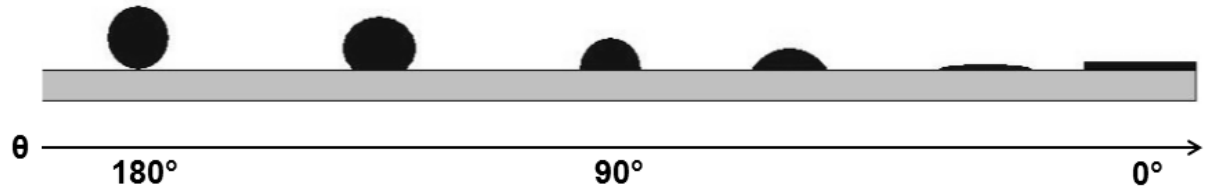

Figure 2.1. Equilibrium sessile droplet shapes.

2.1.1 Surface Tension

The interactions between the solid, liquid, and vapor phases in the evaporating droplet system are controlled by the interfacial energies between these phases. The interfaces may deform or change shape to minimize the surface free energy of the system, resulting in the various equilibrium droplet shapes discussed in the previous section.

The liquid molecules experience attraction which is a result of various intermolecular forces (Van der Waals, electrostatic forces, etc). The molecules at the liquid/vapor interface, however, experience an energy imbalance, caused by a greater attraction between the liquid molecules compared to the interaction between the liquid and gas molecules. This is considered an unfavorable energy state, and leads to a net inward force which seeks to minimize the liquid surface area.[38,42]

For example, consider the potential energy, *U*, between the liquid molecules. A liquid molecule at the liquid/vapor interface will experience an energy deficit of ~ *U/2*. The surface tension (or surface energy density), γ, is a measure of this energy deficit per unit surface area, or

$$\gamma = \left[\frac{\partial U}{\partial A}\right]_{T,V,n}. \quad 2.1$$

Here, *T* is the temperature, *V* is the total volume, and *n* is the number of molecules in the system.[42]

2.1.2 Young's Equation

Each of the three interfaces in the sessile droplet system has a particular free energy per unit area. These interfacial tensions, γ_{SL}, γ_{SV}, and γ_{LV}, for the sessile droplet system are illustrated in Figure 2.2. When the droplet is in equilibrium, the sum of the forces acting on the contact line should be equal to zero. These forces may be represented by the interfacial surface tensions, normalized to a unit length. Young's equation is derived by balancing this force equation:

$$\gamma_{SV} - \gamma_{SL} - \gamma_{LV} cos\theta = 0. \quad 2.2$$

For Young's equation to hold, the system must be in thermodynamic equilibrium, the solid surface must be ideally smooth, and the system should be free from contamination.

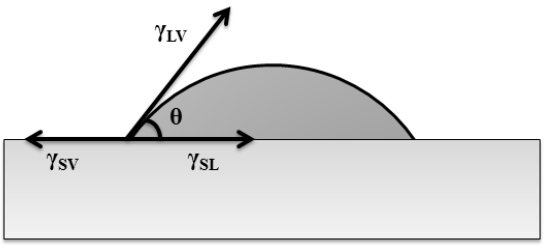

Figure 2.2. Interfacial tensions and equilibrium contact angle for a sessile droplet.

2.1.3 Contact Angle Hysteresis

Determination of the contact angle via Young's equation holds only for ideal, or nearly ideal, situations. In reality, surface roughness, heterogeneities, contaminants, and the nature of some solutes may affect the interfacial tensions and lead to hysteretic effects. This may result in advancing and receding of the drop over the solid surface. Typically, a colloidal sessile droplet is "pinned" upon deposition. Considering these hysteretic effects, the contact line is pinned when $\theta_r < \theta < \theta_a$. The angles θ_a and θ_r define the limits above and below which the contact line will begin to move. The advancing angle, θ_a, occurs when the solid/liquid contact area increases, while θ_r refers to the receding angle which describes a shrinking contact area. Metastable states exist between these advancing and receding angles, which are separated by energy barriers.[38]

2.2 DROPLET EVAPORATION

Evaporation refers to the transfer of molecules from the liquid phase to the vapor phase. The energy loss in this system is described by the latent heat of vaporization. At the molecular level, this is a measure of the kinetic energy. For example, molecules with higher kinetic energy have a greater probability of overcoming energy barriers to enter the gas phase. Liquid droplet evaporation is essentially a vapor diffusion process, first described for the colloidal sessile droplet by Deegan et al[15] and summarized in the following sections.

2.2.1 Problem Formulation

Consider a sessile droplet on a flat, horizontal surface. The droplet is bound by the contact line on the plane of the substrate. Cylindrical coordinates (r, φ_A, z) are used for the mathematical formulation of the problem, where z is normal to the plane of the substrate. Due to the axial symmetry of the sessile droplet problem, no quantity depends on the azimuthal angle, φ_A. The origin is chosen as the center of the droplet, $r = 0$. Further assumptions made in formulating the evaporation model are described below.

2.2.1.1 Knusden Number

To determine a suitable model for evaporation, the Knusden number, *Kn*, can be determined. The Knusden number is a dimensionless number that relates the mean free path of the molecules, λ, to a characteristic length scale, L:

$$Kn = \frac{\lambda}{L}. \tag{2.3}$$

When $Kn \ll 1$, the system is within the continuum mechanics regime. If $Kn > 1$, the mean free path of the molecules are comparable to the length scale, and thus statistical mechanics should be used in the problem formulation.[18]

In the evaporating droplet system, the mean free path of vapor molecules, λ, is compared to the droplet radius, R. In this experiment, the solvent is DI water and the mean free path of water vapor molecules is $\lambda \sim 70$ nm. The droplet sizes are on the order of microns or larger. Therefore, it is assumed that droplet evaporation and related fluid dynamics within the droplet are within the continuum regime and macroscopic models of evaporation are applicable.

2.2.1.2 Bond Number

The evaporation model can be further explored by determining the dominant forces on the droplet. The dimensionless Bond number relates the ratio of gravitational forces to surface tension forces. When $Bo >> 1$, gravitational forces are dominant and when $Bo < 1$, surface tension is dominant and gravitational effects may be neglected. The Bond number is given by

$$Bo = \frac{\rho_L g R h_0}{\gamma_{LV}}, \tag{2.4}$$

where ρ_L is the liquid density, g is the gravitational constant, and h_0 is the initial (maximum) height of the liquid droplet. For typical sessile drop experiments found in the literature, the Bond number is small enough so that surface tension is dominant and gravitational effects are neglected.[18] This is also the case in this experiment, where $Bo < 1$. Therefore, the mean drop curvature is constant and the droplet assumes the shape of a spherical cap.[15,18]

2.2.2 Evaporation Model

With small Knusden and Bond numbers, the evaporation model is within the continuum mechanics regime and the initial droplet assumes the shape of a spherical cap. One of the most widely accepted models for sessile droplet evaporation is the "constant contact diameter" model described by Deegan[15] and expanded upon by Popov.[18] In this model, the droplet is assumed to be pinned at the contact line with a fixed radius, R. The contact angle and droplet volume decrease with time.[18] The parameters describing the problem are illustrated in Figure 2.3, given a sessile droplet with radius, R, and contact angle, $\theta(t)$.

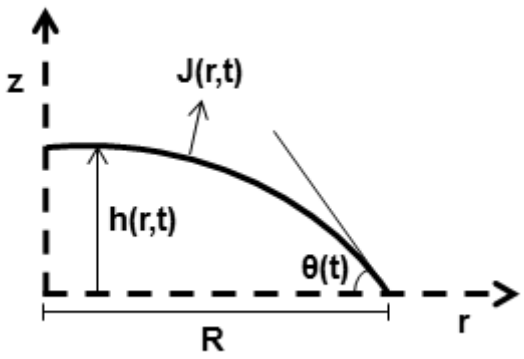

Figure 2.3. Schematic of the geometry and coordinates in the sessile droplet system.

To determine the rates of evaporation and fluid flow, the droplet height must be determined as a function of time. Assuming spherical cap geometry, the height of the droplet, *h(r,t)* is:

$$h(r,t) = \sqrt{\frac{R^2}{\sin^2\theta(t)} - r^2} - \frac{R}{tan\theta(t)}. \quad 2.5$$

The volume of the liquid droplet, V_L, can also be expressed as a function of time by:

$$V_L(t) = \int_0^R h(r,t) 2\pi r dr \quad 2.6$$

$$V_L(t) = \frac{\pi R^3}{3\sin^3\theta(t)}\left(1 - cos\theta(t)\right)^2\left(2 + cos\theta(t)\right). \quad 2.7$$

2.2.3 Evaporation Rate

At the liquid/vapor interface, the vapor concentration, *c*, is assumed to be equal to the saturation vapor concentration, c_V. Far above the droplet, the vapor concentration approaches an ambient value, c_∞. The difference in vapor concentration drives droplet evaporation according to the diffusion equation,

$$\frac{\partial c}{\partial t} = D_V \Delta c, \tag{2.8}$$

where D_V is the vapor diffusivity. In the vapor diffusion model, the rate-limiting process is diffusion of the liquid vapor and the evaporation process is considered to be a quasi-steady state.[18] The transient term can be neglected and the diffusion equation reduces to the Laplace equation:

$$\nabla^2 c = 0. \tag{2.9}$$

At the liquid/vapor interface, the evaporative flux is expressed by

$$\vec{J}(r,t) = D_V \nabla c. \tag{2.10}$$

The evaporation rate is not solved analytically in most cases, as it is an integral of a nontrivial special function. Deegan et al[15] reported an analytical solution for the Laplace equation for evaporation which considered the boundary value problem identical to a charged conductor of a spherical cap shape by equating c with the electrostatic potential and J with the electric field.[17] However, this simplification still requires use of so-called toroidal coordinates and special functions.[15,18,20] Hu and Larson derived an FEM (finite element method) model to describe sessile droplet evaporation, which is comparable with Deegan's analytical solution.[43] Following the solution by Hu and Larson,[43] the evaporation rate can be expressed by:

$$j(r) = \frac{2}{\pi} \frac{D_V (c_0 - c_\infty)}{\sqrt{R^2 - r^2}}, \tag{2.11}$$

where

$$c_0 - c_\infty = \left(\frac{M_W P_{VS}}{R_g T} \right) (1 - RH). \tag{2.12}$$

In the system described here, M_W is the molar mass of water, P_{VS} is the saturation water vapor pressure, R_g is the ideal gas constant, and RH is the relative humidity.

2.2.4 Hydrodynamic Flow

2.2.4.1 Governing Equations

The governing equations in the evaporating sessile droplet are related to conservation laws. The fluid flow is governed by continuity and Navier-Stokes equations. As these are often solved numerically, the appropriate scaling and assumptions are described below.

The vertical and radial coordinates are scaled by h_0, the initial droplet height, and r_0, the initial radius, with $\varepsilon = h_0/r_0$. The velocity field has two components in the radial and vertical directions:

$$\vec{\boldsymbol{v}}(r,z,t) = u(r,z,t)\widehat{\boldsymbol{n_r}} + w(r,z,t)\widehat{\boldsymbol{n_z}}. \tag{2.13}$$

The radial velocity is scaled by the characteristic viscous velocity, $u_c = \eta_0/\rho_L h_0$, where η_0 is the viscosity of the pure solvent. The vertical component of the velocity is scaled by $w_0 = \varepsilon u_c$. The dimensionless Reynolds number, $Re = \rho_L u_c h_0/\eta_0$, appears in the formulation considering the above scaling. The lubrication approximation is often assumed in hydrodynamic models of droplet evaporation, where ε^2 and εRe are assumed to be much less than 1.[16,17,19] By applying this approximation and the above scaling to the Navier-Stokes equations, fluid flow in the evaporating droplet is described by:

$$\begin{gathered} \frac{1}{r}\frac{\partial(ru)}{\partial r} + \frac{\partial w}{\partial z} = 0 \\ -\frac{\partial p}{\partial r} + \eta\frac{\partial^2 u}{\partial z^2} = 0 \\ -\frac{\partial p}{\partial z} = 0 \end{gathered} \tag{2.14}$$

The pressure is scaled by the characteristic pressure $p_c = \eta_0 u_c r_0/h_0^2$ and the time is scaled by the characteristic time: $t_c = r_0/u_c$.

The boundary conditions are given by

$$p|_{z=h} = -\frac{1}{Ca}\frac{1}{r}\frac{\partial}{\partial r}\left(r\frac{\partial h}{\partial r}\right)$$

$$\frac{\partial u}{\partial z}|_{z=h} = 0 \qquad 2.15$$

$$u|_{z=0} = 0$$

$$w|_{z=0} = 0$$

where the dimensionless capillary number is given by $Ca = \eta_0 u_c/\varepsilon^3\gamma = \eta_0^2/\varepsilon^3\rho_L\gamma h_0$.

By solving Equation 2.14 with the boundary conditions in Equation 2.15, the velocity field can be written as a function of the droplet profile *h(r,t)*:

$$u = -\frac{1}{Ca}\frac{\partial}{\partial r}\left(\frac{1}{r}\frac{\partial}{\partial r}\left(r\frac{\partial h}{\partial r}\right)\right)\left(\frac{z^2}{2} - hz\right)$$

$$w = \frac{1}{Ca}\frac{\partial}{\partial r}\left(\frac{r}{\eta}\frac{\partial}{\partial r}\left(\frac{1}{r}\frac{\partial}{\partial r}\left(r\frac{\partial h}{\partial r}\right)\right)\right)\left(\frac{z^3}{6} - h\frac{z^2}{2}\right) \qquad 2.16$$

The height averaged radial velocity can be determined by:

$$\langle u\rangle = \frac{1}{h}\int_0^h u dz = \frac{1}{Ca}\frac{h^2}{3}\frac{\partial}{\partial r}\left(\frac{1}{r}\frac{\partial}{\partial r}\left(r\frac{\partial h}{\partial r}\right)\right). \qquad 2.17$$

The height evolution during evaporation is expressed by:[19]

$$\frac{dh}{dt} + \frac{1}{r}\frac{\partial(rh\langle u\rangle)}{\partial r} = -JE, \qquad 2.18$$

where *J* is scaled by $J_c = \kappa\Delta T/L_V h_0$. Here, κ is the thermal conductivity of the liquid, ΔT is the temperature difference between the substrate and vapor temperature, and L_V is the latent heat of vaporization. The evaporation number, *E*, is given by $E = \kappa\Delta T/\varepsilon\eta_0 L_V$.

2.2.4.2 Distribution of Solute

Now, consider the redistribution of solute throughout the droplet during evaporation. The concentration of particles is assumed to be uniform in the *z* direction. From the conservation of solute, the height averaged solute concentration, φ, is given by:

$$\frac{\partial(h\phi)}{\partial t} = -\frac{1}{r}\frac{\partial(rh\phi\langle u\rangle)}{\partial r}, \tag{2.19}$$

where the concentration, φ, is scaled by the initial concentration, φ_0. Assuming contact line pinning and axial symmetry, the boundary and initial conditions for Equations 2.18 and 2.19 can be written as

$$\begin{aligned} h|_{t=0} &= 1 - r^2 \\ \langle u\rangle|_{r=0} &= \langle u\rangle|_{r=R} = 0 \\ \frac{\partial h}{\partial r}|_{r=0} &= 0 \\ \phi(r,0) &= \phi_0 \\ \frac{\partial \phi}{\partial r}|_{r=0} &= 0. \end{aligned} \tag{2.20}$$

In the presence of diffusion, a finite Peclet number is introduced into Equation 2.19:

$$\frac{\partial(h\phi)}{\partial t} = -\frac{1}{Pe}\frac{1}{r}\frac{\partial(rh\phi\langle u\rangle)}{\partial r}. \tag{2.21}$$

Following the solutions and scaling of the Navier-Stokes equations discussed above,[41]

$$Pe = \frac{uL}{D_L}, \tag{2.22}$$

where u is the particle velocity, L is the characteristic size of the system, and D_L is the particle diffusion coefficient. In general, when $Pe >> 1$ advection dominates transport and when $Pe << 1$, diffusion is the dominant mechanism.

2.2.4.3 Droplet Shape Evolution

The governing dynamic equations for the droplet profile (Eq. 2.18) and particle concentration (Eq. 2.19 or Eq. 2.21) can be solved numerically to determine height and concentration profiles at various times during evaporation. The general solutions with expressions for the height evolution and particle concentration over time led to the widely accepted descriptions of drop evaporation dynamics by Deegan[15] and Hu and Larson.[43] In addition, the final distribution of solute and the geometry of the deposit were examined by Popov[18] and Fischer[19] by closer examination of the solution of Equation 2.19.

In general, the contact angle and droplet volume decrease during evaporation, but the diameter remains the same. As the remaining liquid is depleted, the familiar "coffee ring" of solute is left behind. This final coffee ring shape is noted in a number of systems but other shapes have been observed which depend on the physiochemical properties of the fluid.

While these initial studies on droplet shape and evaporation dynamics laid the theoretical groundwork for solution of the problem, these works consider non-interacting, non-diffusing particles. In reality, however, the system is much more complicated than the ideal case which is often assumed in the literature. In particular, these models assume that the solute does not affect evaporation and any phase transitions within the droplet are neglected. However, in many systems of interest, the final shape of the deposit can be affected by other physical mechanisms including Marangoni flow, heat transfer, and particle interactions. These experimental systems and additional considerations are described in more detail in Chapter 3, which includes a more extensive review of the literature. A solution to the hydrodynamic equations presented in Section 2.2.4 is given in Chapter 7.

3.0 REVIEW OF THE LITERATURE

The physical mechanisms governing the evaporation of a sessile droplet on a solid substrate have been studied for hundreds of years and date back to Young,[36] Maxwell,[37] and Langmuir.[44] However, this phenomenon has attracted considerable interest over the past few decades due to the variety of applications and relevance to a number of scientific fields. In this chapter, a review of the literature on various aspects of pattern formation in evaporating droplets is provided including general pattern formation, evaporative dynamics, heat transfer, and phase transformations. The general, aggregation, and transport properties of lysozyme are also discussed. Finally, a review on image analysis and pattern recognition techniques for quantitative study of the patterns is provided.

3.1 PATTERN FORMATION IN EVAPORATING DROPLETS

The redistribution of colloidal particles during evaporation leads to patterned residues with consistent morphologies, indicative of the complex, multi-scale transport phenomena which occur during drying. When the contact line is pinned during evaporation, solute particles generally accumulate in a ring around the periphery of the drop due to the “coffee ring effect.” Although ring formation has been demonstrated in a variety of systems, a uniform film is often preferred in applications such as printing and coatings. The morphology of these patterns can be

controlled by manipulating various parameters of the experiment. Pattern formation in evaporating droplets can be influenced by wetting properties, fluid dynamics, Brownian motion, phase transitions, heat transfer, and the physiochemical properties of the solution. These physical mechanisms are further discussed in the following sections.

3.1.1 Evaporative Dynamics and General Pattern Formation

The "coffee ring effect" was first explained by Deegan et al.[15-17] Using a particle-tracking method with polystyrene microspheres in water, they showed that a non-uniform evaporative flux induced radial flows which transported solute to the contact line. To investigate droplet pinning, a pure water droplet and a colloidal solution droplet were deposited onto a freshly cleaved mica surface. They found that the colloidal drop remained pinned to the substrate while the pure water droplet receded as it evaporated. During evaporation of the pinned droplet, radial fluid flow developed to maintain wetting of the contact line, while the contact angle decreased. This phenomenon is illustrated in Figure 3.1. Solvent flowing from the center of the drop replaces solvent removed at the periphery, where the evaporative flux is greatest. The solute is transported to the edge of the drop and deposited as the solvent evaporates. The solute particles accumulate along the periphery, which perpetuates contact line pinning.[16,17]

Pinning of the droplet at the interphase boundary is treated as a geometric constraint, characteristic of colloidal solution drops, and is generally considered to be a requirement for ring formation. However, the radial flow alone has been proposed as an alternative prerequisite to the pinning condition.[45] In addition, Sangani et al determined the capillary force on particles near the contact triple point, and proposed a criteria for pinning based on these forces.[31]

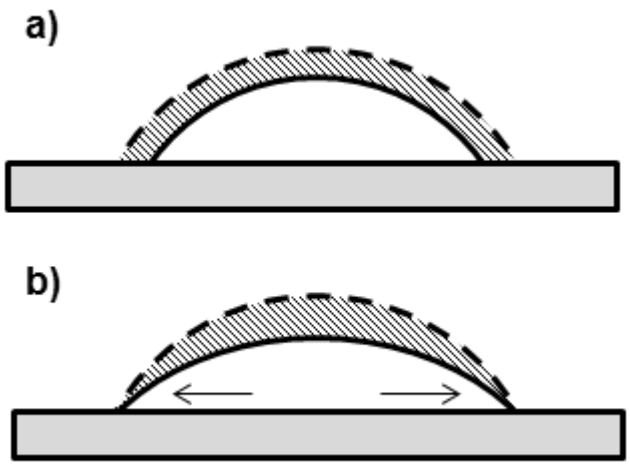

Figure 3.1. Schematic of (a) receding contact line and (b) pinned contact line.

Several groups have modeled the dynamics of the system as well as the geometry of the initial drop and the annular deposit. Popov[18] presented a theoretical model describing the geometric characteristics of the deposit. He demonstrated that the deposit patterns are functions of the initial concentration of the solute, initial geometry, and time elapsed for evaporation. A model by Fischer[19] considered a colloidal sessile drop in several different modes of evaporation including an open system and one in which evaporation was greatest at the center of the droplet. By modeling flow profiles inside the drop, he verified that the solute was distributed in a ring for the open system. When the evaporation was greatest at the center, the solute was distributed uniformly with no solute ring.

Hu and Larson[20,21,43,46] further described the evaporative flows using a particle tracer method to measure the rate of droplet evaporation and examine the velocity fields in the evaporating droplet. They described the evaporation of a pinned sessile drop as a quasi-steady state process and developed a Finite Element Model (FEM) and an expression for the evaporation rate, which they found was very nearly constant. They also went on to consider the flow in terms of Marangoni stresses.[20,21] They explained that a surface tension gradient is

generated along the free surface of the droplet due to thermal cooling or a variation in solute composition. This can cause additional convection currents and affect the deposition patterns left on the substrate, particularly for a multi-component system. In an additional study, they added that the Marangoni effect may reverse coffee ring deposition and that the formation of a peripheral ring actually requires the suppression of Marangoni flows.[21]

Experimentally, many researchers have extended this body of work on colloidal sessile droplet evaporation to include variations in the types of solutes and solvents used in the system. These include aqueous solutions of polystyrene microspheres[24] and nanospheres,[45,47,48] ceramic and oxide powders[49-53] carbon black nanoparticles,[50] copper sulfate, colloidal gold,[54] colloidal silica,[55,56] and TiO_2 nanoparticles.[57] This behavior has also been explored with aqueous suspensions of organic molecules including sugar, citric acid, urea,[54] polysaccharides,[27] motile and non-motile bacteria,[58] DNA,[6,7] and serum albumin.[54,59-62]

Though often neglected, several studies have focused on the influence of gravity and sedimentation on pattern formation.[47,49,50] Sommer[47] studied the impact of gravity on nanosphere suspensions and found that the effects of gravity are negligible for drops with diameters less than 1mm in these nanoparticle colloidal solutions. Recently, Sandu et al.[50] determined that gravity is a contributing factor in larger sized aggregates, where sedimentation occurs in addition to evaporative flows. This is also true for ceramic particles,[49] though it is generally minimized by dispersants and therefore often neglected. In this study and much of the literature, however, the effects of gravity are neglected because of the small particle size in nanoparticle suspensions and a small Bond number (discussed in Chapter 2). When $Bo < 1$, surface tension is dominant and therefore gravitational effects may be neglected.

Techniques have been developed to control the patterns in the deposit by manipulating the evaporative flux,[17] contact line depinning,[6,22,57] particle-substrate interactions,[24,25] and the physiochemical properties of the solution.[2,26,52,53,63-66] A "phase diagram" was recently proposed by Bhardwaj et al. to describe the shape of a colloidal deposit.[25] This was based on the competition between three types of flow: radial capillary flow, Marangoni recirculating flow, and the transport of particles toward the substrate driven by DLVO (Derjaguin, Landau, Verwey, and Overbeek) interactions. In addition, the shape of solute particles was found to influence the deposit pattern. Yunker et al.[26] examined evaporation in aqueous suspensions of latex particles with a spherical and ellipsoidal shape. They found that solutions containing spherical particles exhibited the typical coffee ring behavior, but ellipsoidal particles tended to collect at the air-water interface and form a loosely-packed network which resisted coffee ring formation.

3.1.2 Pattern Formation in Microscale Droplets

Despite the vast potential applications of smaller drops in micro- and nanofluidics and surface patterning applications,[1,32,48] little work exists in the literature on drops with diameters less than 1 mm. Although several studies have emerged which consider micro- scale drops,[3,24,30,31,67-69] a physical interpretation of the dynamics in these smaller scale drops is lacking in the literature. Recently however, Shen et al.[23] examined micro- scale drops to determine the minimum diameter for coffee ring formation using aqueous solutions of colloidal polystyrene beads with three different diameters (20 nm, 60 nm, and 100 nm). Though these well studied systems tend to produce ring-shaped deposits, the deposits from very small drops (with diameters less than ~ 10 μm) did not exhibit the typical ring-like shape. A minimum droplet diameter was found to exist for ring formation at this scale. For drops with diameters less than this critical value, the

particles were dispersed homogenously on the substrate. The particle transport mechanisms were studied to interpret these results. The homogenous deposit formed when the liquid solvent evaporated faster than the rate of particle diffusive motion.[23]

Former members of our group[67-69] also studied drops with a diameter less than 50 μm, using suspensions of dendrimer molecules in alcohol. They took advantage of Atomic Force Microscopy (AFM) techniques, well-suited to smaller scale drops, to generate detailed topographic maps at the nano-scale of the resulting morphologies. It was also demonstrated that pattern formation depended sensitively on the evaporation rate, solution concentration, and dendrimer surface chemistry.

3.1.3 Heat Transfer

To fully examine the dynamics occurring within the droplet during evaporation, the heat transfer must also be considered. Numerical investigations, such as those by Bhardwaj et al.[22] and Girard et al.[70] have examined the effect of substrate temperature on the general droplet dynamics. This includes solving the heat equation along with the continuity and Navier-Stokes equations for hydrodynamic flow. Based on the numerical results, these studies found that heating the substrate causes an increase in the droplet evaporation rate and consequently the rate of fluid flow within the droplet.

The effect of substrate temperature on droplet evaporation has also been studied experimentally for systems of pure water[71-73] as well as suspensions of nanoparticles[74] and polymers.[75] By using IR thermography on pinned water droplets during evaporation, it was determined that the drop apex remains cooler than the fluid near the contact line for the majority of the evaporation process.[76] This increases the fluid flow near the substrate and also affects

Marangoni convection within the droplet, particularly when significant temperature gradients are observed. The increase in the fluid and mass flow rates results in patterns with more concentrated coffee rings and less solute remaining in the central region.[75]

3.2 PATTERN FORMATION IN EVAPORATING DROPS OF BIOLOGICAL FLUIDS

The self-organization of biological fluids accompanying dehydration has attracted attention in the literature over the past two decades, as there is evidence that useful information can be extracted from the dried droplet patterns which remain on the substrate. In particular, the evaporation of sessile drops of human biological fluids in ambient conditions results in complex patterns in the solid phase structures which form on the substrate. These structures can act as markers for various pathological processes and thus, may reflect the health of the patient. Therefore, the ability to recognize, interpret, and classify these unique patterns offers potential applications in medical screening and diagnostics.

Several groups have demonstrated this phenomenon experimentally by comparing the patterns resulting from dehydrated biological fluid drops of healthy patients and those with various disorders. For example, Yakhno et al.[10,77,78] examined the structural evolution of evaporating drops of human blood serum. They compared patterns in dried serum drops of healthy patients to those with carcinoma, viral hepatitis, and burn disease. They also examined serum from women after normal or premature childbirth and determined that recognizable structural differences existed in these patterns. Killeen et al.[9] studied the differences in patterns of blood serum from patients with B cell disorders and multiple myeloma compared to those of

healthy patients. They examined the structural properties of the patterns and also developed a quantitative image analysis method that attempted to classify patterns of drops. Additional human biological fluids were studied by Shabalin and Shatokhina,[13] who found that tears, synovial fluid, and urine also exhibited similar health-dependent morphological differences. Recently, Brutin et al.[11,12] examined drops of whole blood and determined that the resulting patterns were also regular and reproducible for drops from healthy, anaemic, and hyperlipidaemic patients.

There have been additional studies on the differences in morphology of the patterns in deposits from tear droplets of healthy patients and those with various disorders.[79-81] Kuo et al.[79] identified zones within a dried teardrop which include an amorphous peripheral ring, "central," and "transitional" zones. The central and transitional zones contain crystallite structures and branched, fern-like crystals. Though this general morphology is consistent, slight variations were observed in patients with ocular disease. The amount of "ferning" in the central region of the deposit was indicative of pathology.[79,80] Tear deposits have been further investigated by Raman spectroscopy based on the drop coating deposition method.[79,82] The Raman spectra were compared for patients with and without infection and found to be considerably different, indicating changes in protein structure and binding.[79,82]

Many biofluids can be described as containing three types of solute: proteins, lipids, and inorganic salts. For example, the main components of liquid tears and their concentrations are presented in Table 3.1.[83] The chemical composition of biofluids is known to vary at the molecular level when affected by disease, cancer, or other pathologies. The identification of protein[79,82,84-86] or metabolic[87] "biomarkers" in biofluids for diagnostic purposes is the subject of large-scale investigations. For instance, the Plasma Proteome Project (PPP) by the Human

Proteome Organization (HUPO) is an international collaboration focused on characterizing plasma and serum biomarkers and standardizing analytical methods of biomarker discovery.[88] Spectroscopic methods have been used to detect these small changes in protein structure and composition of biofluids.[79,82,84-86] Mass spectroscopy has also been used for biomarker discovery in saliva[85,86] and for detection of oral cancer.[86] For example, Hu et al.[86] discovered that 52 proteins were present in saliva from patients with oral squamous cell carcinoma (OSCC) but these proteins were absent in the saliva from healthy patients. On the other hand, 29 proteins were detected only in healthy patients and were lacking in the patients with OSCC.[86]

Table 3.1. The main components of liquid tears

Protein	Concentration (g/100mL)	Ion	Concentration (g/100mL)
Total Protein	0.751	Na^+	0.184 - 0.391
Lysozyme	0.236	K^+	0.0235 - 0.164
Albumin	0.130	Ca^{2+}	0.00120 - 0.00802
Tear Albumin	0.123	Mg^{2+}	0.00073 - 0.00267
Lactoferrin	0.184	Cl^-	0.376 - 0.479
Other	0.0427	HCO^-_3	0.159

Conventional diagnostic methods are typically labor-intensive and expensive. While the detection of specific protein biomarkers is less so, there are still a number of challenges and costs related to these methods of detection and identification. The change in composition of the biofluid may be detected through examining droplet deposits as the deposit morphology is highly influenced by the physiochemical properties of the fluid. Thus, detecting changes in biofluid drop deposit patterns may be a robust and inexpensive alternative.

3.3 PHASE TRANSITIONS IN EVAPORATING DROPLETS

Phase transition phenomena have been reported during evaporation of colloidal sessile droplets. The solute concentration of the fluid increases as the solvent is depleted, which modifies the rheological and physiochemical properties of the solution during evaporation. In general, when solute (sol) particles are suspended in a solvent, the phases are separated initially. Under appropriate conditions, the sol particles aggregate until a network is formed and a sol-gel transition takes place. Colloidal gels and glasses have been reported to form under various conditions resulting from chemical and physical interactions, DLCA (diffusion limited cluster aggregation), spinodal decomposition,[89] percolation, and jamming.[90]

Gel or glassy transitions have been observed in evaporating sessile drops of aqueous colloidal silica,[91] polymer solutions,[27-29,92] and in drops of biological fluids.[8,10-12,78,93] In these studies, the existence of radial crack patterns in the final deposit indicated that a gel or glassy transition had occurred. The radial crack patterns in the deposit occur from competition between gelation and dessication kinetics. The "buckling instability" of the deposit, induced during drying, is also influenced by formation of a glassy "skin" at the liquid-vapor interface.[94] Formation of a "skin" has also been observed in drops of ellipsoidal particle suspensions[26] and a gel-like skin was also described in drying drops of whole blood.[12] During evaporation, the skin begins to form at the periphery of the drop while the "coffee ring" develops. The gel transition begins at the droplet edge, while the central part of the droplet remains liquid and the gelation front moves inward as evaporation proceeds. As the remaining liquid evaporates through the structure, the skin buckles and cracks are formed in the deposit.

3.4 EFFECT OF ELECTROLYTES ON PATTERN FORMATION

Pauchard et al.[91] studied the influence of electrolytes on the crack patterns produced during sessile droplet evaporation of a colloidal suspension. Various crack patterns were observed, depending on the salt content in the suspension. These properties are related to the variation of the droplet shape during evaporation, and the droplet shape depended on the salt content in the suspension. For a solution with low ionic strength, the gelation time exceeded the evaporation time, while the higher ionic strength solutions tended to have a shorter gelation time, which affected the final deposits. As the solvent evaporates, the central area of the droplet decreases. The gel ring at the droplet edge tends to contract in the final stages of evaporation and a strong mechanical stress emerges.

In addition to peripheral ring formation, crystallization is frequently observed in the central region of the deposit, and often attributed to the presence of salts in the solution[95] and in biofluids.[10,62] Kaya et al.[95] examined phase separation and crystallization in evaporating droplets of solutions of a polyelectrolyte and salts. Fractals, dendrites, periodic concentric rings, needlelike crystals, and small triangular-shaped crystals were observed. Crystallization during droplet evaporation has been examined in other systems containing salts[62,95,96] and resulted in morphologies similar to biofluid deposits (crystallites in the central region surrounded by an amorphous ring). This general form is believed to be a result of the separation of the fluid components during evaporation. The protein tends to accumulate at the periphery and the salts in the central region.

Kuo et al.[79] identified three zones of a dried teardrop: “central, transitional, and ring zones.” The ring zone included the peripheral ring which was believed to contain mainly protein components. The central and transitional zones of the deposit contained crystallite structures and

branched, fern-like crystals. Pearce and Tomlinson[81] studied the chemical composition of the deposit by using SEM coupled with EDXS analysis and determined that the ferns contained predominantly Na, K, and Cl. Sulfur, which is indicative of biomacromolecules, was detected primarily at the periphery of the deposit.[81]

3.5 LYSOZYME

3.5.1 Properties

Lysozyme is a small, compact, globular protein with a roughly ellipsoidal shape and is found in high concentration in human mucosal secretions including tears and saliva. Due to its stability and availability in high purity, lysozyme is well studied and has been the subject of many protein crystallization[97-101] and adsorption studies.[102-106] Hen egg white lysozyme (HEWL) is commonly used in these studies due to the ease in purification and solubility over a wide range of conditions. Lysozyme was also the first enzyme whose atomic structure was determined by X-ray diffraction of crystals.[107] Using this technique, the dimensions were measured for tetragonal lysozyme crystals and determined to be roughly 3.0 nm x 3.0 nm x 4.5 nm. Lysozyme has an isoelectric point of pH 11.1, and carries a net positive charge at physiological pH and a net charge of +9 per molecule at a pH of 5.6.[108] Several properties of lysozyme are summarized in Table 3.2.

In lysozyme adsorption studies, no large scale conformational changes have been reported between lysozyme molecules in aqueous solution compared to adsorbed lysozyme molecules. Lysozyme adsorbs onto the surface as monomers, and once adsorbed, the molecules

tend to diffuse on the surface to form clusters.[106] The interaction between lysozyme and a negatively charged, freshly cleaved, mica substrate has been examined. The positive lysozyme was found to nearly neutralize the surface charge of mica.[105]

Table 3.2. Properties of lysozyme.

Property	Value
Dimensions, nm	3 x 3 x 4.5
Molecular Mass, kDa	14
Isoelectric Point	11.1
Diffusion Coefficient, m^2/s	$D_L = 1 \times 10^{-10}$

3.5.2 Self-Association, Aggregation, and Crystallization

Over the past few decades, there has been a growing interest in the study of liquid phases, gels, clusters, and crystallization in protein solutions due to a variety of applications such as drug delivery and cell scaffolding. As lysozyme is stable and easily purified, many studies have been conducted on self-association[89,109-111] and crystallization[97-101] in aqueous lysozyme solutions.

Considerable research has examined the liquid-liquid phase separation and phase transition in supersaturated globular protein solutions.[89,99,101,109-111] These studies predict a separation to a protein-rich and protein-poor phase, the formation of fractal clusters, metastable crystal nucleation and growth, and nonequilibrium kinetically arrested states. The mechanism for phase separation in the lysozyme solutions include protein-protein interactions which are subject to short range attractions and long range repulsion, often modeled by the classical DLVO (Derjaguin, Landau, Verwey, and Overbeek) potential. The short range attractions considered in protein-protein studies include Van der Waals, hydration, and hydrophobic interactions while the long range repulsions are associated with electrostatic interactions and consider the net charge of

the protein and ionic strength of the solution.[89,111] Lysozyme protein interactions have also been studied by varying the salt concentration of lysozyme solutions. As the concentration of salt rises, the effective protein-protein interactions are more attractive.[109]

Since most proteins are water soluble, they are traditionally crystallized from aqueous solutions. The driving force for protein crystallization is the degree of supersaturation; the protein concentration must be greater than the equilibrium concentration for this phase transition to occur. Crystal growth in solution occurs by mass transport toward the crystal and incorporation of growth units. Lysozyme crystals are often grown in aqueous sodium chloride solutions, resulting in the commonly observed tetragonal structure or variations of this structure (orthorhombic) at different temperatures and levels of supersaturation.[97,98,101,112-114] The aspect ratio of tetragonal lysozyme crystals is known to change with supersaturation, from elongated crystals at low supersaturation to plate-like crystals at high supersaturation. If the supersaturation is yet higher, precipitation occurs instead of crystallization.[112] The effect of pH on lysozyme crystallization has also been studied. Single tetragonal crystals are formed at low pH and "needle like" crystals develop as the pH increases.[98,101,113,114] If crystal growth is diffusion-limited, the crystal morphology may become unstable or spherulitic.[114] The mass transport clearly influences the formation of these crystals and liquid-liquid phase separation, and therefore must be considered.

3.5.3 Transport Properties

Several experimental studies[115,116] confirm that lysozyme diffuses on solid surfaces and in solution with a diffusion coefficient of $D_L = 1 \times 10^{-10}$ m^2/s. In these investigations, the diffusion coefficient of lysozyme, D_L, was determined as a function of concentration and the experimental

results were compared to the concentration dependence of the diffusion coefficient for rigid Brownian particles. This models the particles as identical rigid spheres. For volume fractions from 0.015 to 0.4, the concentration dependence of D_L for lysozyme is similar in behavior to the theoretical results for Brownian spheres.[116] It was also pointed out, however, that the theoretical calculations for rigid spheres do not account for aggregation and tended to overestimate the reduction in diffusion as the concentration increases.[116]

The concentration dependence of the self-diffusion coefficient of a Brownian spherical particle is described by:[117]

$$\frac{D}{D_0} = \frac{1 - \frac{9}{32}\varphi}{1 + H(\varphi) + \left(\frac{\varphi}{\varphi_s}\right) / \left(1 - \frac{\varphi}{\varphi_s}\right)^2}, \tag{3.1}$$

where φ_S is the concentration of close packing of spheres $\varphi_s \approx 0.5718$,

$$D_0 = \frac{k_B T}{6\pi\eta R_p}, \tag{3.2}$$

$$H(\varphi) = \frac{2b^2}{(1-b)} - \frac{c}{(1+2c)} - \frac{bc(2+c)}{(1+c)(1-b+c)}, \tag{3.3}$$

$$b = \sqrt{\left(\frac{9\varphi}{8}\right)}, \tag{3.4}$$

$$c = \frac{11\varphi}{6}, \tag{3.5}$$

k_B is the Boltzmann constant, η is the viscosity of pure water, and R_p is the particle radius. The above equations can be used with parameters assumed for lysozyme (R_p = 2 nm) to model the concentration dependence of D_L. Using Equations 3.1 - 3.5, the behavior of $D_L(\varphi)$ for lysozyme is plotted in Figure 3.2.

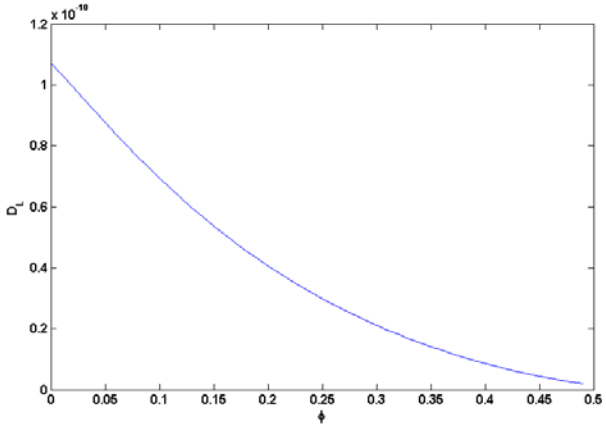

Figure 3.2. Estimated diffusion coefficient of lysozyme as a function of concentration, $D_L(\varphi)$.

3.6 IMAGE ANALYSIS AND PATTERN RECOGNITION IN IDENTIFICATION OF FLUIDS

Pattern recognition of images is applicable to a variety of fields such as biometrics and forensics, through human identification by iris,[118] fingerprint, face, voice, and handwriting,[119] for example. In addition, pattern recognition has been proposed for use in defect detection, food analysis, and identification of chemical data in arrays.[120] These pattern recognition and machine learning techniques may be applicable in detecting small differences in drop deposition patterns and therefore automatic identification of patterns in biofluids may play a role in developing rapid disease detection. While several studies have demonstrated the unique pattern formation in biofluids, few attempts have been made at quantifying these patterns. However, recent studies have demonstrated success with using image analysis[9] and pattern recognition techniques[14] in classifying fluid droplet patterns. The following sections discuss the major components of these algorithms, including feature extraction and classification, and the general aspects of detecting differences in fluids using these techniques.

3.6.1 Image Feature Extraction

Biometric techniques have become popular methods of identification because of the accuracy of these methods. Biometric features often used in these techniques are unique to the individual. For example, every iris has relatively the same shape, size, and location in the face but each iris has a detailed, intricate, and distinctive structure. Each individual's iris is unique, making iris recognition an attractive method of identification. In addition, there is a large database (9 million+) of iris images for comparison to accurately determine the degree of classification.[118] The reliability of any pattern recognition algorithm depends on the amount of separation or overlap between the various classes. Therefore, the information used in classification should be selected to observe these statistical requirements. This unique information is referred to as the "features" of the image, which make up a feature vector for classification.

One of the most popular methods of feature extraction in biometric applications uses wavelet transforms to extract "texture." Instead of using image features such as pixel statistics, histograms, shapes, or parametric transforms, wavelet transforms provide spatial frequency data and have been used for feature extraction in voice classification,[119] microarray data analysis,[120] and iris recognition[118] algorithms. The popular Discrete Wavelet Decomposition (DWD)[119,120] involves the decomposition of a raw signal onto a set of basis functions (or, the image) by dilation, contraction, scaling, and shifting of the signal (in this case, the image pixel information). This includes applying successive lowpass and highpass filters which decomposes the data into two sets of coefficients which contain information about the signal at various scales. For example, a coarse scale corresponds to global features and a finer scale represents local features. In images, the decomposition of an n x n image into wavelet coefficients includes first applying the filters to the rows of the image. This splits the original image into two subimages:

a highpass and a lowpass filtered image with dimensions *n*/2 x *n*. Then, the filters are again applied, but this time to the columns of both subimages to get four subimages of dimension *n*/2 x *n*/2 representing the high- and low- pass filters applied in the horizontal and vertical directions.[119,120]

These general wavelet methods were also used for iris recognition. Daugman originally developed the method of using convolution with bandpass filters for extracting textural information from iris images.[118] Daugman's algorithm included using 2D Gabor filters which are useful in determining orientation and frequency selective properties, or in other words, the phase quantization of the iris pattern. This method is described as follows. Assume $\Psi(x,y)$ represents a 2D "mother" wavelet. From this wavelet function, a self-similar collection of "daughter" wavelets $\Psi_{mpq\theta}(x,y)$ can be determined where

$$\Psi_{mpq\theta}(x,y) = 2^{-2m}\Psi(x',y')\,. \tag{3.6}$$

The variables (x',y') introduced in Equation 3.6 contain dilations of the wavelet in size by 2^m, translations in position *(p,q)*, and rotation through angle θ:

$$x' = 2^{-m}[xcos(\theta) + ysin(\theta)] - p \tag{3.7}$$

$$y' = 2^{-m}[-xsin(\theta) + ycos(\theta)] - q. \tag{3.8}$$

Daugman chose the 2D Gabor wavelet for $\Psi(x,y)$ which is defined as:

$$\Psi(x,y) = e^{-\pi\left[\frac{(x-x_0)^2}{\alpha^2}+\frac{(y-y_0)^2}{\beta^2}\right]}e^{-2\pi i[u_0(x-x_0)+v_0(y-y_0)]}. \tag{3.9}$$

The variables (x_0,y_0) denote wavelet position information, (α,β) are effective width and length, and (u_0,v_0) describe the modulation wave-vector, which (in polar coordinates) is related to spatial frequency $\omega_0 = (u_0^2 + v_0^2)^{1/2}$ and orientation $\theta_0 = \tan^{-1}(v_0/u_0)$.

Finally, since the wavelet coefficients are complex-valued, the real and imaginary parts of the subimages can be used to extract image texture information in terms of local modulus and

phase. This information makes up the "256 byte iris code" for each iris, which is the feature vector for comparison to other iris codes. Next, the fraction of bits that disagree from iris to iris is detected. Daugman's algorithm allowed up to 27% of the bits to disagree while still accepting the iris codes as a match.[118] This was Daugman's prototype in pattern matching, though the methods of classification have improved in recent years. These additional methods of classification in pattern recognition are further described in the following section.

3.6.2 Classification

The features discussed above are the output of the measurement process, or a set of numbers that characterize specific properties of the image. These features are used as the "measurement vector" for classification. There are many classification algorithms used such as k- means, decision tree, and density- based methods, which can be broadly described as supervised or unsupervised learning methods.[121] A supervised learning process includes training set, where each vector is labeled with the class to which it belongs. Then, the classes are represented statistically and new measurement vectors are assigned to a class, predefined by the training set. The classification algorithm computes the distance between the vectors of unknown and labeled classes and minimizes the distance. This distance can be determined in a number of ways; one of the most popular is by simple Euclidean distance.[121] A variation of this is the "nearest neighbor" classification algorithm, which assigns the unknown to the same class as the class of the nearest neighbor in the training set. There are also statistical classification methods such as maximum likelihood and Bayesian decision rules.[121] For example, the maximum likelihood algorithm uses statistical representations to describe the probability that a vector which has a certain set of measurements belongs to a particular class.

In unsupervised learning techniques, vectors are not identified *a priori* by class, but clusters are observed in the data. A clustering algorithm associates samples with the nearest cluster using various methods of doing so such as hierarchical and k-means clustering algorithms. Hierarchical methods involve grouping of the clusters at different levels and does not require a predefined number of clusters.[119,121] Each vector initially starts as its own cluster and pairs of clusters are combined as you move up the hierarchy.[119] The k-means clustering algorithm is one of the most popular clustering algorithms. This algorithm consists of four steps: assign samples to clusters or choose cluster centers and assign all samples to the nearest cluster, determine the mean of each cluster, reassign each sample to belong to the nearest cluster mean, if nothing changed, exit, otherwise go to step 2 and repeat.[121] In these clustering algorithms, the distances between the clusters and the cluster means can be measured by Euclidean distance, $d(a, b) = |a - b|$, or the additional decision rules mentioned above.

3.6.3 Identification of Fluids

Killeen et al.[9] studied the mechanisms of drying human serum droplets and developed a method for pattern classification between healthy serum samples and those with myeloma. Various image parameters (contrast, brightness, mean square deviations, number of lines, intensity histogram, etc.) were determined over a rectangular window along the radius of the drop in the image. They determined that the intensity variation and change in contrast within the window were "characteristic features," unique to each class of drop (healthy vs. myeloma). In an attempt to reduce noise caused by droplet size and other external features, they plotted the change in intensity against the change in contrast along the droplet radius to produce a "signature" plot, which was used to classify the samples.[9]

Kim et al.[14] used pattern recognition techniques in identifying a variety of fluids such as popular soft drinks, wines, and colloidal systems with inorganic and organic solutes. The study was completed to examine two ideas: algorithms trained with existing data can identify unknown patterns and automated pattern recognition methods can group patterns that differentiate between combinations of liquid and substrate chemistry. This included the extraction and computation of feature vectors which they denoted as $f = [\alpha f_c, \beta f_L, \gamma f_G, \epsilon f_S]$. The feature vector was made up of f_c, the color distribution, f_L, local binary patterns (LBP), f_G, Gabor wavelet patterns, and f_S, the relative size of the droplet. The relative weights ($\alpha,\beta,\gamma,\varepsilon$) were found by normalizing each component to the range of [0,1]. Feature vectors were determined for each image and classified based on several different methods for comparison. The classification algorithm included using 10 training images and the k- nearest neighbor method of classification. The clustering algorithms were based on unsupervised learning and compared k-means, average linking, and spectral clustering algorithms. The classification accuracy ranged from 80 to 90%, while the clustering accuracy ranged from 62 to 80%.[14] These methods may be improved and optimized to identify the patterns resulting from evaporation of simplified model biological fluids, which is one of the main components of this PhD dissertation.

4.0 RESEARCH DESCRIPTION

4.1 HYPOTHESIS

The primary hypothesis of this PhD dissertation is that incremental changes in experimental conditions result in reproducible and statistically interpretable variations in the self-assembled patterns that develop during sessile droplet evaporation of simplified model biological fluids. A supplementary hypothesis explored throughout this dissertation is that evaporative patterns from simplified biofluids can act as a "fingerprint" for identification based on solution chemistry. The supplementary hypothesis therefore serves as a "proof of concept" of the working hypotheses. This work will provide guidance on interpreting the patterns from colloidal fluid evaporation (especially biological fluids) and support of the idea that the detailed morphology of the patterns may function as biomarkers or indicators of various physical interactions.

There are two distinct investigative undertakings in this PhD research. The first set of experiments involves the evaporation of aqueous lysozyme solution droplets under varying experimental conditions, investigating the core hypothesis. In particular, the effects of lysozyme solution composition, droplet size, and evaporation conditions are explored. The general evaporative behavior and resulting pattern formation are described in Chapter 6. The effect of lysozyme concentration is examined for droplets with sizes ranging from micro- to macro- scale. This work is extended in Chapter 7 to examine even smaller droplets on the order of 1 - 20 μm

and a characteristic size for ring formation is documented. The diffusive and convective motion of the lysozyme particles is explored to interpret the cap- and ring-shaped deposits. The effect of heat transfer on pattern formation is studied in Chapter 8, by changing the temperature of the substrate and thus changing the evaporation rate and fluid flow velocity within the droplet.

The second set of experiments investigates changes in solution chemistry with a particular focus on the effect of electrolytes on pattern formation of aqueous lysozyme droplets. This also includes quantifying the deposit patterns using image analysis and pattern recognition techniques. In Chapter 9, pattern formation is examined in evaporating solution droplets containing a fixed amount of lysozyme with incremental changes in NaCl concentration. Chapter 9 also includes an interpretation of these patterns in two size regimes (at the micro- and macro- scale). These patterns are further examined in Chapter 10, which focuses on a novel pattern recognition technique used to classify the deposits based on their fluid compositions. To the best of the author's knowledge, this is the first attempt in using pattern recognition techniques to classify small, incremental changes in fluid composition.

4.2 OBJECTIVES

The primary purpose of the research described in this PhD dissertation is to investigate evaporative behavior and pattern formation in evaporating sessile drops of simplified model biological fluids and the effect of small, incremental changes to experimental conditions. Understanding pattern formation in the evaporating colloidal droplet system is relevant to a variety of technologies such as printing and coatings. This research also involves interpreting the evaporative behavior at the micro-scale, which is especially well-suited to applications such

as lab-on-a-chip or microarray printing and analysis. Research on colloidal droplet evaporation is also of considerable fundamental scientific interest as a natural phenomenon involving coupled fluid dynamics, particle transport, self-assembly, and phase transformations.

The goal of this research is to develop an understanding of the effect of various experimental conditions on pattern formation in this system and to create a robust pattern recognition technique to classify the morphological patterns. The specific objectives of this PhD research can be summarized as follows.

1. To understand morphological features in the self-assembled patterns produced during evaporation of droplets of aqueous lysozyme solutions deposited on oxidized Si wafer substrates.
2. To understand the role of solution composition in pattern formation in this system.
3. To understand the effect of characteristic size and time scales on pattern formation in this system.
4. To understand the effect of heat transfer on pattern formation in this system.
5. To understand the role of electrolytes on pattern formation of simplified model biofluids (aqueous lysozyme – NaCl solutions).
6. To develop a novel pattern recognition technique to classify images of deposits from evaporation of solutions with different concentrations of lysozyme and NaCl.

5.0 EXPERIMENTAL DETAILS

5.1 SOLUTION PREPARATION

High purity lysozyme powder (Sigma Aldrich, L6876) and sodium chloride (NaCl) were used to prepare concentrated lysozyme and sodium chloride stock solutions. These powders were dissolved, as-received, in deionized water (Millipore, 18.2 MΩ·cm) at 35° C to concentrations (φ_L) of 2.0 g/100mL. The concentrated stock solutions were diluted with DI water to create the desired concentrations, ranging from 0.1 – 1.0 g/100mL. Solutions were stored at 2º C and brought to room temperature prior to deposition.

Commercial lysozyme powder is known to contain salts for purification and buffering purposes.[111,122] The concentration of salts in commercial lysozyme has been previously measured using X-ray fluorescence and was found to range from 3.6% to 10.2% (w/w) of chloride, or up to 46 moles of chloride per 1 mole of lysozyme.[122]

5.2 SUBSTRATES AND DEPOSITION TECHNIQUES

Oxidized silicon wafers were chosen as a substrate in this experiment due to the surface charge, reflective properties, and ease of preparation. The silica surface of the silicon wafer is negatively charged and attracts the positively charged lysozyme molecules, ensuring that the droplets will

be quickly and strongly pinned. A number of studies have been conducted which examine the adsorption of lysozyme on silica.[123-125] These studies demonstrated that lysozyme adsorbed to the silica substrate in monolayers. At low concentrations, lysozyme adsorbed "side-on" and as the concentration increased above 0.1 g/100mL, the lysozyme absorbed with "end-on" orientation.[123] Another advantage of surface oxidized silicon wafer substrates in this experiment is their reflective properties. The lysozyme drop deposits are nearly transparent and when deposited on the reflective silicon wafers, details within the deposits are visible using reflection optical microscopy.

Prior to deposition, silicon wafers were cleaned in ultrasonic baths (Fisher Scientific, FS20) of alternating isopropyl alcohol (IPA), acetone, and DI water and blown dry with compressed air. Droplets were deposited using several methods to produce a wide range of drop diameters for this research. These methods include deposition via micro-pipette, drop-on-demand printing, aerosol spray, and a nebulizer. The deposited droplets evaporated under ambient conditions.

The micropipette (Rainin, 0.2 - 2.0 µL), with micro-tips (Fisherbrand, 0.1 - 10 µL), was used to produce droplets with volumes of ~ 0.2 µL and diameters of ~ 2 mm. A drop-on-demand printer (MicroFab Technologies, Inc., JetLab4) was used to produce arrays of droplets with consistent diameters and spacing of ~ 100 µm. An example of a printed array is given in Figure 5.1. The Preval® aerosol spray system was used to produce droplets with diameters ranging from ~ 10 µm to 250 µm. The substrate was held approximately ~ 0.6 m (~ 2 ft) from the spray nozzle. The Omron MicroAir® Nebulizer (NE-U22V) was used to produce very small droplets ranging from D ~ 1 - 30 µm. This ultrasonic nebulizer, used commercially for delivery of liquid medication, uses high speed vibrations (180 kHz) to create a mist of small droplets.

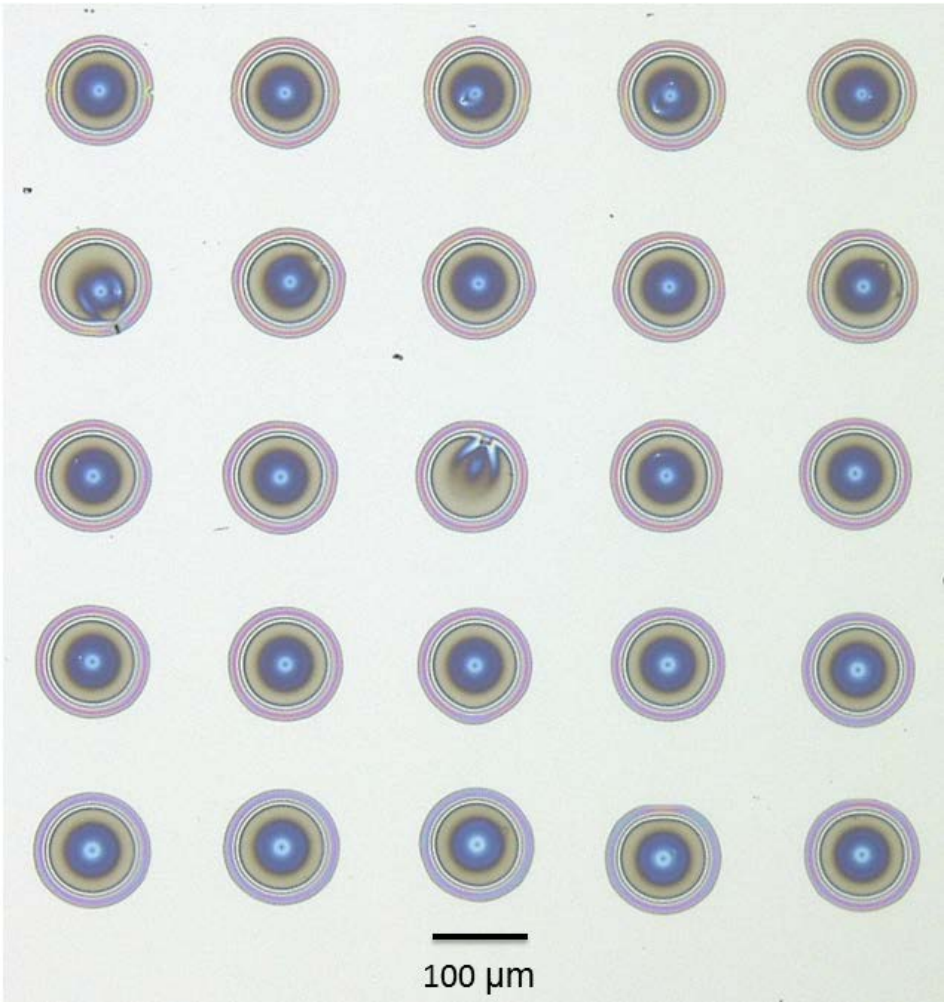

Figure 5.1. Deposit array pattern (φ_L = 1.00 g/100mL) from the drop-on-demand printer.

Drops selected for detailed analysis were limited to those with nearly circular contact lines. The typical range of drop sizes and shapes as well as the areal number density of drops produced by the aerosol system are illustrated in the low magnification optical images in Figures 5.2a – 5.2c for φ_L = 0.1, 0.5, and 1.0 g/100mL, respectively. Figure 5.2d includes a higher magnification image of the droplets within the selected rectangular portion of Figure 5.2c.

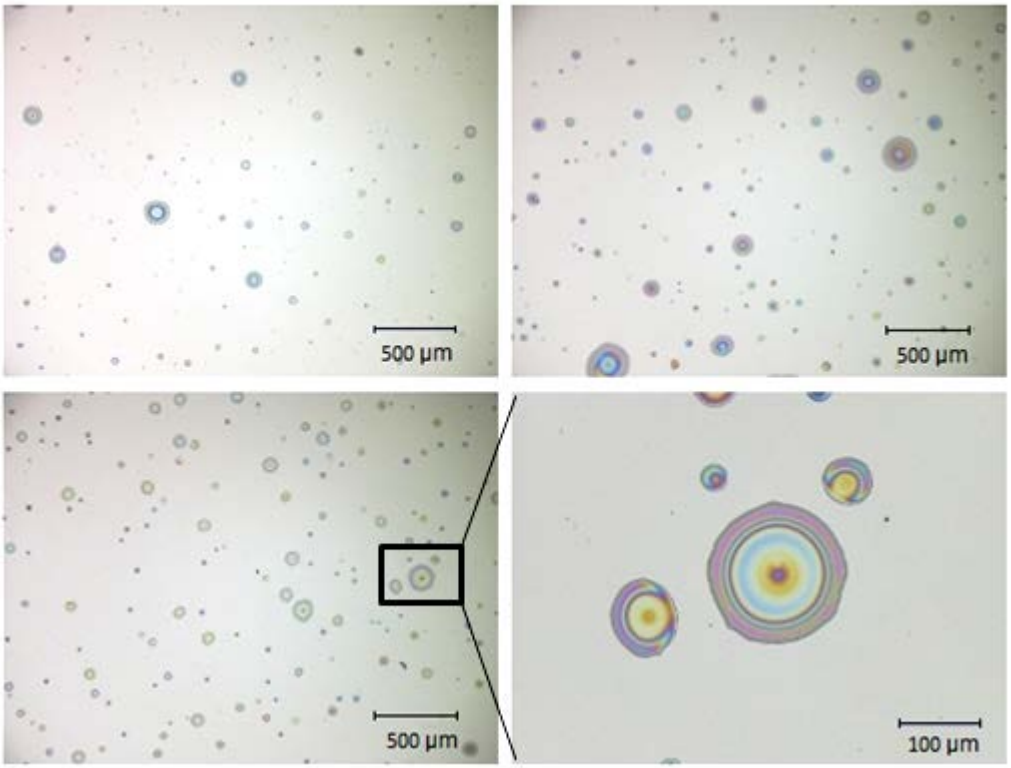

Figure 5.2. Reflection optical microscopy images illustrating typical droplet sizes produced by aerosol deposition.

Note the distortions in the residue shape found in the smaller deposits in Figure 5.2d. The "coffee ring effect" is suppressed in the regions of the smaller drops that are closest to the large drop. This effect is due to overlapping of the vapor fields of closely neighboring drops. The evaporation rate is lowest where the vapor fields of two neighboring drops overlap.[17,126] The slower evaporation rate in the area of the overlapping vapor fields leads to less flux of solute to that region of the drop. The vapor diffusion field from the large drop extends further than that of the smaller drops. The region of the small drops closest to the large drop is saturated with extra vapor molecules, decreasing the driving force for water to leave the drop in this area and therefore suppressing ring formation. The vapor fields of the small drops have a much smaller range and do not affect ring formation in the large drop.

5.3 OPTICAL MICROSCOPY

A digital optical microscope (Keyence, VHX-600) was used to examine the drop deposits. The colors were adjusted by setting the white balance using a reference card and the images were collected in the "image enhancement" mode, which automatically adjusts the contrast in the image to enhance features. Examples of typical images acquired from the Keyence optical microscope are shown in Figure 5.2. In addition, the real-time evaporation process for lysozyme solution droplets deposited via micropipette was monitored by video recording with the Keyence optical microscope at 28 frames per second.

5.4 DROP SHAPE ANALYSIS

A Drop Shape Analysis (DSA) system (Kruss, D100) was used to analyze basic wetting behavior and surface tension in this experiment. In the Kruss DSA system, the stage is illuminated from one side and a CCD camera captures the image on the opposite side. Droplets are deposited by a syringe with a standard needle with a diameter of 1.7 mm. Droplet images are displayed on the monitor and analyzed by the proprietary Kruss DSA 1.9 software, which calculates various properties of the droplet. Frames can be analyzed and captured in sequence to enable time dependent measurements.

In the sessile drop method, the droplet is deposited on the substrate, which lies on the stage. The base diameter, droplet volume, and contact angle are determined by the software fitting a circle to the droplet profile. The frames are captured every 30 seconds during evaporation. An example of a sessile droplet image is given in Figure 5.3.

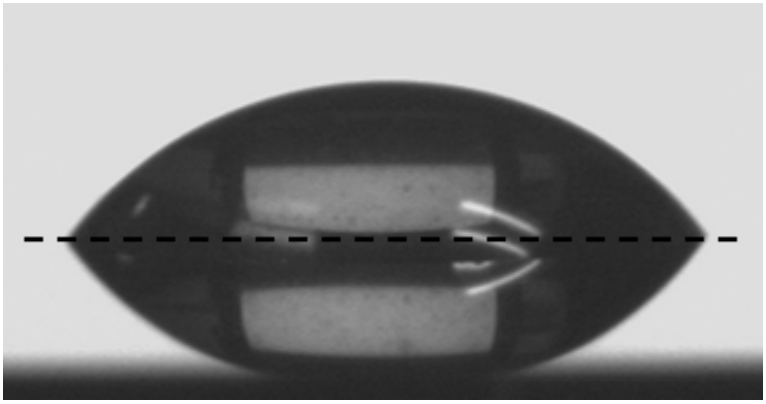

Figure 5.3. Sessile droplet profile of solution with φ_L = 1.0 g/100mL, D ~ 2 mm.

In the pendant drop method, a droplet is suspended from the syringe needle. The force due to surface tension is proportional to the diameter of the needle, d. For the droplet to remain suspended, the force due to surface tension is balanced by the force due to gravity and the surface tension, γ, is determined by $mg = \pi d\gamma$. This is also measured over time by capturing frames and performing this calculation every 30 seconds. An example of a pendant drop image is given in Figure 5.4.

Figure 5.4. Pendant drop image of solution with φ_L = 1.0 g/100mL.

5.5 ATOMIC FORCE MICROSCOPY

Atomic Force Microscopy (AFM) was used to characterize the detailed morphology of the deposits at nano- scale resolution. The AFM provides measurements of the geometry of the deposit, roughness, and overall shape of the deposit, which is useful in interpreting the deposit. AFM is a form of Scanning Probe Microscopy (SPM), which involves scanning a probe across a surface and monitoring the probe – surface interaction. The scanner is piezoelectric which expands and contracts in proportion to an applied voltage, controlling the height of the cantilever and tip. Independent piezo electrodes for x, y, and z directions are combined to form the scanner which manipulates the probe in three dimensions. The force between the tip and surface is kept constant during scanning by maintaining a constant cantilever deflection and vertically moving the scanner at every (x,y) position to maintain the "set-point" deflection. The position of the scanner at each (x,y) is stored by the computer, which forms the topographic image of the surface with nano- scale resolution.[127] The general set up is given in the schematic of Figure 5.5.

There are several types of AFM measurements including Contact Mode, Non-contact Mode, and Tapping Mode. In contact mode, the tip comes in contact with the surface through the adsorbed fluid layer on the surface. In non-contact mode, the tip does not contact the surface, but oscillates just above the surface. The Van der Waals forces and other long range forces cause the resonant frequency of the cantilever to decrease which causes the amplitude of oscillation to decrease.[127] In tapping mode, the cantilever is oscillated near its resonant frequency. When the tip is brought into proximity of the surface, the forces between the tip and the sample lead to deflection of the cantilever. Van der Waals forces cause the amplitude of oscillation to decrease as the tip comes closer to the sample. The deflection is measured by a laser spot reflected from the top surface of the cantilever and detected by a photodiode array.[127]

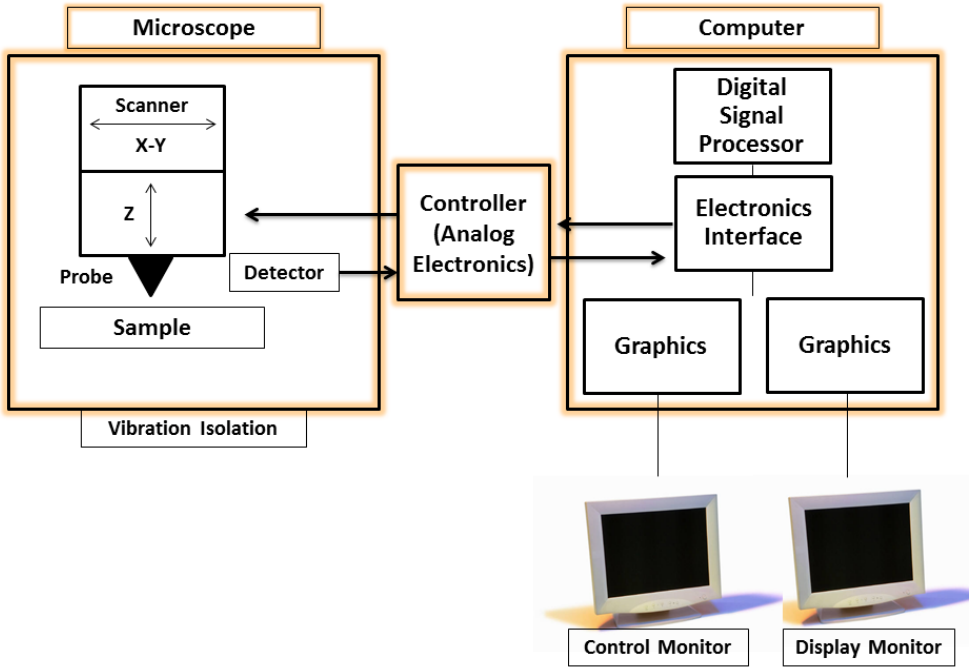

Figure 5.5. Basic schematic of AFM system setup.

In this experiment, drops with D < 50 µm were characterized in air by AFM (Digital Instruments, D3100) in Tapping Mode with a standard tip (K-TEK Nanotechnology, LLC, NSG01). The AFM data was analyzed to extract the critical dimensions, RMS roughness, cross-sectional profiles, and volumes of the dehydrated residues.

Raw AFM data was analyzed using Gwyddion SPM software, a free, open source, cross-platform, SPM data analysis program.[128] First, obvious scanning defects such as artifacts and scan lines were removed. A small neighborhood of pixels containing the erroneous data was selected and a hyperbolic flatten function was used to interpolate the pixel information from the surrounding area. The data was then leveled using a plane level function which computes the plane from all of the data points and subtracts the plane from the original data. This corrects for slight drift but does not suppress the features or texture of the surface.[128] Finally, the minimum pixel value was set as the plane of the substrate (z = 0).

5.6 EXPERIMENTAL UNCERTAINTIES

The uncertainties in these experimental procedures should be noted. For a given concentration, all lysozyme droplets were prepared from the same base solution. However, the lysozyme concentration may vary slightly from droplet to droplet due to the variation in droplet size and time in "flight" to reach the substrate, especially with aerosol and nebulizer deposition. In addition, there will be natural variation in initial contact angle from droplet to droplet due to local substrate heterogeneities.

Although the resolution of the AFM is on the order of fractions of a nanometer, uncertainties in these measurements should also be noted. The local measurement uncertainty can be estimated from instrument calibration data, following the method described in Klapetek et al.[129] This method was implemented in Gwyddion, where the uncertainty was added to the measurement results and propagated through the statistical functions as the data was processed.

6.0 LYSOZYME PATTERN FORMATION IN EVAPORATING DROPLETS[33]

6.1 WETTING AND ADSORPTION BEHAVIOR

The overall evaporative and adsorption behavior of lysozyme solution droplets was studied using Drop Shape Analysis (DSA). The Kruss DSA system was used to measure the base diameter, contact angle, and volume of the sessile droplet as a function of time. DSA was also used to determine the surface tension of the lysozyme solutions as a function of time, using the pendant drop method (see Section 5.2).

Sessile droplets of lysozyme in concentrations φ_L = 0.10, 0.25, 0.50, 0.75, and 1.0 g/100mL were deposited onto clean Si wafer substrates. Upon deposition, all of the droplets were pinned and no initial spreading or receding was observed. The initial volume (base diameter) of the sessile droplet was varied to compare the wetting and evaporation behavior for different droplet sizes. The initial contact angle, θ_0, of all lysozyme solution sessile droplets varied from ~ 50° - 60°; little dependence on lysozyme concentration was found. Throughout this work, the initial contact angle is taken as $\theta_0 \sim 55°$. During evaporation of the lysozyme solution drops, the base diameter remained constant over time while the contact angle and volume decreased linearly. When evaporation was complete, a ring like deposit was observed on the substrate which covered the entire wetted area. The contact angle, θ, and liquid drop volume, V_L, as a function of time are illustrated in Figure 6.1 for drops with φ_L = 1.0 g/100mL.

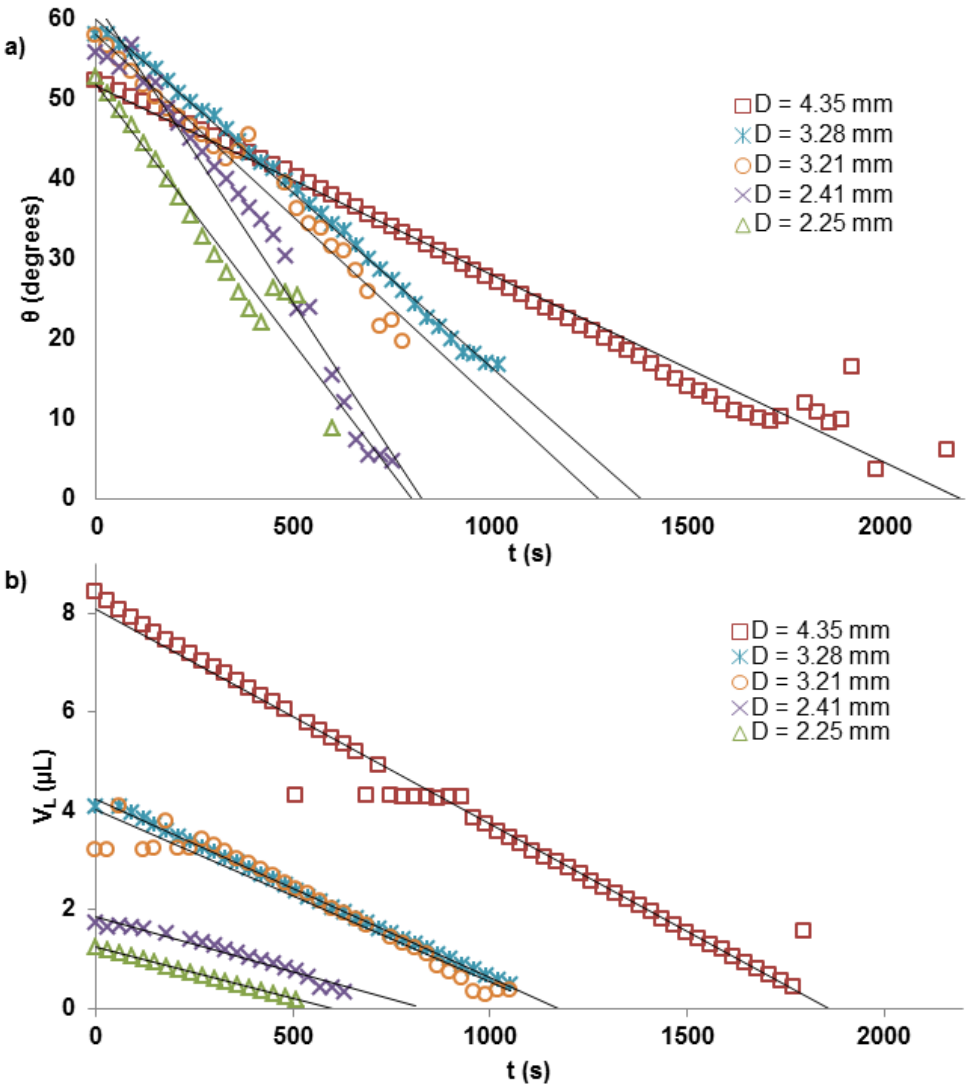

Figure 6.1. The a) contact angle, θ, vs. time and b) liquid drop volume, V_L, vs. time for select drops with φ_L = 1.0 g/100mL.

Figure 6.1 illustrates the behavior of the contact angle and liquid drop volume during evaporation for droplets with base diameters ranging from ~ 2.25 – 4.35 mm. The trendlines are a good fit to a linear relationship with R^2 values from 0.97 – 0.99. As the contact angle approaches ~ 15°, the experimental uncertainty of the DSA measurement increases. This is due to the nature of the measurement. To determine the contact angle, the software fits a circle to the sessile droplet. In this experiment, the shape of the final deposit interferes with detection of the

circle. The trendlines in Figure 6.1a interpolate the trends at these lower contact angles from the linear fit. The volume data in Figure 6.1b was neglected for drops with $\theta < 10°$ due to this increased measurement uncertainty. The interpolated evaporation time from the volume data is in agreement with the measured evaporation time.

In order for the droplet to remain pinned throughout evaporation, a portion of lysozyme molecules must adsorb to the Si wafer substrate. This claim is supported in the literature as lysozyme is known to adsorb to the SiO_2 surface of Si wafer substrates irreversibly in monolayers.[105,106] Lysozyme is also known to adsorb at the vapor-liquid interface, which can be verified from dynamic surface tension data.[130-132] Following this rationale, the DSA pendant drop method was used to find the surface tension of lysozyme solutions as a function of time. The initial surface tension of the solutions of all concentrations in this study was $\gamma_0 \sim 70$ mN/m, which is similar to that of pure water. The dynamic surface tension data from a representative pendant drop with $\varphi_L = 1.0$ g/100mL is illustrated in Figure 6.2.

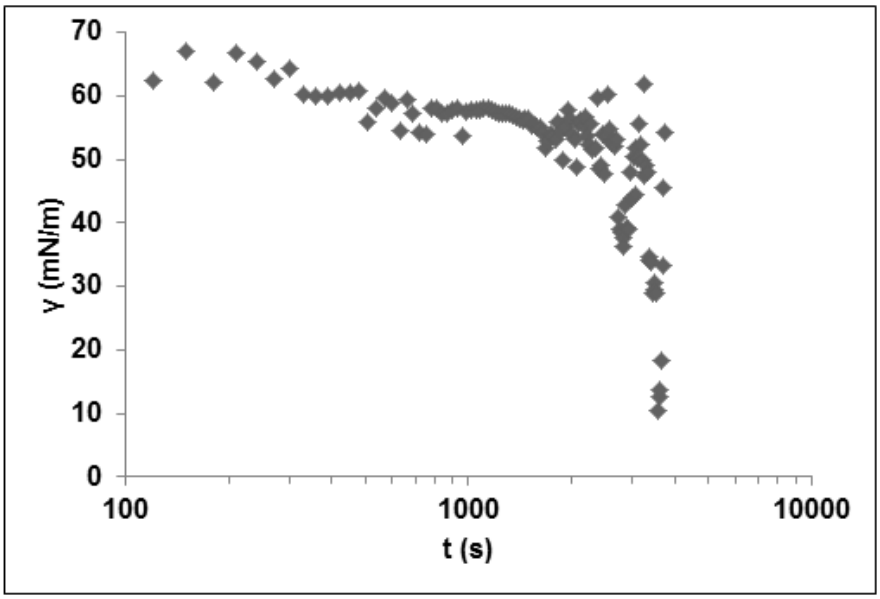

Figure 6.2. Surface tension, γ, vs. ln t, for pendant drop with $\varphi_L = 1.0$ g/100mL.

It is clear from the profile of the surface tension versus ln *t* (Fig 6.2), that no equilibrium state is reached. The surface tension decreases steadily from ~ 70 to ~ 50 mN/m for a prolonged period and begins to fluctuate near 2000 s. At this point, the surface tension decreases more rapidly until the drop is nearly evaporated. This general behavior was similar for all solutions in this study.

Pendant drop experiments have been performed to study the interfacial adsorption of lysozyme.[130-132] The surface tension was found to remain constant during an "induction period" while the protein adsorbs at the interface. As the interfacial concentration of lysozyme gradually increases, the surface tension decreases. At longer times, molecules continue to adsorb and multilayer formation and aggregation may occur. In these studies, the conditions were controlled and surface tension data was taken for up to 24 hours. In our work, however, the pendant drop evaporated in ambient conditions. The general profile shapes are similar to those reported in References [130 – 132], but the surface tension decreases more rapidly due to the loss of solvent and effective increase of lysozyme concentration during evaporation.

6.2 GENERAL OBSERVATIONS: LYSOZYME DEPOSIT MORPHOLOGY

The generally observed morphology of the dried residue resulting from evaporation of drops of lysozyme-DI water solutions on Si wafer substrates is documented in Figure 6.3. This includes an optical (reflection) image, two- and three- dimensional AFM topographic images, and the AFM cross-sectional profile of a droplet deposit with lysozyme concentration φ_L = 1.0 g/100mL and D = 32.6 μm.

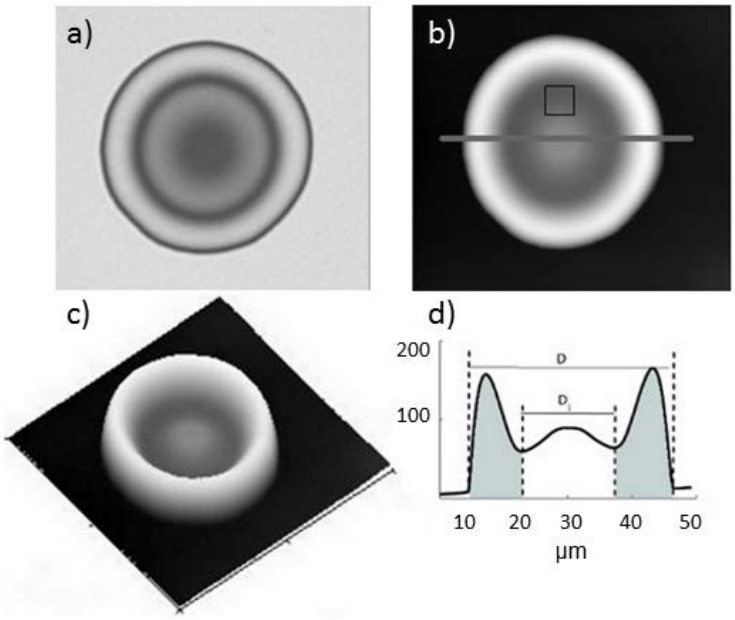

Figure 6.3. Representative images of a single evaporated lysozyme drop deposit.

The images in Figure 6.3 show no evidence of local interior dewetting or significant contamination. The deposit has a smooth surface and is radially symmetric. A single, circular, well-defined "coffee ring" is present at the perimeter of the deposit. Note that the height (z-axis) is in nanometers while the dimensions along the plane of the substrate (at $z = 0$) are micron-scale. In Figure 6.3a, the radial variation of color (not apparent in the gray scale image) tracks the radial variation in deposit thickness and is associated with Fresnel interference.[133] The radial thickness variation is further illustrated in the AFM images (Fig. 6.3; b-c) where the surface profile is determined, in this case yielding a maximum of ~ 160 nm at the peak of the ring. In the AFM images and profiles, it is clear that the ring height is much greater than the drop interior. This suggests that the majority of the solute collects at the periphery during evaporation, due to radial flows. Note, however, that significant solute does remain in the interior of the drop. Within the perimeter ring, the deposit thickness falls rapidly to a minimum

and then rises more gradually to a central mound which usually exhibits a small depression at the center. The central mound is still significantly thinner than the perimeter ring. This complex form is consistently observed in the lysozyme-based system for drops with $D > 20$ μm.

6.3 EFFECT OF CONCENTRATION ON RING FORMATION

Optical microscopy images and AFM data were collected and analyzed for evaporated droplets (deposited via aerosol) with D ranging from ~20 μm to 50 μm for lysozyme concentrations φ_L = 0.10, 0.25, 0.50, 0.75, and 1.0 g/100 mL. Representative examples of deposits with similar diameter are illustrated in Figure 6.4 for comparison. The general form of the lysozyme deposits (rim at the perimeter falling to a minimum and then rising to a central mound) is similar across the range of concentrations in this study. These shapes are also similar to the final deposits observed in the drop shape analysis study.

It is clear from the AFM cross-sections in Figure 6.4 that differences in ring height and width are not dramatic and surprisingly do not reflect the ten-fold change in solution concentration. Upon detailed comparison of many images and profiles for different concentrations, the morphologies of all of the deposits are found to be similar and do not reveal any obvious solution concentration dependence. As in Figure 6.3, the optical images show a radial variation in colors corresponding to the height variation of the deposits (assumed to be transparent). The AFM topographies and cross-sectional profiles in Figure 6.4 again have very smooth surfaces. Complete coverage of the Si substrate over the entire contact area is found in all drops examined.

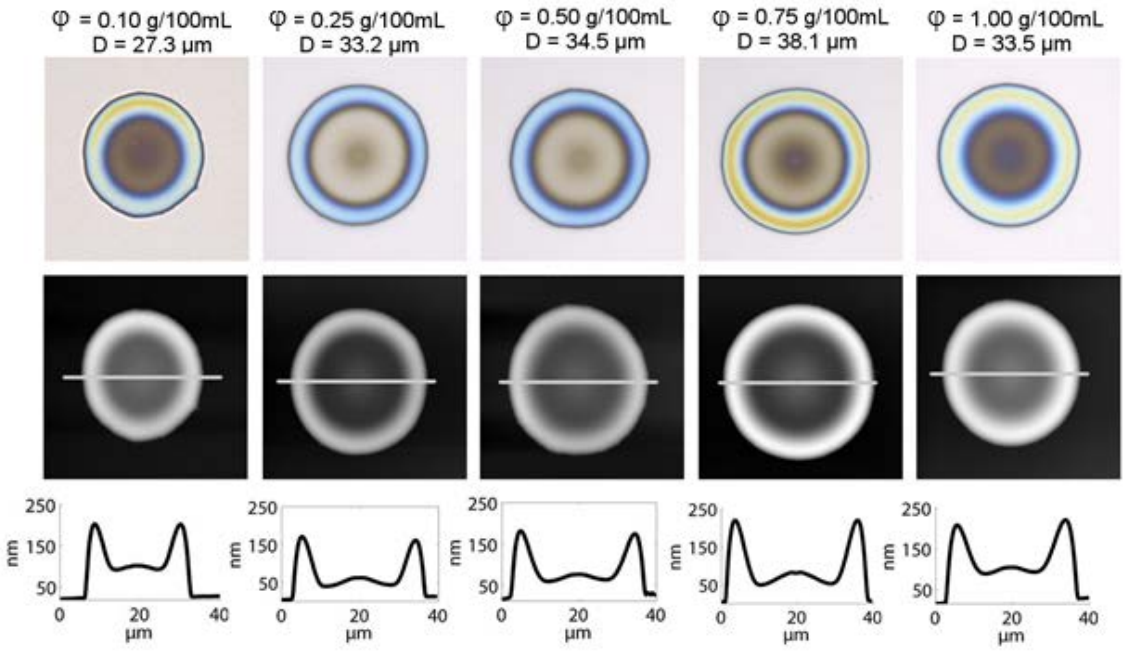

Figure 6.4. Representative morphologies in columns from left to right with increasing φ_L.

6.4 DEPOSIT GEOMETRY

After initial processing of each image, the critical dimensions of the deposit, RMS roughness, and the volume of the deposited solute, V_D, were extracted. The outer drop diameter, D, and the inner diameter between the two minima, D_i, were measured for each deposit as illustrated in Figure 6.3. These values were used to calculate the width of the ring, $w = (D - D_i)/2$. The ring width, w, is expected to scale with drop diameter, based on simple geometric reasoning. This trend is shown in Figure 6.5 for drops from all five concentrations. The trend line is a linear fit through all of the data points with a slope of 0.26 and an R^2 value of 0.98. The relative size of the ring, w/D, is independent of concentration.

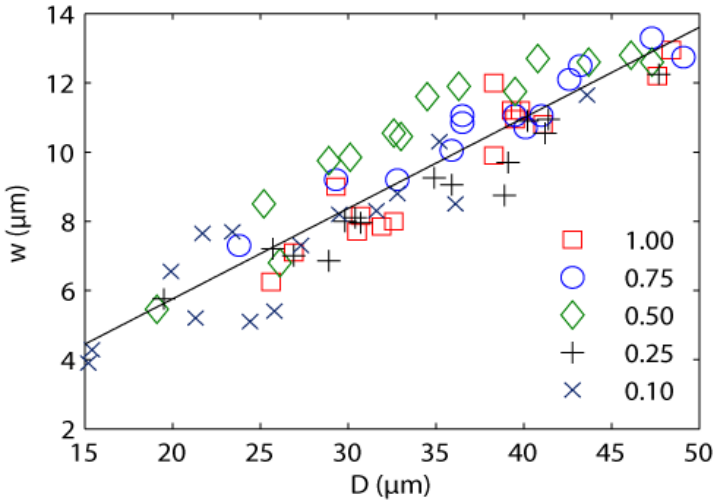

Figure 6.5. The width of the ring, *w*, vs drop diameter, *D*.

To quantify the "smoothness" of the deposit surface, the RMS roughness was determined for the bare Si substrate and compared to a region within the drop interior. A 5 µm x 5 µm square was selected in the same relative position for each drop in a relatively "flat" area of the drop interior so that the effect of large changes in background height would be minimized. The size and position of the selected area is illustrated in Figure 6.3b. The RMS for the Si wafer was ~ 1.5 nm while the RMS of the lysozyme deposit ranged from ~ 2 nm – 5 nm with a mean of 2.8 nm in the selected drop interior region. The surface roughness of the lysozyme deposits was similar for all concentrations and consistent with the finite size of the lysozyme molecules.

The volume of the deposit after evaporation, V_D, was determined for each drop. The drop deposit area was segmented from the background by height threshold and the volume of the deposit was calculated between the height of each pixel and the substrate (at plane z = 0). This volume calculation is equivalent to numerical integration of the two dimensional height profiles using the trapezoidal rule and assuming radial symmetry. This procedure was verified using MATLAB® software to determine the area under the profile curve by trapezoidal numerical integration and the results were in excellent agreement. Assuming a spherical cap geometry with

diameter, D, and a contact angle of 55º for the initial liquid profile of the drop, the volume of the liquid drop (at t = 0) is proportional to D^3. The volume of solute remaining on the substrate was expected to also be proportional to D^3. To verify this relationship, ln V_D vs ln D is plotted in Figure 6.6 for all five concentrations. The linear fit shown on the graph is the average of the slopes of the best fit lines for the 5 different concentrations with a slope of 2.99 and R^2 value of 0.99. As expected, the slope is very close to 3, indicating that $V_D \propto D^3$ for all concentrations of lysozyme and range of diameters in this study.

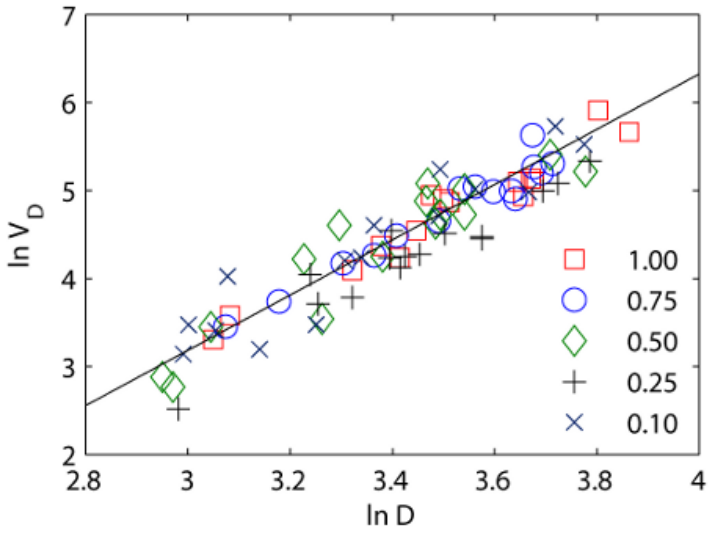

Figure 6.6. Ln-ln plot of deposited volume, V_D, vs drop diameter, D.

One might expect that the deposit density would be dependent on initial solution concentration and that this should lead to five separate but parallel lines of slope 3 for the five concentrations studied with a difference in y-intercept (increasing with solution concentration). However, the variation in y-intercept of the linear fits for the different concentrations is negligible.

The total volume of the outer ring, V_R, was also measured for each deposit. The ring area was selected by subtracting the circular area corresponding to the diameter D_i, leaving only the ring segmented from the remaining data. The selection of the ring area is illustrated in Figure

6.3d in gray. The fraction of the total deposit by volume contained in the outer ring is simply V_R/V_D. In this range of concentrations and drop sizes, V_R/V_D is essentially constant with a value of 0.75 ± 0.02, further demonstrating the geometrical similarity of all the deposits.

6.5 LYSOZYME PACKING IN THE DEPOSITS

The surprising uniformity of the deposit geometry despite the ten-fold concentration difference led to examination of the lysozyme packing in the deposits. Using the reported dimensions of the lysozyme molecule (3 nm x 3 nm x 4.5 nm),[107] the volume of a single lysozyme molecule, V_l, is estimated assuming a prolate spheroid form with a ≈ b ≈ 1.5 nm and c ≈ 2.25 nm: $V_l = 4/3\,\pi abc = 21.2$ nm^3. The total volume of lysozyme in the liquid drop was estimated from the volume of the initial liquid drop (assuming a spherical cap with initial contact angle $\theta_0 \approx 55°$), the concentration of molecules per volume in solution, and the volume of one lysozyme molecule. In the larger volume DSA experiments, it was observed that the diameter of the final deposit was equal to the contact diameter of the liquid droplet at $t = 0$ (no receding of the initial contact line). This behavior is assumed to hold for the smaller drops although direct measurements were not possible. The calculation of total volume of lysozyme molecules in the drop uses the bulk concentration of the solution (evaporation in flight is neglected). Finally, the total volume of lysozyme molecules in a drop is assumed constant, as the number of molecules in the system should be equal before and after evaporation. Using the volume of lysozyme in solution, V_S, and the volume of the deposit, V_D and given that the number of lysozyme molecules is conserved, the volume fraction of lysozyme in the deposit, Φ, is determined by $\Phi = V_S/V_D$.

The mean volume fraction of lysozyme in the deposit, Φ, is plotted in Figure 6.7 versus solution concentration, φ_L. The error bars on the plot correspond to the standard deviation in the data.

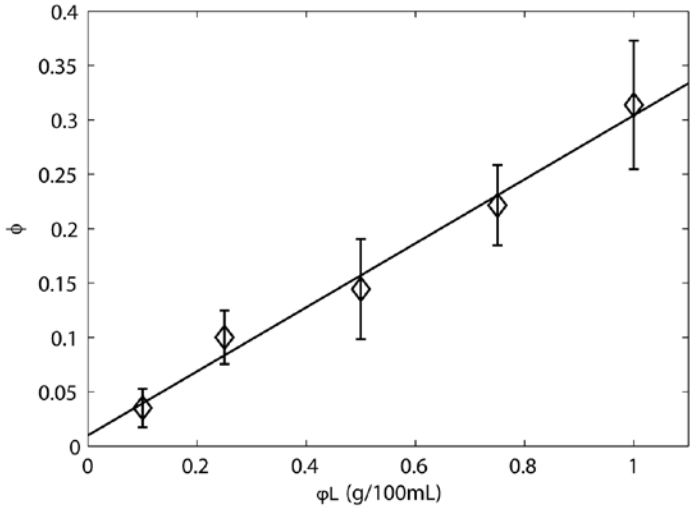

Figure 6.7. Mean volume fraction of the deposit, Φ, vs concentration, φ_L.

The data is linear with an R^2 value of 0.99. This suggests that while the total volume of the deposit is not concentration dependent and scales with diameter, the volume fraction of lysozyme within the deposited volume (the apparent density) increases linearly with concentration. This result becomes more remarkable upon examination of the actual values. The highest Φ observed is ~ 0.31 indicating that approximately 70% of the deposit is air or water. As Φ decreases, the fraction of open volume in the deposit increases correspondingly, leading to extremely porous deposits from the lowest concentration solution.

This set of experiments was repeated from fresh samples to verify this unexpected result. The repeated measurements were in very good agreement with the initial measurements (the most recent results are reported here). The stability of the deposits was examined by taking new AFM measurements of the same deposits after 1 week, 2 weeks, 1 month, and 2 months. The volume measurements during these time periods were identical within 2%.

6.6 DISCUSSION

To interpret the geometry and lysozyme packing of the deposits, it is reasonable to propose that the lysozyme solution drops undergo a gel transition during evaporation, and that this gel is packed more densely with increasing solution concentration. The gelation of lysozyme[101,134,135] can be brought about by changes in concentration, temperature, pH, and ionic strength, as well as the addition of a solvent. A transparent, viscoelastic gel matrix is often observed, with increasing bond character with increasing initial concentration.[135]

Similar gel transitions have been observed in related studies on the evaporation of sessile droplets of polymer solutions[27-29,92] and biological fluids[11,12] due to the effective increase in concentration during evaporation of the solvent. Recently, Sobac and Brutin investigated the phase transition in drops of whole blood, where a gel-like skin forms at the periphery of the drop while the "coffee ring" develops and the gelation front moves inward as evaporation proceeds. This is followed by a rapid gelation of the central area and then a decrease in evaporation rate while the remaining liquid in the deposit evaporates through the porous gel matrix.[12]

A similar line of reasoning can be used to describe the phase change in the aqueous lysozyme droplet. As the evaporation times of the micro- scale drops are on the order of seconds (too rapid for measurement in our laboratory), mm- scale drops of the same lysozyme/DI water solutions were used to illustrate the morphological evolution during evaporation. Videos were captured on the Keyence optical microscope during evaporation of droplets deposited via micropipette. Several frames illustrating the various stages of evaporation are given in the following Figure 6.8.

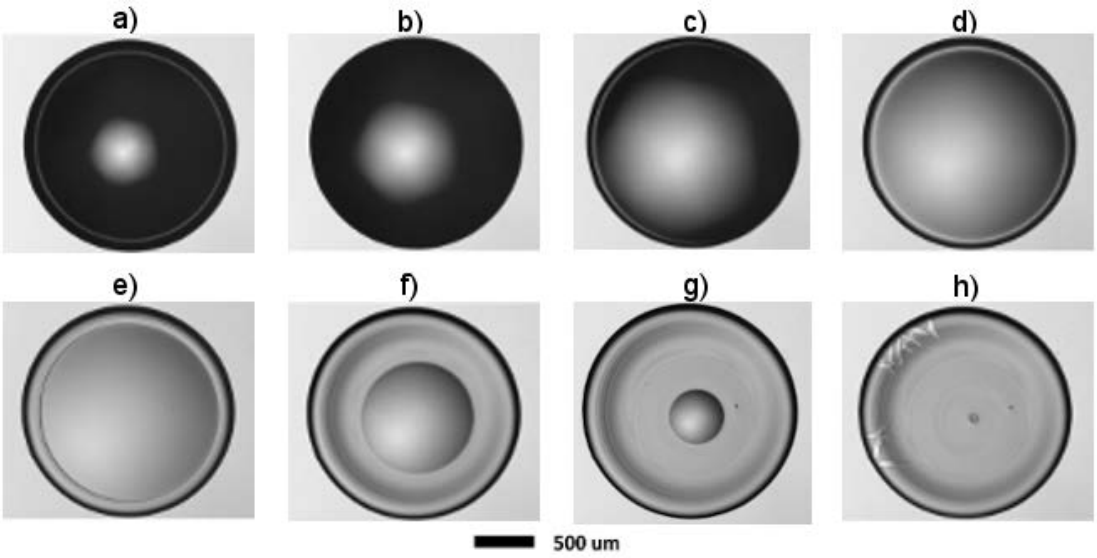

Figure 6.8. Sequential images during evaporation of a droplet with φ_L = 2.0 g/100mL at a) t ~ 1, b) 3, c) 4, d) 4.5, e) 5, f) 5.5, g) 5.75, and h) 6 minutes.

Radial flows carry solute to the perimeter of the drop, effectively increasing the concentration in the ring, which begins to gel (Fig. 6.8; a,b). Gelation continues toward the center of the drop which remains liquid (Fig. 6.8; c,d). Once the gel has formed at the periphery, creating the rim, and has proceeded toward the central area of the drop forming the typical crater-like shape, the remaining liquid depins from the gel (Fig. 6.8e) and recedes rapidly until the visibly remaining liquid is diminished and the gel has formed throughout the deposit. Finally, as the remaining liquid evaporates through the gel, the general shape is evident (Fig. 6.8h). Periodic surface cracks appear in the final stages of evaporation as a result of increasing stress in the deposit. These cracks increase in number as time continues (after visible evaporation is complete) until the deposit is stable. Cracking is not observed in deposits with D < 50 μm. The surface of this deposit was further examined with an optical surface profiler (Veeco/Wyko NT 1100) and given in Figure 6.9. The overall shape of the deposit is consistent with our observations in smaller drops and thus the evaporation process is assumed to be similar in the two size ranges.

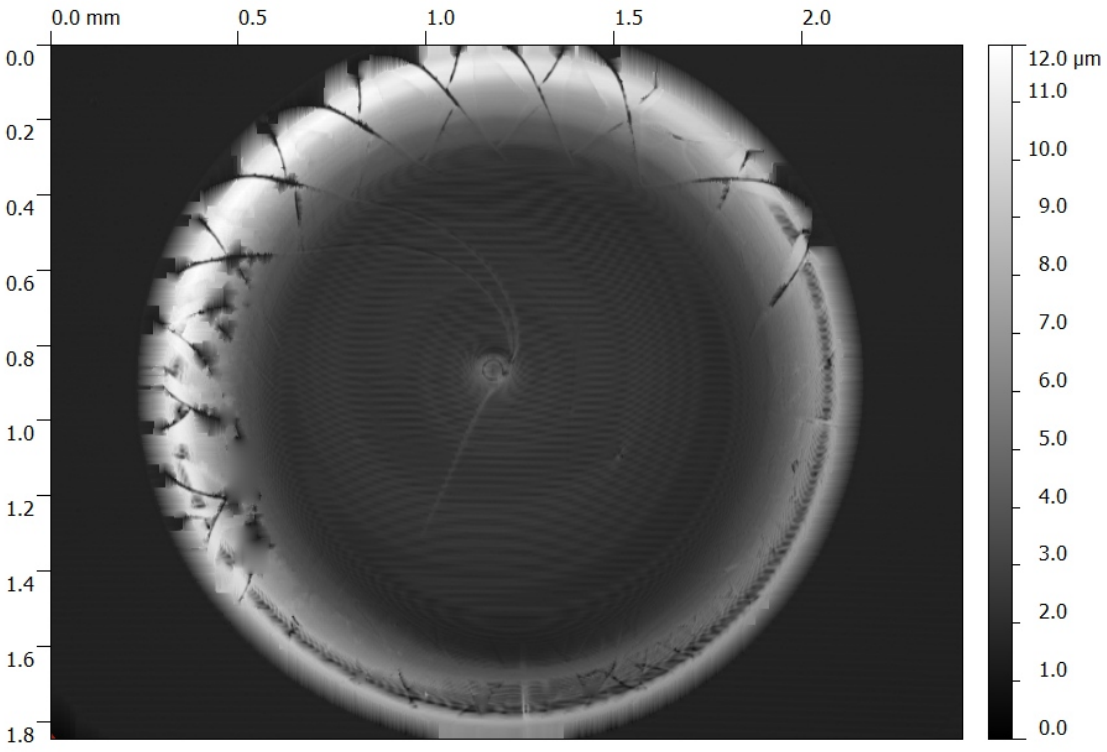

Figure 6.9. Topographical image of deposit in Figure 6.8.

This measurement was taken at least 24 hours after the images in Figure 6.8 and it is clear that the number of cracks in the surface increased. Periodic examination of these larger deposits via optical microscopy revealed that the number of cracks remained relatively stable after the first 24 hours, when stored in ambient conditions. The topographies of the large deposits were very similar to those measured by the AFM. Due to the nature of the measurement, there were some singularities in interpolating the height measurements, for example, the dark spots near the cracks in the ring area, as well as the darker looking ring at the periphery in Figure 6.9. These measurements are at the peak of the height profile, and were not properly interpolated. The dark secondary ring-like shape running from about 2 o'clock to 8 o'clock is a result of measurement error and does not reflect a real height change.

The shape evolution during evaporation and final deposit shapes were also documented using images acquired from the DSA. This shape evolution is illustrated in the sequence of images given in Figure 6.10. The images in Figure 6.10 correspond to the shape evolution of the droplet during evaporation as illustrated in Figure 6.8. The contact angle decreases linearly with time (Fig. 6.10; a – d) while evaporation proceeds. In Figure 6.10e, the gel formation in the ring along the perimeter is apparent and the remaining liquid depins. The remaining liquid in the droplet recedes rapidly (Fig. 6.10; e – i). The final deposit is shown in Figure 6.10i, and is generally similar to those shown in Figures 6.8 and 6.9 and to the micro- scale deposits in Figures 6.3 and 6.4.

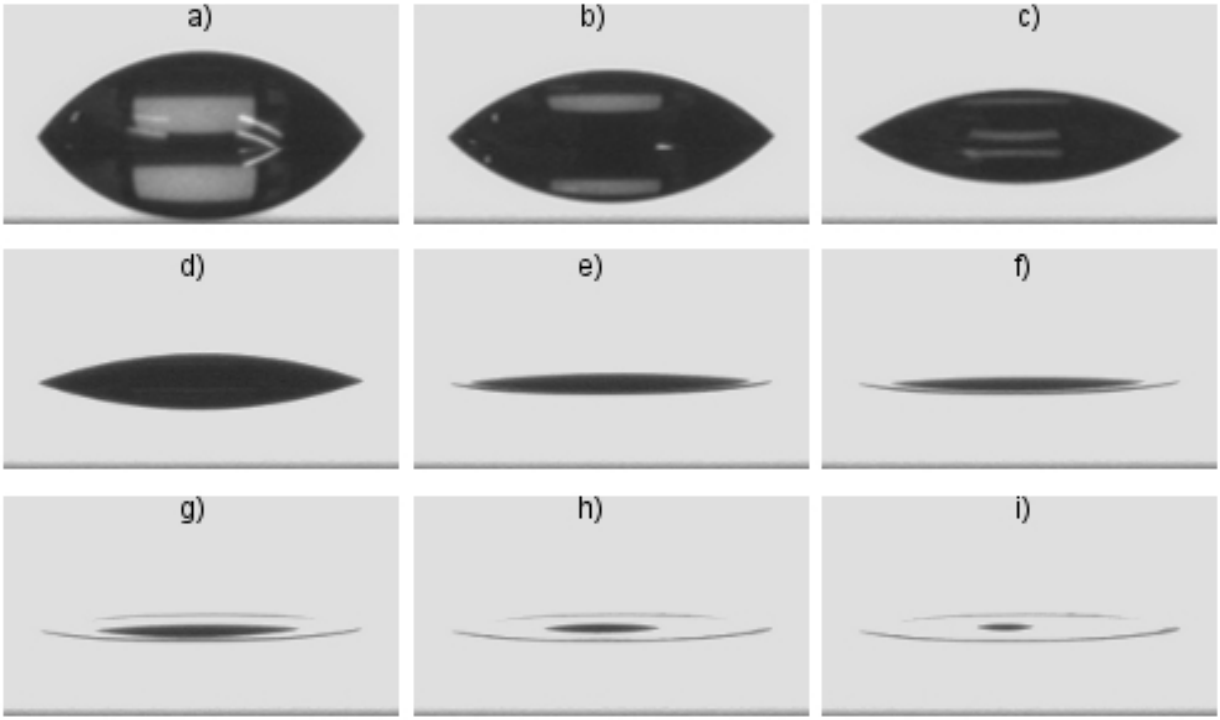

Figure 6.10. Shape evolution of lysozyme droplet (φ_L = 1.0 g/100mL) at times of a) ~1, b) 5, c) 10, d) 15, e) 20, f) 21, g) 22, h) 23, i) 24 minutes.

Unlike the flow-dominated coffee ring shapes of non-interacting particle systems, the shape of the lysozyme deposit is dictated by the shape of the droplet at the free surface. Based on the results from the pendant drop experiment (Section 6.1), lysozyme molecules adsorb to the vapor-liquid interface,[130-132] forming a loosely-packed, permeable "skin." This skin formation at the vapor-liquid interface has also been observed in biofluid droplets,[11,12] aqueous polymer solutions,[27-29,92] and suspensions of ellipsoidal latex particles.[26] Formation of a permeable skin tends to suppress the coffee-ring effect in these systems and the deposit shapes are dependent on the initial free surface profile. The final deposit shape can be predicted by solving the equations for hydrodynamic flow, highlighted in Chapter 2. The shape evolution predicted by these equations is further discussed in Chapter 7.

The initial shape depends only on the wetting diameter and the contact angle, which was equivalent for all concentrations in this study. As the coffee ring forms, the critical gelation concentration is reached at the periphery at and similar ring heights and widths are observed across the range of concentrations, determined by the decreasing contact angle. As evaporation proceeds inward, the lysozyme diffusion coefficient decreases due to self-obstruction and approaches kinetic arrest in the central region of the drop. The remaining liquid depins and recedes and the residual lysozyme in this liquid collects in the mound shape on top of the well-defined crater-like shape. Formation of this ring-like deposit shape is explored in more detail in Chapter 7.

7.0 CHARACTERISTIC SIZE FOR ONSET OF COFFEE-RING FORMATION IN EVAPORATING LYSOZYME SOLUTION DROPLETS[34]

7.1 DEPOSIT SHAPES

In the initial range of diameters studied for the lysozyme/DI water system (20 – 50 μm), the volume fraction of lysozyme in the deposit scaled linearly with initial solute concentration, but the basic geometry of the deposit varied little with a ten-fold increase in solute concentration. However, in surveying large numbers of lysozyme/DI water drop patterns by optical microscopy it became apparent that very small diameter drops did not produce the optical contrast expected for the coffee ring morphology. Very small drops seemed to form mounds or dome-shaped structures instead of rings. Although a recent study showed that a concentration and particle-size dependent critical diameter existed for ring formation in drops containing latex spheres,[23] little work exists on a minimum size condition for ring formation, particularly for fluids containing interacting particles.

To explore this observation in greater detail, small drops ranging from ~1 - 20 μm in diameter were deposited by the Omicron® nebulizer and characterized by AFM for lysozyme concentrations φ_L = 0.10, 0.25, 0.50, 0.75, and 1.0 g/100mL. Upon examination of drops with diameters, *D*, ranging from ~ 1 – 50 μm, two characteristic deposit morphologies were noted: a cap-shaped deposit in very small drops transitioning to the familiar ring-like deposit as *D*

increases. The generally observed cap and ring shaped deposits for φ_L = 1.0 g/100mL are illustrated in Figure 7.1 using two- and three-dimensional AFM topographic images and corresponding cross-sectional profile plots.

The cap and ring forms illustrated in Figure 7.1 were consistently observed throughout this study. Note that the z-axis scales in Figure 7.1 are in nanometers whereas the dimensions in the plane of the substrate are in microns. Both deposits are radially symmetric and cover the entire wetted area. The deposit in Figure 7.1a has the shape of a spherical cap with a maximum height of ~ 225 nm and shows no indication of ring formation. This shape is referred to as "cap-like" throughout this study. The typical "ring-like" deposit is illustrated in Figure 7.1b and similar to the shapes reported in Chapter 6.

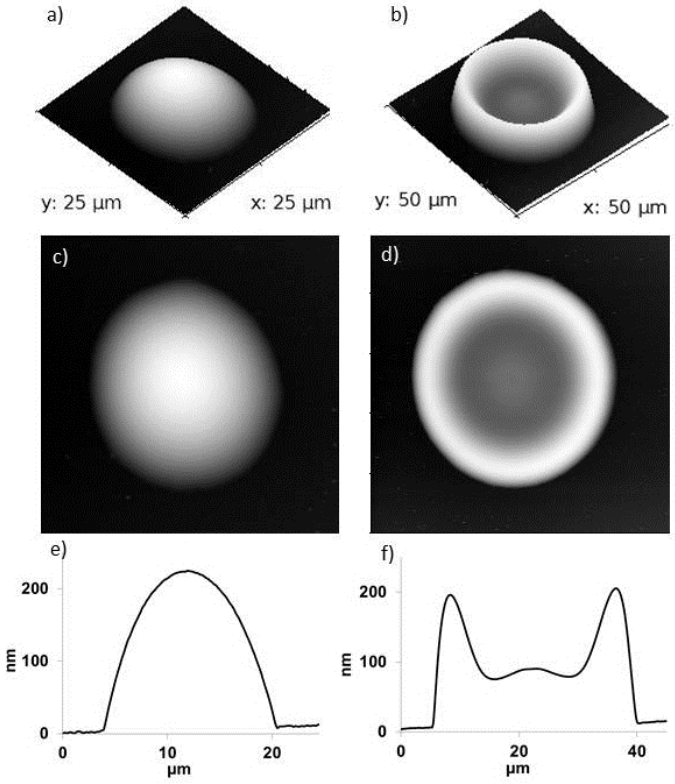

Figure 7.1. Representative morphologies for cap- and ring-like deposits with φ_L = 1.0 g/100mL.

7.2 CRITICAL DIAMETER FOR RING FORMATION

After surveying the shapes of a large number of drops of different sizes, it became clear that a transition from cap-like to ring-like deposits occurred at a well-defined *D*. This transition is illustrated in Figure 7.2 for drops with diameter, *D*, ranging from ~1 μm – 20 μm for solution concentration φ_L = 0.5 g/100mL.

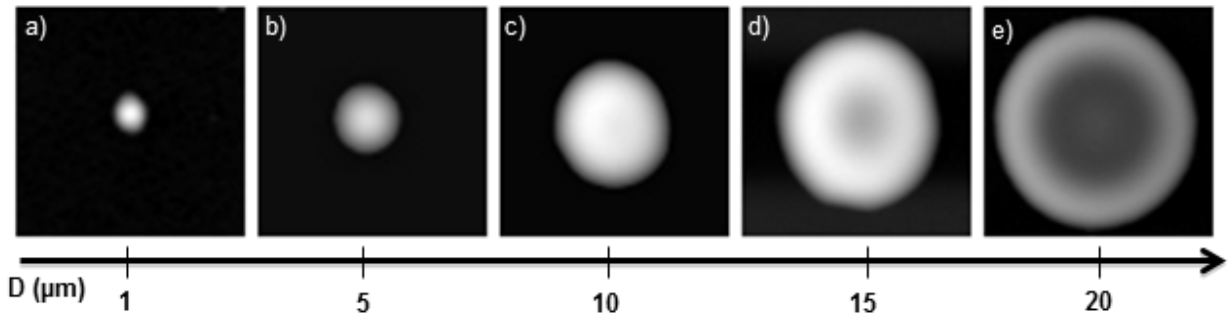

Figure 7.2. AFM topographic images of deposits (φ_L = 0.5 g/100mL) with increasing *D* (μm).

For this concentration, the ~ 1 and 5 μm deposits (Fig. 7.2; a-b) are below the minimum size for ring formation. At *D* ~ 10 μm (Fig. 7.2c), a very small, circular depression is visible in the central region of the deposit. The existence of a local minimum in the AFM cross section (not shown here) indicates the onset of ring formation in this system and is referred to as the critical diameter for ring formation, D_c. As *D* increases, the ring becomes more pronounced. For example, the 15 μm deposit (Fig. 7.2d) is ring-like with a circular depression in the center. The 20 μm deposit (Fig. 7.2e) has a well-defined ring-like shape with the typical undulation in the central region. This shape is consistent with the profiles found for all drops with $D > 20$ μm at this concentration. Although the transition between the cap and ring-like shapes is gradual, the deposit is referred to as "ring-like" if a local minimum exists in the central region of the deposit.

7.3 EFFECT OF CONCENTRATION

The transition between these two shape regimes was clearly observed in all concentrations studied. However, D_C, systematically increased with initial lysozyme concentration. To illustrate this phenomenon, representative drops from concentrations φ_L = 0.1, 0.5, and 1.0 g/100mL are collected in Figure 7.3 for D ~ 5, 10, 15, 20, and 25 μm.

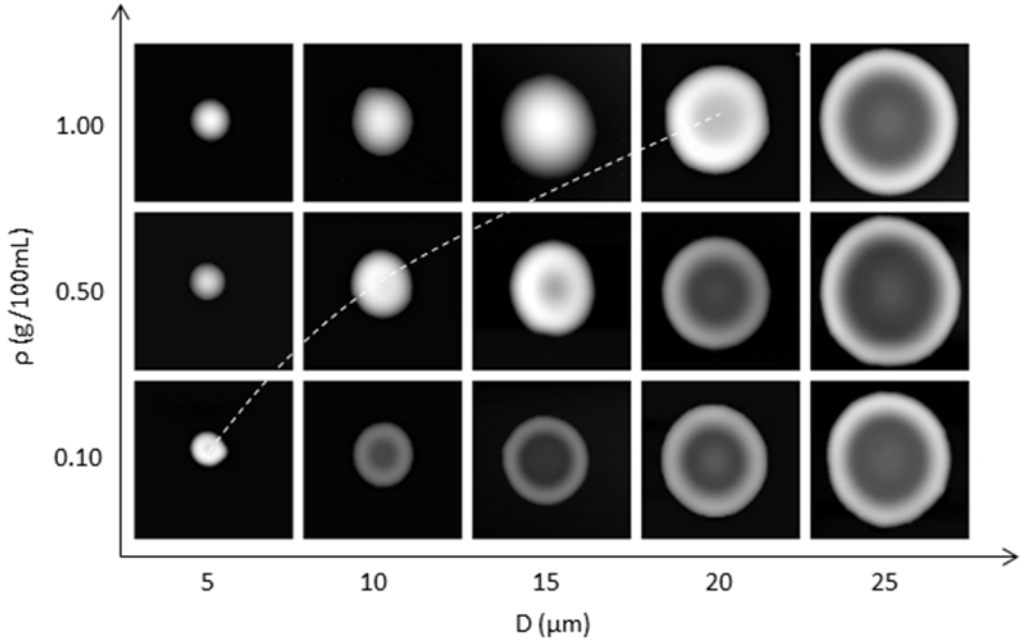

Figure 7.3. AFM topographic maps for droplets in rows with increasing φ_L and in columns from left to right with increasing D ~ 5, 10, 15, 20, and 25 μm.

The deposits are cap-like for all three concentrations when D < 5 μm. The coffee ring shape begins to form at a critical diameter, D_C, which depends on initial solution concentration and is indicated by the dotted line in Figure 7.3. As the concentration increases, D_C increases. The drops with D ~ 25 μm have very similar topography, independent of concentration. To examine these shapes more closely, AFM cross sectional profiles are presented in Figure 7.4.

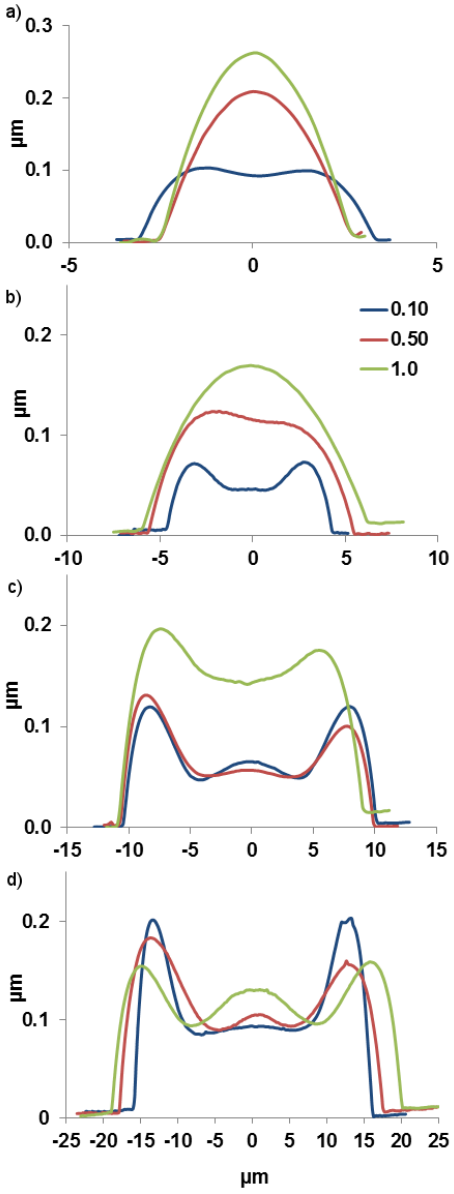

Figure 7.4. AFM cross sectional profiles for deposits with D ~ a) 5, b) 10, c) 20, and d) 30 µm for φ_L = 0.1, 0.5, 1.0 g/100mL.

The profiles of the smallest drops in Figure 7.4a (D ~ 5 µm) have cap-like shapes for φ_L = 0.5 and 1.0 g/100mL, but the shape has a local minimum in the center for the lowest concentration (φ_L = 0.1 g/100mL), indicating the development of a ring. This is considered the critical diameter, D_C, for the φ_L = 0.1 g/100mL concentration. In Figure 7.4b, the 0.5 g/100mL deposit

has a local minimum in the center, indicating ring formation. The 0.1 g/100mL deposit has a well-defined ring shape while the highest concentration deposit (1.0 g/100mL) has a cap-like shape at this diameter. In Figure 7.4c, the highest concentration deposit has a local minimum, indicating ring formation. The two deposits with lower concentrations exhibit the well-defined ring like shape with the central mound. Despite the difference in concentration, these two deposits are quite similar in shape. This is illustrated further in Figure 7.4d, which contains the cross-sectional profiles for drops with $D \sim 30$ μm. All three concentrations have deposits with similar ring-like shapes. These patterns show negligible concentration dependence in the geometry of the deposit for drops with $D > 25$ μm for all concentrations in this study. This observation is consistent with the findings from the initial study (presented in Chapter 6) for drops with $30 \leq D \leq 50$ μm.[33]

7.4 DISCUSSION

7.4.1 Ring Formation

Formation of the ring-like deposit is discussed in Chapter 6 and Reference [33] and is briefly summarized here. When the droplet is deposited, lysozyme molecules adsorb to the Si wafer substrate, pinning the droplet. The liquid drop maintains a spherical cap shape and the contact angle decreases during evaporation. Radial flows carry un-adsorbed molecules to the perimeter of the drop where the flux is the highest, consistent with the "coffee ring effect." Simultaneously, lysozyme molecules collect at the air-water interface,[130-132] forming a loosely-packed, permeable skin. Lysozyme molecules accumulate at the periphery, undergoing a gel

transition which proceeds inward toward the center of the drop. The contact angle continues to decrease until a critical angle, θ_r, is reached. At this point, the remaining liquid depins and recedes toward the center of the drop. The residual lysozyme in this liquid collects in the mound shape on top of the gel structure, forming the well-defined ring-like shape.

In the initial study,[33] it was noted that the ring-like deposit geometry is quite similar for all concentrations, but the volume fraction of lysozyme molecules in the deposit increased linearly with initial solution concentration. As lysozyme collects at the periphery, the critical gelation concentration is reached in the ring. Similar ring heights and widths are observed across the range of concentrations, determined by the geometry of the liquid droplet during evaporation and the angle at which the depinning event occurs, θ_r.

7.4.2 Particle Transport

The deposits in this study are clearly influenced by the characteristic time and length scales of the experiment. Macroscopic models of evaporation are assumed to be applicable in this case, as the mean free path of the vapor molecules is significantly less than the length scale in this experiment and therefore within the regime of continuum mechanics. The droplet evaporation time can be estimated using the evaporation model proposed by Popov:[18]

$$\tau_{evap} = \frac{\pi \rho_L R^2 \theta_0}{16 D_V (c_o - c_\infty)} \tag{7.1}$$

where D_V is the diffusion coefficient of the vapor in air, c_o is the density of saturated vapor immediately above the liquid-air interface, c_∞ is the ambient vapor density, ρ_L is the liquid density, θ_0 is the initial contact angle, and R is the drop radius. Based on the parameters of this

experiment, the evaporation times are on the order of seconds. The velocity of the radial flow is estimated by $u \sim j/\rho_L$, where j is the solvent evaporation rate and is given by: [20]

$$j(r) = \frac{2}{\pi}\frac{D_V(c_0 - c_\infty)}{\sqrt{R^2 - r^2}} \quad 7.2$$

In this experiment, $u \sim 8$ μm/s, which is consistent with particle velocities in evaporating biofluid drops.[11]

To determine the time and length scales for lysozyme diffusion, the mean displacement of lysozyme monomers during evaporation, X_L, is determined. This is estimated using the Stokes-Einstein equation and the expected diffusion coefficient for lysozyme monomers in solution,[115] $D_L \sim 1 \times 10^{-10}$ m^2/s:

$$X_L = \sqrt{(6D_L\tau_{evap})} \quad 7.3$$

The mean displacement due to diffusion can be compared to two other length scales, the mean spacing of molecules in solution and the size of the drop. Assuming a homogeneous distribution of lysozyme particles in solution, the mean distance between two lysozyme monomers in the liquid suspension, λ_L, is estimated by

$$\lambda_L = \sqrt[3]{\frac{V_L}{n_L}} \quad 7.4$$

where V_L is the volume of the liquid drop and n_L is the number of lysozyme molecules in the liquid drop per unit volume. V_L is determined using an initial contact angle of ~ 55° and assuming the contact diameter is equal to the deposit diameter. The number of lysozyme molecules per unit volume, n_L, is estimated from the initial solute concentration. Considering the lysozyme concentrations in this experiment, λ_L ~ 10 - 30 nm and based on the estimated evaporation time for a drop with D = 50 μm, we find a maximum X_L of ~ 15 μm. Thus, this

system can be considered “crowded” for the solution concentrations and drop diameters studied, as the average spacing of lysozyme molecules in solution is much less than mean-squared displacement of particles over the time scales of the experiment.[115] In other words, to travel the characteristic length, every lysozyme molecule will travel many times the nearest neighbor distance and potentially interact with many other lysozyme molecules. During evaporation, the effective concentration of lysozyme within the drop increases and the diffusion coefficient will decrease due to self-obstruction in the crowded system. As the diffusion coefficient approaches zero, the system approaches kinetic arrest and the sol-gel transition takes place at the critical concentration for gelation, φ_g.

7.4.3 Shape Transition

Uniform, dome-like,[2,25,64,65] and pillar-like deposits[136,137] have been observed in a number of systems and were predicted based on consideration of the dominant transport mechanisms in the droplet. For example, uniform deposits occur when Marangoni convection dominates over radial flow[2,64,65] and when DLVO interactions between the particles and substrate dominate over the radial outward flow and Marangoni convection.[25] The deposit shape has also been predicted numerically based on the ratio of the initial and gelation concentrations in polymer solutions.[29] A dome-like shape resulted when the radial flow was suppressed due to gelation in drops with higher initial polymer concentrations.

The deposit shape has recently been discussed by comparing the representative time scales for evaporation and diffusion.[23,137] This reasoning is employed here in describing the lysozyme deposit shape regimes. The shapes can be analyzed in terms of the competition between advection and diffusion of the lysozyme molecules. In the pinned droplet, unadsorbed

lysozyme molecules will be influenced by the radial capillary flow, which is opposed by particle diffusion. For the ring to form, the "coffee ring effect" must be greater than the effect of diffusion. A more homogeneous deposit would be expected when diffusion dominates over capillary flow.

The competition between advection and diffusion can be examined using the dimensionless Peclet number, *Pe*. Following the solutions and scaling of the Navier-Stokes equations[41] (Chapter 2),

$$Pe = \frac{uL}{D_L} \tag{7.5}$$

where u is the particle velocity, L is the characteristic size of the system, and D_L is the particle diffusion coefficient. In general, when $Pe >> 1$ advection dominates transport and when $Pe << 1$, diffusion is the dominant mechanism.

To find the Peclet number in this system, the radial velocity is estimated by $u \sim j/\rho_L$, where j is the solvent evaporation rate determined by Equation 7.2, and ρ_L is the liquid density. In this experiment, the radial velocity is estimated as u = 8 μm/s, which is consistent with radial flow velocity in evaporating biofluid drops.[11] The radius of the drop, R, is taken as the characteristic length of the system, L, and the reported diffusion coefficient of lysozyme monomers is $D_L \sim 1 \times 10^{-10}$ m^2/s.[115] It should be noted that lysozyme concentration, crowding effects, and phase transition phenomena during evaporation are not considered in the calculation of the Peclet number in this study.

Based on the above assumptions, the Peclet number for the range of diameters in this experiment is Pe = 0.05 – 2.0. The range of Peclet numbers at this scale indicates that both advection and diffusion are occurring in competition. The Peclet number, *Pe*, was determined for all deposits examined in this experiment and is plotted in Figure 7.5 as a function of φ_L.

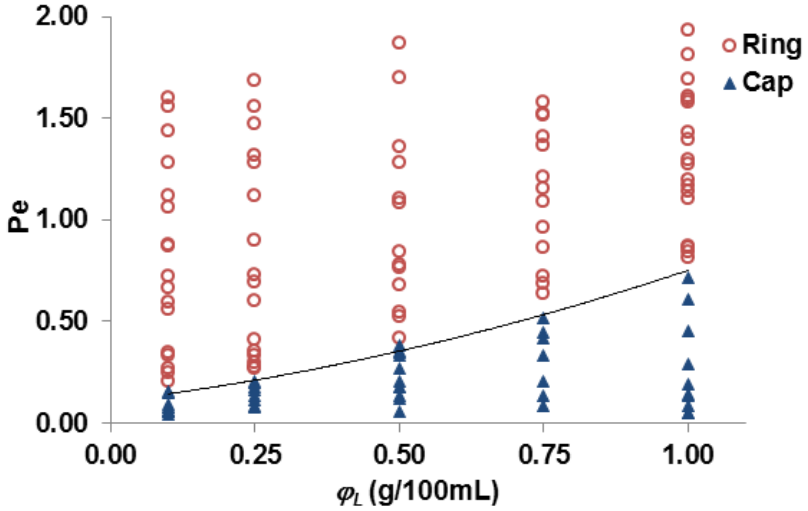

Figure 7.5. Plot of Peclet numbers for φ_L = 0.1, 0.25, 0.5, 0.75, and 1.0 g/100mL.

Several trends can be seen in Figure 7.5. The deposits with a ring-like shape are indicated with a circle and the cap-like shapes are indicated with a triangle. The transition between the deposit regimes for each concentration is indicated by the fit line. The deposits with $Pe < 0.20$ for all concentrations have cap-like shapes, while all of the deposits with $Pe > 1$ are ring-like. Between $Pe \sim 0.20 – 0.80$, the transition occurs at different values depending on the concentration.

In this system, a Peclet number of 1 corresponds to a characteristic length of 12.5 μm, or $D = 25$ μm. This is generally consistent with our experimental observations, as the deposits with $D > 20$ μm (corresponding to $Pe > 1$) have ring-like shapes. In other words, when the Peclet number is greater than 1 in this system, advection is dominant, which drives ring formation. As $Pe \rightarrow 0$, diffusion becomes more dominant, which is also consistent with our observations. The absence of the coffee ring in very small drops (with low Pe) indicates that diffusion is the dominant transport mechanism in this case.

7.4.4 Deposit Contact Angle

In ring-like deposits, the lysozyme collects at the periphery and begins to gel. When the contact angle reaches the critical angle, θ_r, the liquid depins and recedes, leaving deposits with similar volume and geometry, independent of initial concentration (higher initial lysozyme concentrations yield more densely packed final deposits). For the cap-like shapes, this behavior is different. Though the general shape is similar for all cap-like deposits, the AFM measured contact angle of the deposit (and therefore the volume of the cap) increases with solution concentration. We propose that when $D < D_C$ (cap-like deposits), the gelation concentration throughout the deposit, φ_g, is reached before the receding contact angle, θ_r, is reached, and the time to reach φ_g decreases with concentration. To examine this idea further, the contact angle of the final deposit, θ_D, was determined by fitting the AFM cross sectional profiles to a spherical cap shape and taking θ_D as the maximum angle with the horizontal. An example of this measurement is given in Figure 7.6. The values of θ_D are plotted in Figure 7.7 as a function of D for the deposit shapes observed in this study.

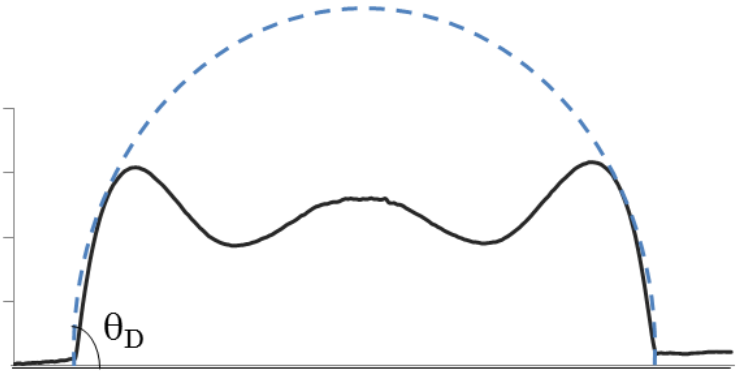

Figure 7.6. Schematic of deposit contact angle measurement, θ_D.

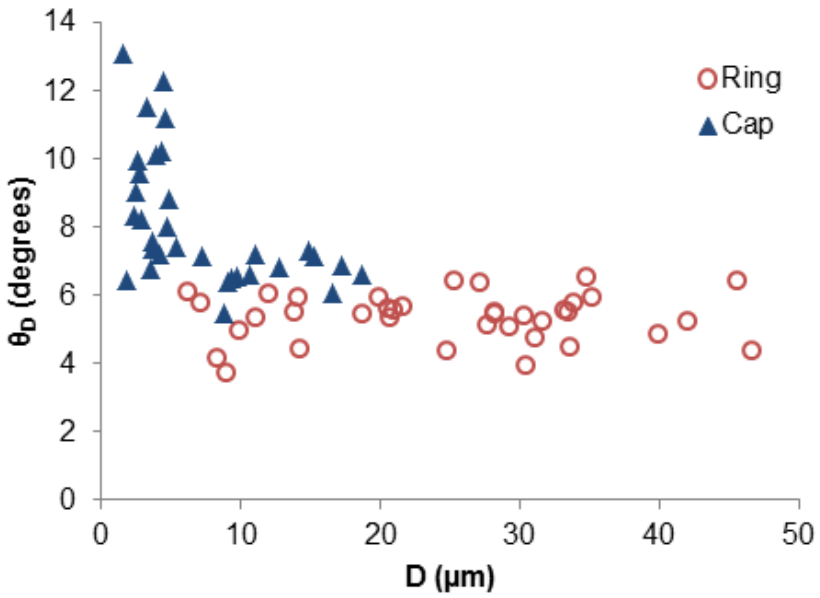

Figure 7.7. Deposit contact angle, θ_D, vs. D for all concentrations.

In ring-like deposits, θ_D varied within a narrow band from approximately 3° - 6° for all concentrations. The contact angles of the cap-shaped deposits are larger, ranging from ~ 6° - 15°, depending on diameter and initial solution concentration. In cap-like deposits, the angle increased with solution concentration. Based on these observations, the critical receding contact angle is assumed to be θ_r ~ 6°. The scatter in the data likely reflects typical experimental error such as local substrate heterogeneities and slight variations in concentration and evaporation rate from droplet to droplet due to the nature of the deposition process.

In general, cap-like deposits are formed when the gel transition occurs before the drop shape reaches θ_r. In the case of the evaporating droplet, the diffusion coefficient is dependent on concentration and time. Due to crowding and DLVO interactions, the lysozyme diffusion coefficient decreases with increasing concentration.[115,116] In drops with higher initial protein concentrations, there is a higher degree of self-association and the system will reach kinetic arrest before the more dilute concentrations. Therefore, the droplets with higher initial lysozyme

concentrations will undergo the gel transition at an earlier time in the evaporation process. The diameter for ring formation, D_C, is thus larger in solutions with higher initial lysozyme concentrations.

This can be further explained by examining the final deposit shape for a variety of concentrations. The final shape transition can be predicted by solving the equations for hydrodynamic flow (Navier-Stokes and continuity equations, given in Chapter 2). To model the height profile, the concentration profile $\phi(r,t)$ is determined by solving Equation 2.21 with the boundary conditions in Equation 2.20. This concentration profile is given by:

$$\phi(r,t) = \phi_0 \frac{b^{-\frac{1}{2}}(t) - r^2}{1 - r^2} \tag{7.6}$$

where $b(t) = 1 - 2t$.

To consider gelation of the lysozyme in this model, two time regimes are considered: the pregelation and postgelation regimes. The pregelation regime occurs at early times when the gel-like phase does not appear ($\phi < \phi_g$). The gel phase region begins to form when $\phi = \phi_g$ along the perimeter of the droplet. The height, $h(t)$, and position, $r(t)$, of the of the gel front are determined and the final shape of the film after drying is estimated by the trajectory $[r(t), h(t)]$ at $t = t_f$. This produces the expression for the final shape:[29]

$$h = \frac{\Phi^{-1}(1 - r^2)}{[r^2 + \Phi^{-1}(1 - r^2)]^3} \tag{7.7}$$

where $\Phi = \varphi_o/\varphi_g$. The shape of h changes with the value of Φ and is plotted in Figure 7.8 for values of Φ ranging from 0.2 to 1.0 and Pe = 1. The shapes predicted in Figure 7.8 are quite similar to those observed experimentally in this study. For deposits with a similar diameter, when the initial concentration is closer to the gelation concentration, the resulting shape is cap-like, while lower initial concentrations have ring-like deposit shapes.

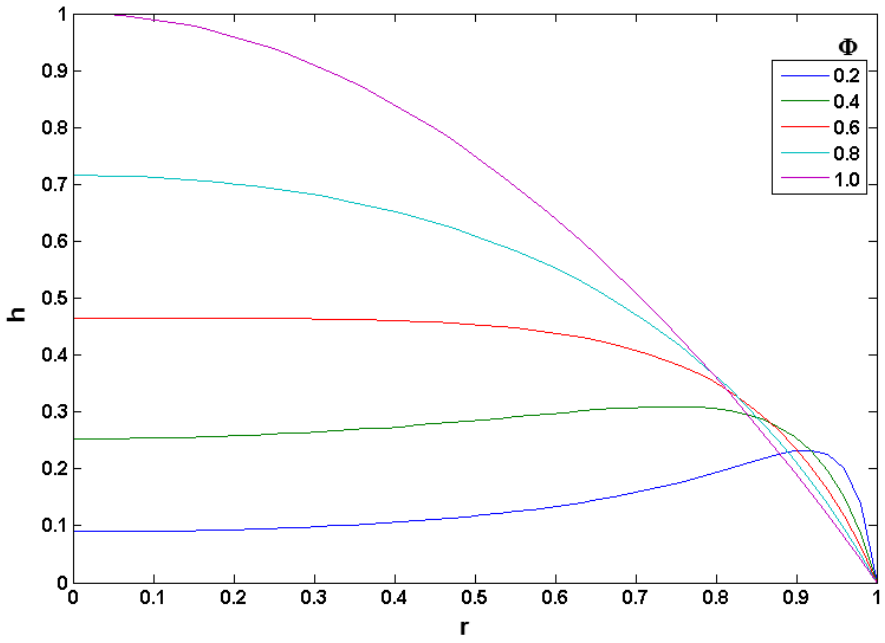

Figure 7.8. Numerical prediction of the final deposit shape, *h*, as a function of *r*.

8.0 EFFECT OF SUBSTRATE TEMPERATURE ON EVAPORATING LYSOZYME SOLUTION DROPLETS

In the investigation of the final deposit patterns of lysozyme and DI water solutions, the geometry of the deposit and therefore the evaporative dynamics and kinetics of the system are highly influenced by the initial system parameters. Recent studies on droplet evaporation have incorporated thermal effects, which were found to influence the evaporation rate and accompanying evaporative flows within the fluid droplet.[71,72,73] Heating the substrate modifies the temperature gradients at the solid/liquid and liquid/vapor interfaces, which affects the evaporative dynamics of the system and therefore pattern formation in the evaporating lysozyme droplet.

8.1 GENERAL OBSERVATIONS

To determine the effect of substrate temperature on evaporating lysozyme droplets, clean Si wafers were heated on a digital hot plate (EchoTherm, HP30) to substrate temperatures, T_S, of 30, 50, and 80°C. The substrates were held at the temperature of interest for 10 minutes. Drops were then deposited via the Preval® aerosol spray system (with the substrate remaining on the hot plate) and removed from the heat after 60 seconds. Optical microscopy and AFM were used to characterize the deposits. Representative examples of three deposits with φ_L = 0.5 g/100mL

and prepared at substrate temperatures, T_S, of 30, 50, and 80°C, are illustrated in Figure 8.1. These three deposits have diameters of ~ 40.8, 43.9, and 45.3 μm and similar deposit volumes of ~ 235 μm^3 for comparison.

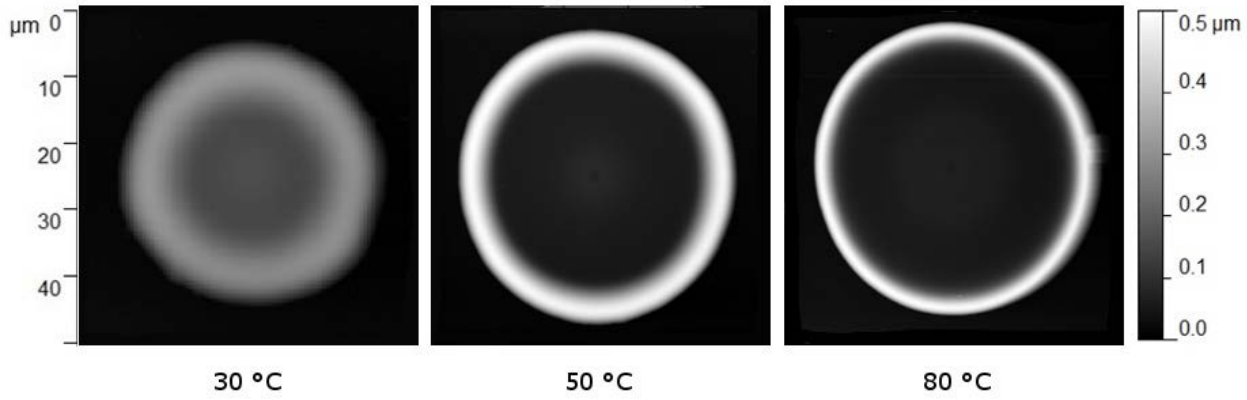

Figure 8.1. Representative morphologies with φ_L = 0.50 g/100mL at T_S = 30, 50, and 80°C.

The general behavior shown in Figure 8.1 was observed in the lysozyme deposits throughout this study. The overall shapes of all deposits are smooth, radially symmetric, and have a single peripheral ring. The deposits with T_S = 30°C exhibited the general behavior observed in lysozyme solution droplets that evaporated under ambient conditions (Chapter 6).[33] The deposits with T_S = 50 and 80°C have similar ring-like shapes, but the ring becomes narrower as the substrate temperature increases. In addition, much less solute remains in the central region of these deposits with higher substrate temperatures. The peak height of the ring also increases as the substrate temperature increases, as illustrated by the grayscale color map in Figure 8.1. To examine the deposit geometry more closely, the AFM cross-sectional profiles for the deposits in Figure 8.1 are presented in Figure 8.2.

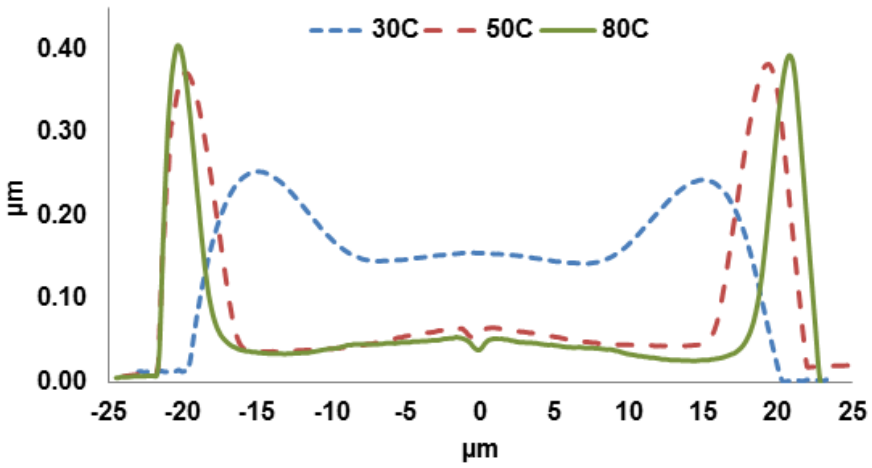

Figure 8.2. AFM cross-sectional profiles of the three deposits in Figure 8.1.

The cross-sectional profiles in Figure 8.2 reveal the deposit geometry in more detail, which clearly changes as substrate temperature increases. The deposit at 30°C has the familiar ring-like profile shape with a slight undulation in the central region of the deposit. The deposit profiles of drops at 50 and 80°C are somewhat different, with narrow ring regions and peak heights much greater that of the 30°C deposit. The deposits at 50 and 80°C also have a greater deposit angle than the 30°C deposit. The central regions of the 50 and 80°C deposits are much thinner, with thicknesses nearly half that of the 30°C deposit. Though much thinner, these central regions still have a slight undulation and small depression in the center.

After observing many deposits at each temperature, the mean diameter of the deposits increased with substrate temperature. This observation is attributed to a decrease in the initial contact angle with heated substrates. This was examined more closely by Drop Shape Analysis (DSA) of drops deposited on the heated substrates. While the room temperature deposits had contact angles near ~ 55°, the contact angles of drops on heated substrates, ranged from ~ 40 - 50°, and decreased as the substrate temperature increased.

8.2 EFFECT OF CONCENTRATION

The effect of substrate annealing was examined for drops with concentrations φ_L = 0.10, 0.50, and 1.00 g/100mL for comparison. The overall deposit shapes were similar for all concentrations studied. For the range of concentrations in this study, the ring width decreased and the peak ring heights increased with substrate temperature. The central regions of the deposits also contained much less solute when T_S = 50 and 80°C for all concentrations. However, slight differences in the morphologies with concentration were apparent for the drops deposited at 50 and 80°C. Representative deposits with concentrations of φ_L = 0.10, 0.50, and 1.00 g/100mL at T_S = 50°C are given in Figure 8.3.

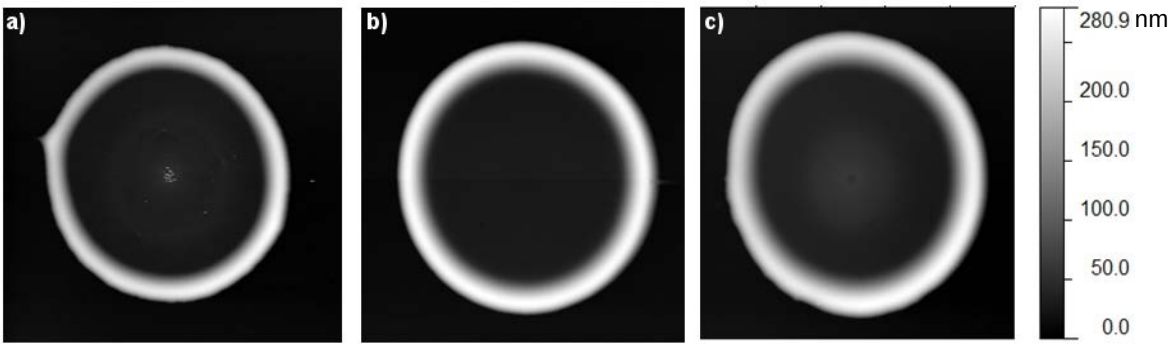

Figure 8.3. Representative deposits with T_S = 50°C for drops with concentrations of a) 0.10, b) 0.50, and c) 1.00 g/100mL.

In the deposits with T_S = 50 and 80°C, the width of the ring increased with concentration, unlike the drops deposited at room temperature (Chapter 6). To examine this relationship further, the ring width, *w*, was measured for all deposits in this study. The relative width of the ring (normalized by the deposit diameter), *w/D*, is plotted in Figure 8.4 versus concentration for T_S = 30, 50, and 80°C.

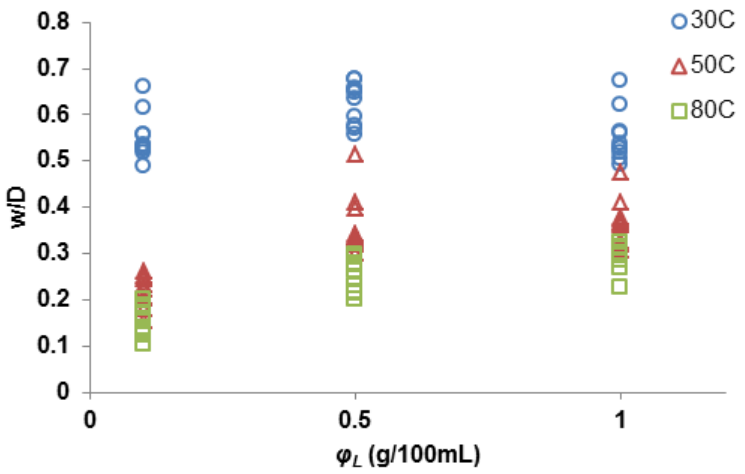

Figure 8.4. Ring width normalized by diameter, *w/D*, vs. φ_L at T_S = 30, 50, and 80°C.

Figure 8.4 illustrates the relative ring width as a function of concentration for the three different substrate temperatures. The relative width for deposits with 30°C is similar across the range of concentrations in this study. This is consistent with our previous observations of deposits on room temperature substrates and ambient evaporation conditions (Chapter 6).[33] The deposits with substrate temperatures of 50°C have an intermediate range of relative widths, lower than that of the 30°C substrates. In addition, the mean relative width for the 50°C deposits increases with concentration. This is also true for the 80°C deposits, which have even lower relative widths.

8.3 DISCUSSION

Substrate annealing clearly affects pattern formation in the lysozyme/DI water droplet system. The peripheral rings are much more pronounced in drops deposited on heated substrates. In addition, the thickness in the central region of the deposits on annealed substrates is much less

than the room temperature deposits, suggesting that more lysozyme reaches the periphery when the substrate temperature is increased. Manipulating the substrate temperature affects the initial geometry and the fluid dynamics within the droplet and therefore affects the final deposit pattern.

The effect of substrate temperature on droplet evaporation has been previously studied for systems of pure water[70-73] as well as drops containing nanoparticles[74] and polymers.[75] In experimental studies using IR thermography,[76] evaporation of water droplets were observed on heated substrates. Global heating of the droplet was observed during evaporation, though the drop apex remained cooler than the fluid near the contact line for most of the evaporation process. Heating substrates will also cause an increase in the droplet evaporation rate.[22,70] It was also determined that heated substrates caused depinning and receding of pinned water droplets to occur at an earlier time in the evaporation process.[71,72] In the lysozyme/DI water droplet system, similar reasoning is employed to explain the effect of substrate temperature on pattern formation.

Lysozyme solution drops deposited on heated substrates tend to have lower contact angles than the drops deposited at room temperature, based on drop shape analysis. The surface tension of water is known to decrease as temperature increases which would also lead to the decrease in contact angle with substrate temperature.[138] Furthermore, the overall evaporation rate increases as the substrate temperature increases. This results in an increase in evaporative flux near the contact line and consequently an increase in the rate of fluid flow within the droplet. It should also be noted that the unfolding temperature of lysozyme is 83°C, so we assume that the increase in substrate temperature changes the wetting properties and dynamics within the system and not the structure of the lysozyme molecule itself.

To examine the effect of substrate temperature more closely, the heat equation is solved for both the droplet and the substrate to observe heat transfer within the droplet. Assuming a perfect thermal contact between the drop and the substrate, the dimensionless heat equation can be written as[70]

$$c_p^* \frac{\partial T}{\partial t} - \frac{1}{PrRe} \nabla^2 T = 0 \tag{8.1}$$

where c_p* is the dimensionless heat capacity, and the dimensionless Prandtl, *Pr*, and Reynolds, *Re*, numbers are given by:

$$Pr = \frac{c_p \mu}{k} \tag{8.2}$$

$$Re = \frac{\rho u L}{\mu} \tag{8.3}$$

The velocity, *u*, is taken as 8 μm/s and the characteristic length, *L*, is taken as the droplet radius, as in Chapter 7. The thermophysical properties of pure water, used as the parameters in this calculation, are collected in Table 8.1. The dimensionless temperature, *T*, is defined as

$$T = \frac{T_i - \min(T_{1,0}, T_{2,0})}{\left| T_{1,0} - T_{2,0} \right|} \tag{8.4}$$

where $T_{1,0}$ and $T_{2,0}$ are the initial temperature of the drop (i = 1) and the substrate (i = 2), respectively. The boundary conditions for this equation can be written as:

$$\frac{\partial T}{\partial r} \hat{n}_r + \frac{\partial T}{\partial z} \hat{n}_z = 0 \text{ at } R = 0,\ z = 0 \tag{8.5}$$

and the initial conditions for the droplet and substrate temperatures are:

$$T_{1,0}(r, z, 0) = 30℃\,,\ \ T_{2,0}(r, z, 0) = 50℃. \tag{8.6}$$

In dimensionless form, these initial conditions are taken as

$$T_{1,0}(r, z, 0) = 0\,,\ \ T_{2,0}(r, z, 0) = 1. \tag{8.7}$$

Table 8.1. Thermophysical properties of pure water at 25°C.

Property	Value
Density, ρ_L (kg m^{-3})	997
Thermal conductivity, κ (W m^{-1} K^{-1})	0.607
Heat capacity c_p (J kg^{-1} K^{-1})	4180
Viscosity, $\mu(T)$ (Pa s)	$(-0.0026T^3 + 0.5874T^2 - 47.598T + 1763.4) \times 10^{-6}$

The heat equation (Equation 8.1) was solved in the sessile droplet geometry with substrate temperatures of 30, 50, and 80°C using MATLAB®. Figure 8.5 shows the temperature profile within the droplet after 1 second for a substrate temperature of 50°C. Based on this temperature profile, the droplet is clearly heated in the vicinity of the contact line after 1 second. The elevated temperature, especially near the periphery of the droplet adds to the nonuniformity of the evaporative flux profile. The evaporation rate increases and therefore, the outward radial flow velocity increases.

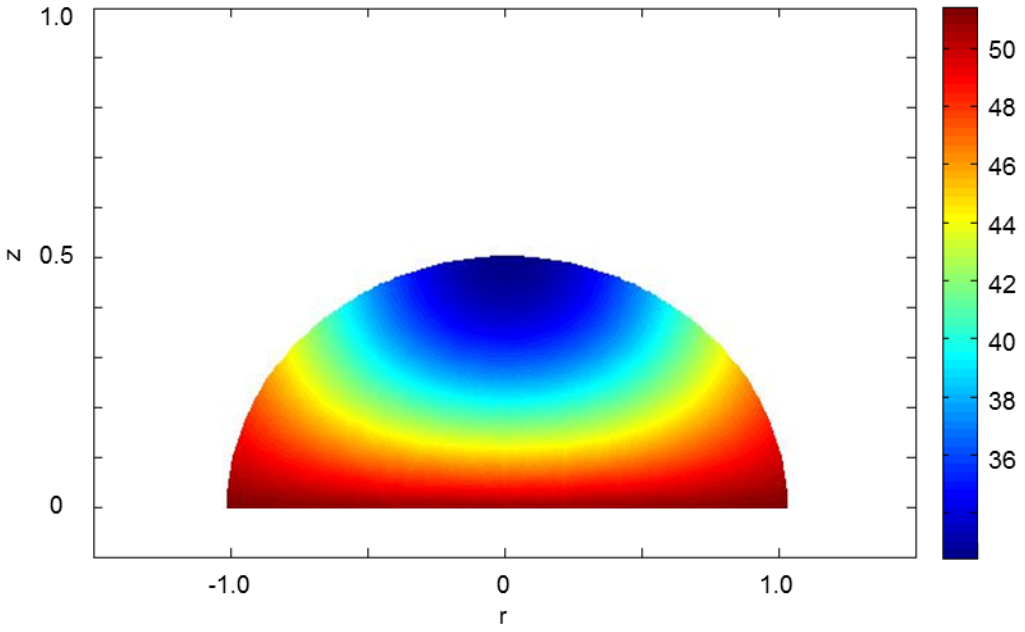

Figure 8.5. Temperature profile within sessile droplet after 1 second with T_S = 50°C.

The amount of adsorption is expected to decrease with increasing temperature for this system. Here, we assume DLVO (Derjaguin, Landau, Verwey, and Overbeek) interactions between the positively charged lysozyme molecules and negatively charged SiO_2. The DLVO theory combines short range Van der Waals and longer range electrostatic interactions in a liquid medium. In general, the lysozyme molecules are strongly attracted to the substrate and form a self-assembled monolayer. Additional layers form and the electrostatic attraction between the molecules and the substrate decreases with layer thickness. As the number of layers increases, the positively charged lysozyme molecules tend to repel one another. Unadsorbed lysozyme molecules are free to diffuse or to be transported to the periphery by the convective flow.

While the first few monolayers will undoubtedly have a strong enough electrostatic interaction to keep the droplet pinned, increasing the substrate temperature provides additional kinetic energy to help the molecules escape from the substrate. In addition, since the solid-liquid interfacial temperature is higher than the liquid-vapor interfacial temperature, the lysozyme molecules near the substrate will tend to diffuse away from the substrate, according to Fick's first law. Therefore, more molecules will be unadsorbed and able to reach the periphery of the drop by the fluid flow, which is increased by the increase in evaporative flux. This results in higher ring peaks and thinner central regions of the deposits at elevated substrate temperatures.

The relative ring width is dependent on concentration for the 50 and 80°C substrate temperatures, but is not dependent on concentration for 30°C. This is consistent with the observations collected in Chapters 6 – 7 for room temperature droplets, which have similar *w/D* measurements without concentration dependence. With increased substrate temperature, the lysozyme molecules are less affected by diffusion and substrate influences and less affected by crowding of the system. Therefore, more lysozyme will reach the periphery before jamming and

undergoing the phase transition for all concentrations. This behavior is more like the typical coffee ring effect for colloidal particles where the majority of the solute reaches the periphery and little (or no) solute remains in the central region. Therefore, with higher concentrations, even more solute is capable of transport and thus more solute builds up at the ring before the gel transition takes place.

9.0 SALT-INDUCED PATTERN FORMATION IN EVAPORATING DROPLETS OF LYSOZYME SOLUTIONS[35]

The influence of electrolytes on patterns produced during sessile droplet evaporation of colloidal suspensions has been found to produce interesting effects such as cracking, phase separation, and crystallization in the deposits.[62,91,95,96] These effects have also been observed during evaporation of biofluids.[11,12,79-81] To examine the influence of electrolytes on pattern formation in the lysozyme droplet system, NaCl was added to the lysozyme solution in varying concentrations. The solutions in this study contain lysozyme φ_L = 1.00 g/100mL and NaCl in concentrations φ_N = 0.01, 0.10, 0.50, and 1.00 g/100mL. These concentrations are generally consistent with the protein and electrolyte content in tears, given in Table 3.1. When affected by disease or other pathologies, the protein content in biofluids is known to vary.[79,82,84-86] Here, this affect is represented by changing the ratio of lysozyme to NaCl.

9.1 PATTERN FORMATION DURING EVAPORATION

Droplets containing lysozyme φ_L = 1.00 g/100mL and NaCl in concentrations φ_N = 0.01, 0.10, 0.50, and 1.00 g/100mL were observed *in situ* via optical microscopy and drop shape analysis (DSA) during the drying process. Upon deposition, all droplets were pinned to the substrate at the periphery and the initial contact diameter remained constant throughout evaporation. The

volume reduction of the solution due to the evaporation of the water led to a steady decrease in the contact angle of the droplet with the substrate. Concurrent with this reduction in contact angle, an outward radial flow produced a ring of condensed residue along the periphery of the drop. Until the formation of the perimeter ring, the drying process was similar for all of the solutions tested in this experiment. However, subsequent to the perimeter ring formation, the drying proceeded differently based on the NaCl concentration.

In pure lysozyme droplets, the contact angle decreased as the ring was formed until a critical angle was reached, θ_r. Then, the remaining liquid depinned and receded toward the center of the drop until evaporation was complete. In the final stages of evaporation, periodic surface cracks often appeared in the ring area associated with the release of internal stresses that accumulate during evaporation. In droplets of lysozyme solutions containing a small amount of NaCl (φ_N = 0.01 g/100mL), evaporation proceeded in a similar manner. The only difference noted was in the central region of the droplet, where a grainy structure was formed in the late stages of evaporation, whereas the rest of the deposit was smooth and featureless.

For solutions with more significant amounts of salt, the peripheral ring formed as for the other solutions, but the liquid never depinned. This drying process is illustrated in Figure 9.1 for a droplet containing φ_N = 0.50 g/100mL. The contact angle continued to decrease, creating an increase in the capillary flow rate. Aggregates were formed in the liquid and swept to the perimeter, creating a secondary ring area adjacent to the featureless peripheral ring (Fig. 9.1; b – d). Some of the larger aggregates (Fig. 9.1; a – f) remained relatively stationary, only experiencing a slight drift. As evaporation progressed, the deposit began to crack (Fig. 9.1e) and the aggregated particles moved in irregular paths, less obviously influenced by radial flow. Additional cracks began to form in the film and larger immobile aggregates assembled, forming

the dense, dark structures in Figure 9.1; f – l. The remaining liquid continued to evaporate through the film, causing more cracking and mechanical instabilities in the deposit. In the final drying stages, rapid dendritic crystal growth was observed from the center of the drop toward the ring (Fig. 9.1; h – l). This was accompanied by percolation of the remaining liquid through the solid deposit and extensive additional cracking in the perimeter ring (Fig. 9.1; k – l).

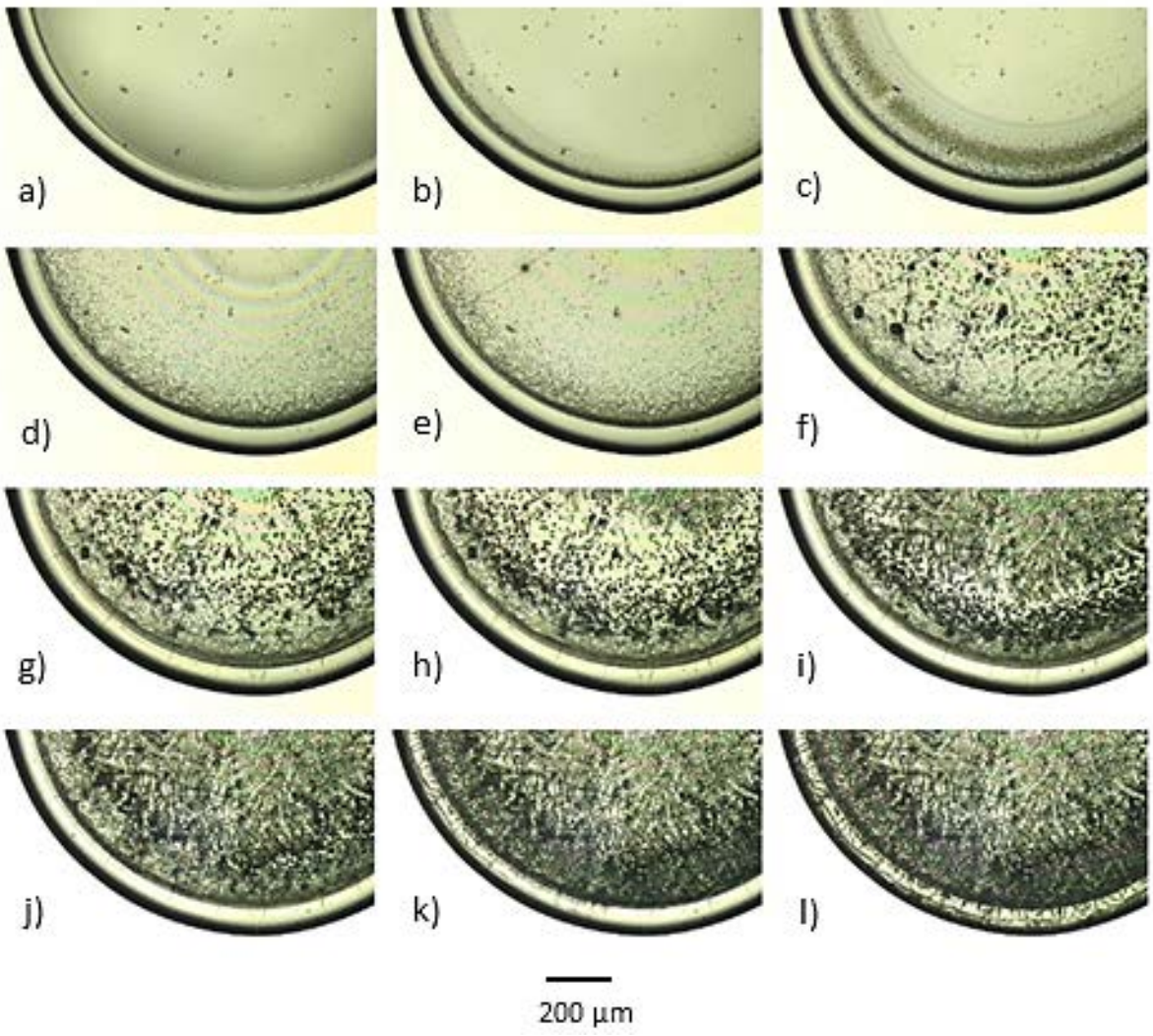

Figure 9.1. Sequential images of the evaporation process of a solution with φ_L = 1.0 g/100mL and φ_N = 0.50 g/100mL at a) t = 0, b) 40, c) 80, d) 120, e) 160, f) 200, g) 240, h) 250, i) 260, j) 270, k) 280, and l) 290 seconds.

The times in Figure 9.1 provide a reference timescale for the images. Note that these times do not reflect the total elapsed time from the initial droplet deposition. The total drying time for the droplets in this study ranged from 10 to 20 minutes. Due to this rather lengthy drying process, videos were captured only during the final stages of drying as shown in this panel of images. The end of the drying process was determined visually as the point in time after which no changes occurred in the morphology of the deposited structure.

The evaporation process for drops containing only NaCl (φ_N = 1.0 g/100mL) was also observed for comparison. In this case, the drop slowly receded and never pinned along the contact line. Large NaCl crystals were formed in the center of the droplet during evaporation. The resulting pattern consisted of several NaCl crystals collected in the central region (Fig. 9.2f). The overall morphologies of the deposits from the pure NaCl solution were unlike those observed in the lysozyme + NaCl deposits.

9.2 EFFECT OF SALT CONCENTRATION ON PATTERN FORMATION

Examples of the final deposit patterns for the solutions examined in this study are given in Figure 9.2. Deposits from pure lysozyme (Fig. 9.2a) and pure NaCl (Fig. 9.2f) solutions are also included in Figure 9.2 for comparison. In pure lysozyme solutions (Fig. 9.2a), the dried morphology was consistent with previous observations (Chapter 6). As the salt concentration increased, this structure gradually changed. With a small amount of salt (Fig. 9.2b), the overall structure was similar to the pure lysozyme deposit with a single perimeter ring and multicolored fringes. This deposit also includes a region with a grainy texture which is obviously distinct from the rest of the deposit.

With increasing salt content, a clear secondary ring-like region began to form, separating the peripheral ring from the central region of the deposit. For ease of discussion, these three regions are referred to as “Region I”, “Region II”, and “Region III,” and are illustrated schematically in Figure 9.3.

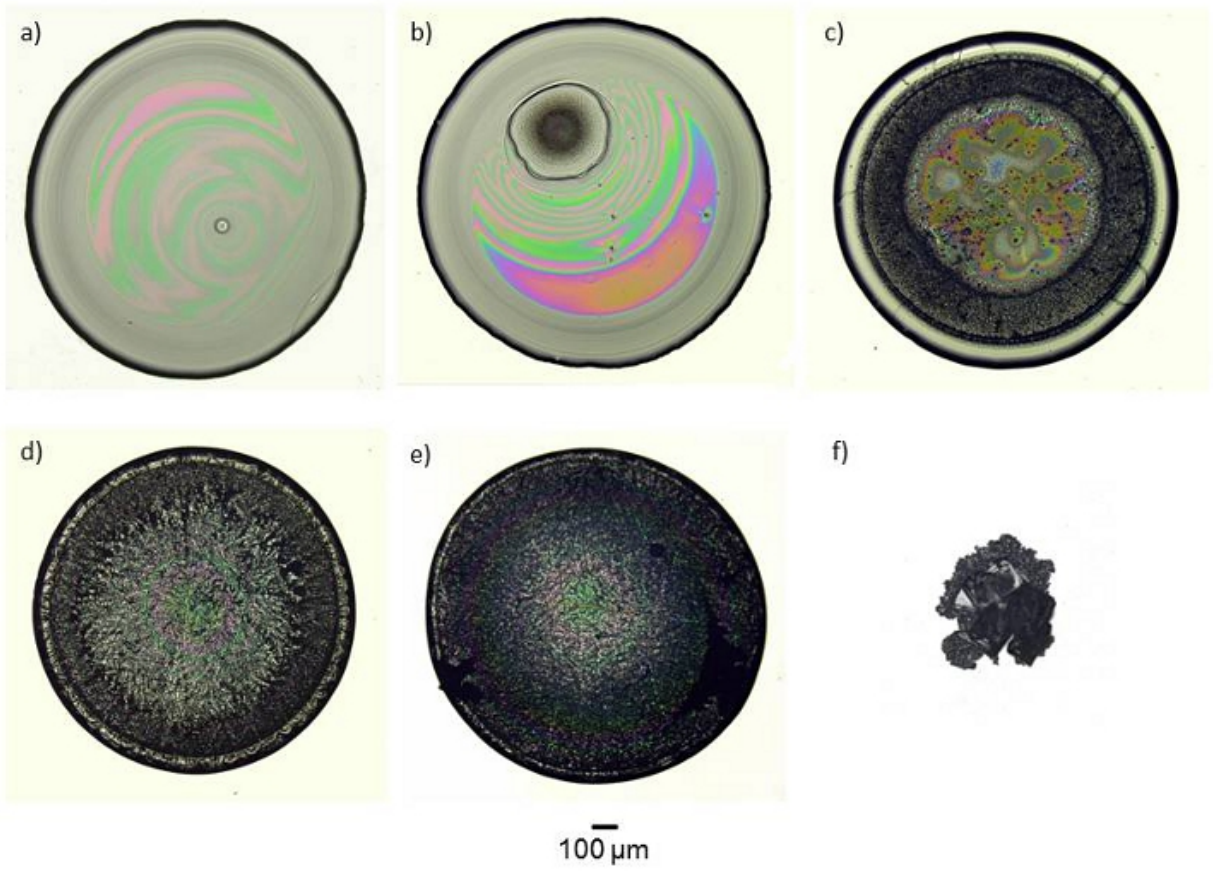

Figure 9.2. Dried droplets from lysozyme solutions with increasing φ_N; a) 0.00, b) 0.01, c) 0.10, d) 0.50, and e) 1.00 g/100mL NaCl. The pattern in f) contains only NaCl.

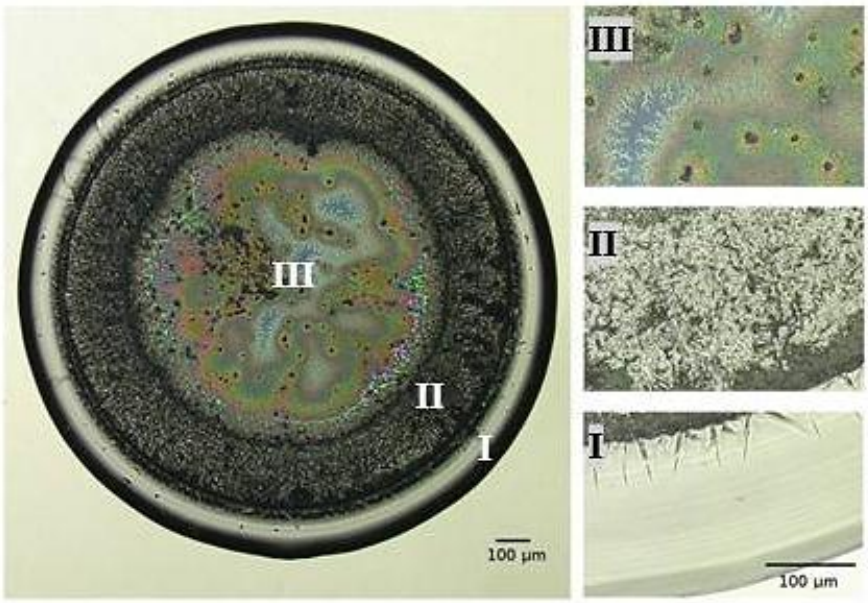

Figure 9.3. Deposit from solution with φ_L = 1.0 g/100mL and φ_N = 0.10 g/100mL, illustrating three deposit regions.

Region I is the perimeter "coffee ring" which is characteristic of pinned colloidal droplets and apparent in all of the deposits. Surface cracks are observed in the ring area, sometimes periodic, with the number of cracks increasing with initial salt concentration. The peripheral ring is similar to those found in pure lysozyme deposit studies and is attributed to a lysozyme gel or glassy structure.

Region II refers to the secondary ring area of the deposit and is illustrated in more detail in Figure 9.4. At very low salt concentrations (Fig. 9.4a), Region II is not distinct but its onset may be indicated by the brightly colored fringes in the area between the perimeter ring and the central region. As the salt content increases (Fig 9.4; b - d), this region becomes well-defined with a high density of aggregates and dendritic structures which cover more area with increasing NaCl concentration.

Dendritic crystal structures are also observed in Region III and illustrated in Figure 9.5b – d. In the deposit containing 0.01 g/100mL NaCl, this region is distinct from the rest of the deposit and has a grainy texture. In the deposits containing 0.10 g/100mL NaCl, Region III is larger and also has a grainy texture. However, there are also areas containing dendritic branches as well as larger aggregates (Fig. 9.5b). More dendrites are apparent in Region III of the deposit containing 0.50 g/100mL NaCl (Fig. 9.5c). There are also large, darker (more dense) aggregates in this region as well. The dendrites grow mainly from the center of the drop toward the ring. This is also the case in the deposit with the highest concentration of NaCl (Fig. 9.5d). For this concentration, Region III contains similar dendrites but more dark aggregates than those with lower salt content. These darker aggregates are often found at the tip of the dendrite. The diameters of the dendrite primary branches are on the order of ~ 2 μm and display second and third order branching, independent of salt concentration.

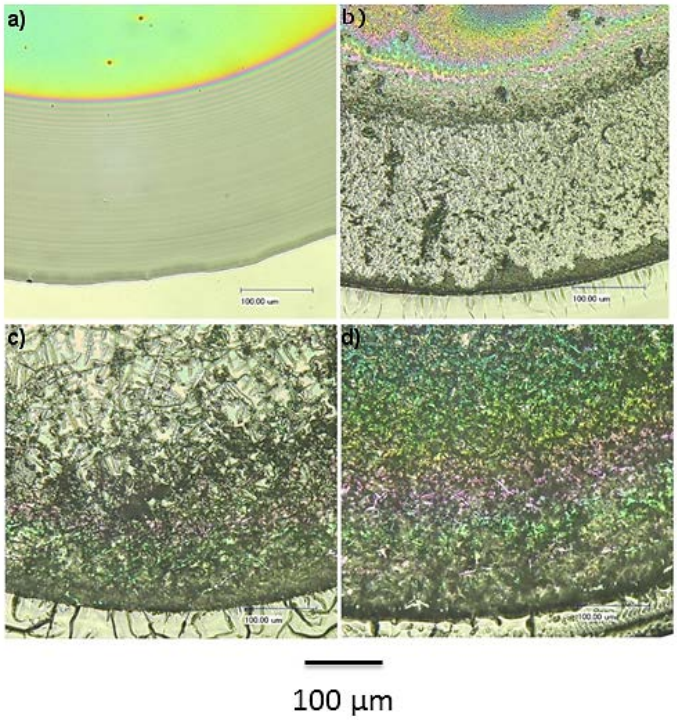

Figure 9.4. Images of Region II for φ_N = a) 0.01, b) 0.10, c) 0.50, d) 1.00 g/100mL.

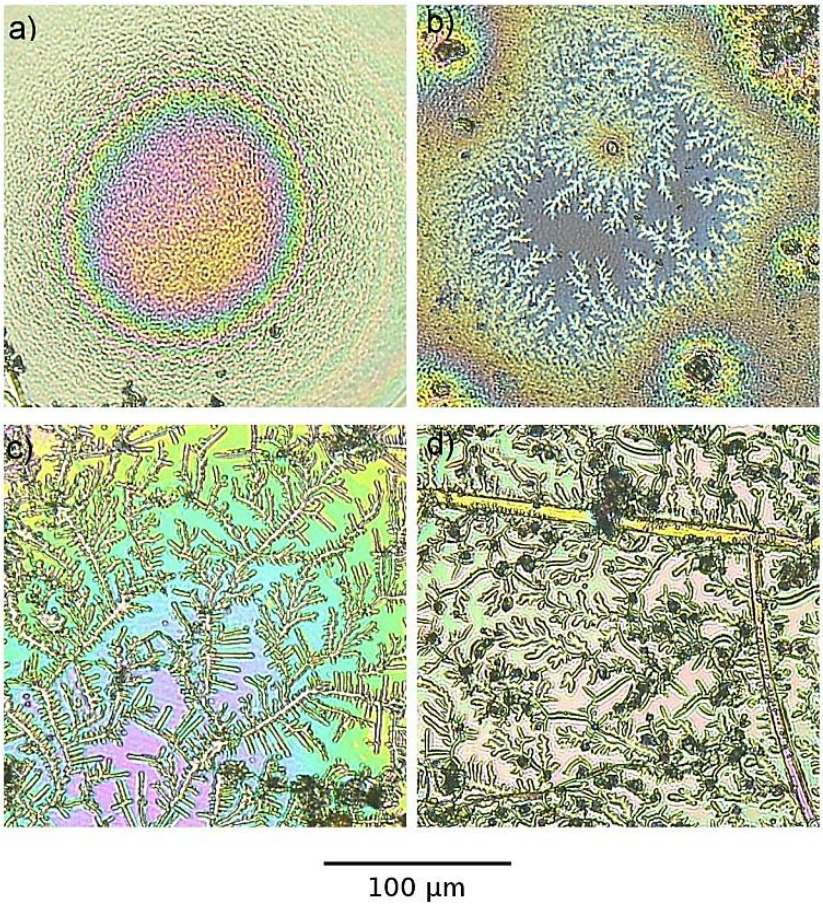

Figure 9.5. Images of Region III for φ_N = a) 0.01, b) 0.10, c) 0.50, and d) 1.00 g/100mL.

One clear trend in these observations is a decrease in the width of Region I as the salt concentration increases, which is consistent with the formation of Region II. The relative width of the ring, *w*, was measured for each of the drops and analyzed as a function of relative salt concentration, Φ_N. The width of the ring is normalized by the drop diameter, *w/D,* and the relative salt concentration, Φ_N, is the molar amount of salt divided by the molar amount of lysozyme. This value is effectively the number of salt ions per lysozyme molecule. A plot of –ln *w/D* vs ln Φ_N and best fit line are given in Figure 9.6. The best fit to the curve is a power law relationship with an exponent of -0.48 and an R^2 value of 0.98.

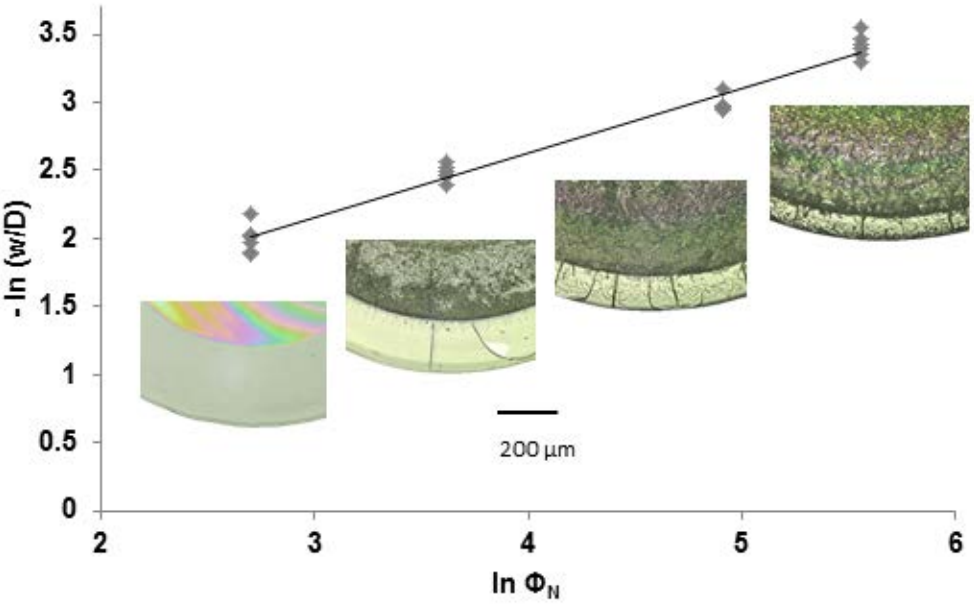

Figure 9.6. Plot of –ln (*w/D*) (relative width of Region I (ring)), vs. ln Φ_N, the relative salt concentration.

The number of cracks in the ring also increases with initial salt concentration, as illustrated in the images in Figure 9.6. Cracking in the ring is attributed to competition between adhesion to the substrate and shrinkage of the solid deposit during to evaporation.[61,139] Internal stresses build up during evaporation and radial cracks emerge from the contact line. When the ionic strength of the solution increases, more cracks are apparent. The number and direction of the cracks depend on the evolution of the drop shape. During evaporation, the shape evolution of the drop changes with higher initial salt content, affecting the internal stresses which, in turn, influences ring cracking.

9.3 SEM STUDY

A scanning electron microscope (Philips, XL-30) was used to observe the structure of the deposits at a finer scale. Several key observations can be made based on the higher resolution images obtained with the SEM. The surfaces of the deposits are remarkably smooth in Region I and show evidence of a more porous structure in Regions II and III. The SEM also revealed multi-scale hierarchical structures in Regions II and III in all of the deposits containing NaCl. To illustrate this structure, Figure 9.7 shows a portion of Region III in a lysozyme deposit containing 0.01 g/100mL NaCl. This corresponds to the grainy region in Figure 9.2b.

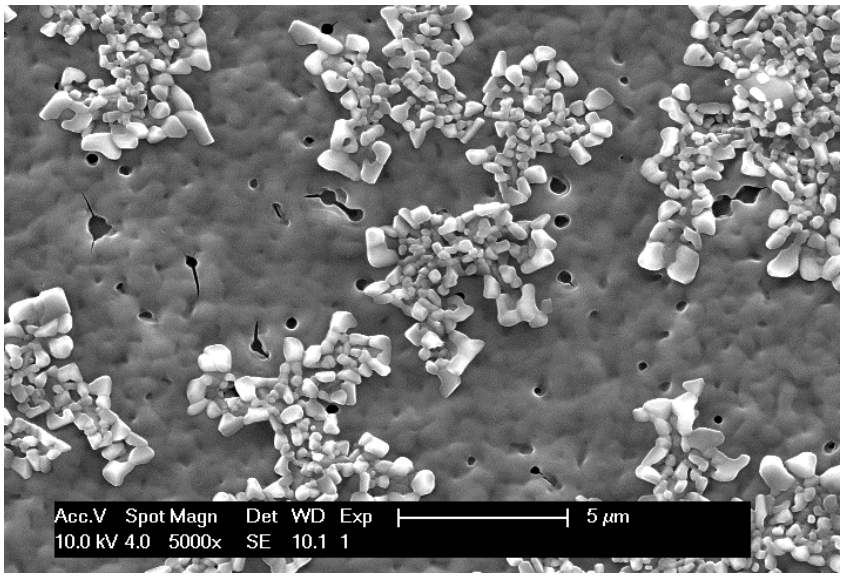

Figure 9.7. SEM image from Region III of a deposit with φ_L =1.00 and φ_N = 0.01 g/100mL.

This region of the deposit exhibits scattered small pores and branched, aggregated structures on top of this porous surface. In the optical images of the deposit containing 0.01 g/100mL NaCl (Fig. 9.5a), there is little indication of crystalline structure in the central region. However, the SEM images illustrate that there is structure in this region, even for the lowest solution

concentration of NaCl. Similar structures were observed in Regions II and III of deposits containing higher concentrations of NaCl. As the salt concentration increased, these structures covered more of the surface area of the deposit, and were similar in nature. It should be noted that the structures in Figure 9.7 are similar to aggregates of plate-like tetragonal crystals that have been observed in lysozyme crystallization studies.[101,113]

Energy Dispersive X-ray Spectroscopy (EDXS) spot analysis was used on homogeneous gel-like locations in Regions I, II, and III as well as on selected aggregates, dendrites, and crystallites in Regions II and III. In the pure lysozyme sample, C, N, O, and S (associated with lysozyme protein) were present throughout the sample in all three regions. Small amounts of Na and Cl were also found (the commercial lysozyme powder contains small amounts of inorganic salts for buffering purposes). The homogeneous peripheral ring contained Cl but negligible Na. However, the Na:Cl ratio increased in Regions II and III. This was attributed to the sampling depth of the EDXS technique and the association of negatively charged Cl ions with the lysozyme molecule and the positively charged Na ions with the negatively charged SiO_2 substrate. The accumulation of Na near the substrate is not detected in Region I which has a thickness on the order of tens of microns.

In deposits with added NaCl and three distinct regions, the amounts of Na and Cl increased in Regions II and III while the elemental makeup in Region I was similar to that of pure lysozyme. In addition, more Na and Cl were detected in the flat, porous part of Region III compared to that of Region II. This is further illustrated in Table 9.1, which includes the mean Na:Cl ratios for each of the three regions (and associated standard deviation in the data). The dendritic structures in Regions II and III contained significant amounts of Na and Cl, but also contained C, N, O, and S. The cubic crystals were composed predominantly of Na and Cl in

ratios close to 1. This analysis provides a general picture of the composition of the various regions and structures in the deposit, but there are limitations associated with sampling volume of the technique. As noted above, the thickness of Region I blocks detection of chemical information from near the substrate. More generally, the EDXS signal apparently taken from individual aggregates, dendrites, and cubic crystallites cannot be isolated from the signal coming from the surrounding gel in which these structures are embedded.

Table 9.1. Na:Cl ratio in three deposit regions

Region	Na:Cl
I	0.147 ± 0.05
II	0.740 ± 0.11
III	1.07 ± 0.12

9.4 EFFECT OF DROPLET SIZE ON PATTERN FORMATION

Smaller droplets containing lysozyme and NaCl were deposited with the Preval® aerosol spray system, providing drops with $D \sim 20 - 250$ μm. Representative optical microscopy images of these deposits are shown in Figure 9.8 with φ_L =1.0 g/100mL and φ_N = 0.01, 0.10, 0.50, and 1.0 g/100mL.

The overall shapes of the deposits in this size range are similar to the larger, mm-scale deposits. The μm-scale deposits exhibit the familiar ring-like structure in Region I and overall transparency of the deposit, with colored fringes indicating the variation in thickness. Unlike the mm-scale deposits, Regions II and III are not as distinctive in the smaller deposits. These deposits appear mostly smooth and translucent, similar to pure lysozyme deposits, with various crystallites and dendrites in the central region of the deposit at higher NaCl concentrations.

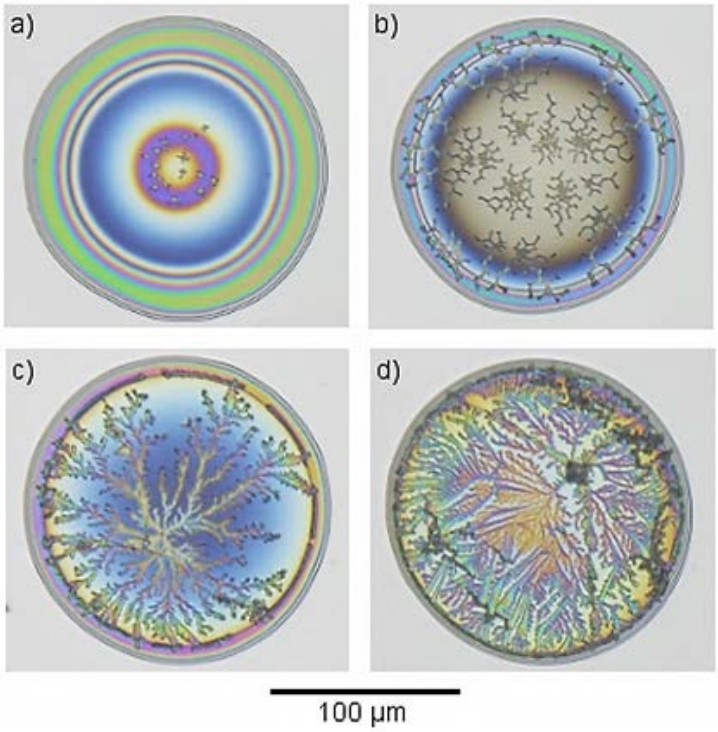

Figure 9.8. Micro- scale drop deposits containing φ_L =1.0 g/100mL and φ_N = a) 0.01, b) 0.10, c) 0.5, d) 1.0 g/100mL.

The deposits with the lowest NaCl concentration (Fig 9.8a) are quite similar to pure lysozyme deposits, with the exception of small crystallites in the center of the deposit. Figure 9.8b shows the deposit containing 0.10 g/100mL NaCl, which has a honeycomb-like structure throughout the deposit. The peripheral rings for these two deposits are similar to that of pure lysozyme, but with the various structures also apparent in this concentration (Fig. 9.8b). In the φ_N = 0.50 and 1.00 g/100mL concentration deposits (Fig 9.8; c-d), dendritic structures are found in the central region. In both of these deposits, the dendrites appear to grow from a single crystal seed toward the periphery. While these types of structures are apparent in the mm-scale deposits, the larger drops contain multiple primary dendrites grown from multiple crystalline seeds.

For the smaller scale deposits (D < 50 μm), AFM can be employed in closer examination of these interesting structures. Examples of typical morphologies in this size regime are given in the two and three-dimensional AFM topographic images and cross sectional profiles of Figure 9.9 for φ_N = 0.10 and 1.00 g/100mL.

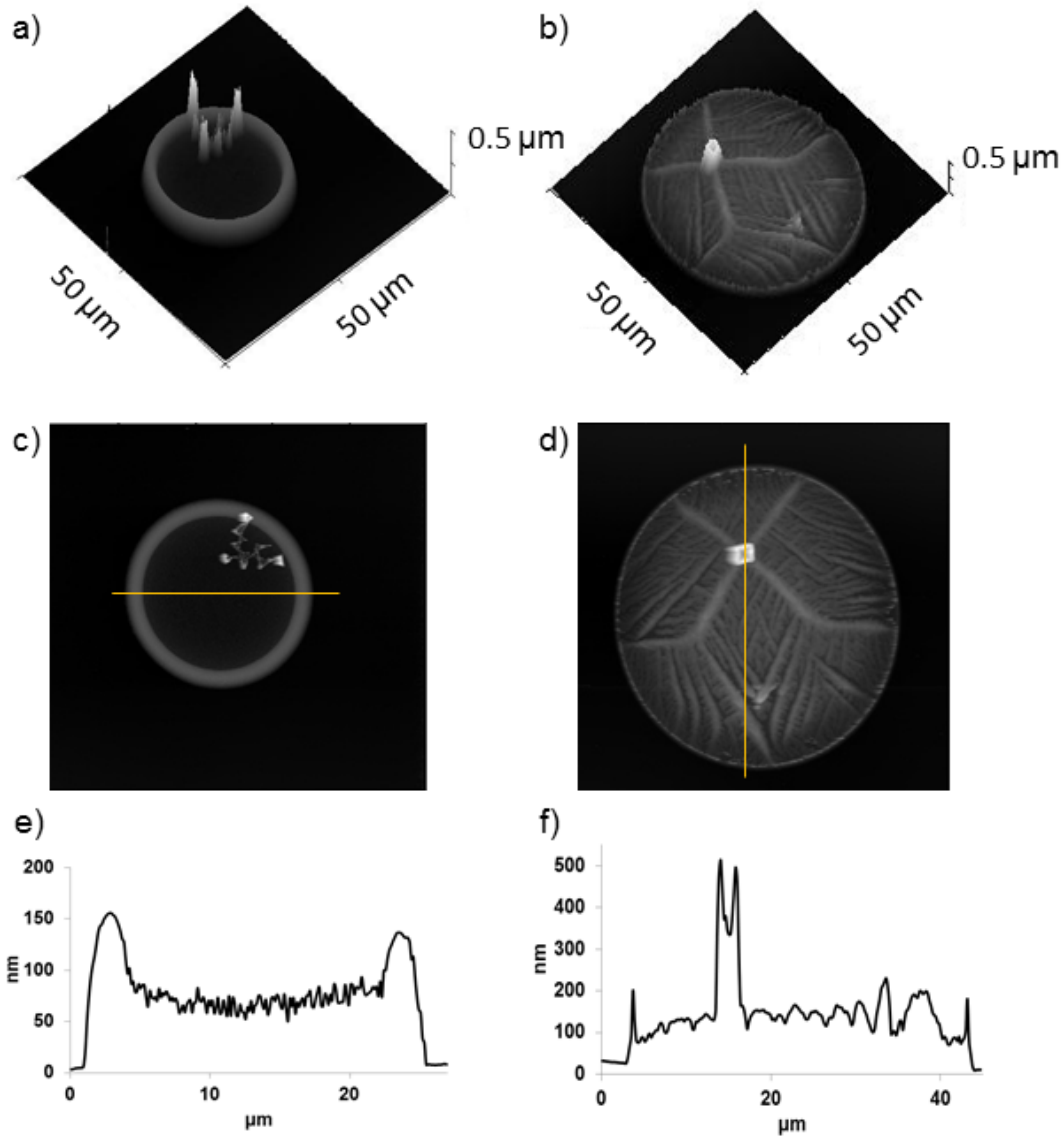

Figure 9.9. Morphologies for deposits with φ_L = 1.0 and φ_N = a) 0.10 and b) 1.0 g/100mL.

The left column in Figure 9.9 shows a deposit with φ_N = 0.10 g/100mL. Based on the AFM topographic images, this deposit is similar in shape to the pure lysozyme deposits, with a peripheral ring much thicker than the central region of the deposit (Fig 9.9e). A small honeycomb-like structure is present near the periphery, similar in appearance to the structure in Figure 9.8b. This structure is clearly much thicker than the remainder of the deposit. The cross sectional profile in Figure 9.9e shows the peripheral ring with a peak of ~ 150 nm and the central region ranging from 50 - 100 nm. This central region is much less smooth than the profiles observed in pure lysozyme deposits (Chapters 6 – 8). The AFM measurements of deposits containing φ_N = 0.01 and 0.10 g/100mL revealed a number of pores and generally rough surfaces.

The column to the left of Figure 9.9 shows a deposit with φ_N = 1.00 g/100mL. This deposit has an obvious peripheral ring as well as dendritic structures in the central region. The dendrites have a single, faceted, crystalline seed with primary dendrite branching toward the periphery. Second and third order branches are also clear from the AFM topographic images. The main branches have a diameter of ~ 2 μm and the secondary branches have diameters of ~ 1 μm. The diameters of the main branches are consistent with those observed in the larger mm-scale deposits. These are also consistent with the dendrites observed in deposits with φ_N = 0.50 g/100mL. The number of dendrites increase with NaCl concentration, but the diameter is consistent in both concentrations and size regimes. The cross sectional profile in Figure 9.9f illustrates the thickness of these dendritic structures. The profile was chosen along the line illustrated in Figure 9.9d to include the large faceted crystal. The ring is apparent, but much less smooth than the deposits with lower NaCl concentrations. The crystalline seed is much thicker with peaks over twice as high as the remainder of the deposit.

9.5 DISCUSSION

It is clear from these experimental observations that distinctive regions are formed in the deposits from lysozyme – NaCl solutions and various structures are found which depend on the NaCl content. Segregated regions have been known to form during evaporation of single[140] and multi-component[32] colloidal droplets. An order-to-disorder transition was recently observed in the ring region from droplets of colloidal polystyrene.[140] The outer portion of the ring was ordered in a hexagonal packed structure while the adjacent portion of the ring (closer to the center of the drop) was disordered. This was explained by a change in the capillary flow rate during evaporation. When the particles reach the periphery at the earliest stages, they have time to arrange into an ordered phase via Brownian motion. The particles that reach the periphery at higher velocities form a jammed, disordered phase.[140] This, in addition to variations in particle interactions and mobility in suspension, results in segregation of multicomponent solutions. Distinctive regions are also observed in evaporated droplets of human biofluids including blood serum,[9,10] synovial fluid,[141] and tears.[13,79] These regions generally include an amorphous ring and a central region containing crystallites.

To rationalize the experimental observations in this study, the forces acting on a lysozyme molecule during evaporation are considered. Forces due to capillary flow, F_C, Marangoni flow, F_M, which resists capillary flow, the force between the protein and substrate, F_S, and the interaction between the lysozyme molecules, F_L, may play a role. When the drop is deposited, the positively charged lysozyme molecules adsorb to the negatively charged SiO_2 substrate, due to the particle-substrate interaction, F_S. The adsorbed molecules cause pinning of the droplet. Simultaneously, lysozyme molecules are transported to the periphery by capillary flow, which forms the ring. The significant increase in lysozyme concentration and rapid

evaporation of water at the periphery results in the phase transition at the peripheral ring. This phase transition leads to a transparent lysozyme-rich amorphous ring, which was observed in all of the deposits studied. The central regions of the deposits contain colored fringes in addition to the various structures. The colored fringes indicate that the gel or glassy-like structure is present in the entire drop area. After formation of the adsorbed layers and the amorphous ring, the phase transition continues toward the central region of the drop and from the substrate toward the drop apex, producing a porous gel-like structure throughout the deposit.

The chemistry of the liquid in the drying droplet evolves during evaporation as lysozyme molecules leave solution and adsorb to the substrate and form the peripheral ring. Consequently, the ionic strength of the remaining solution increases, which changes the lysozyme-lysozyme interaction, F_L. Protein-protein interactions in aqueous systems are often modeled by the classical DLVO (Derjaguin, Landau, Verwey, and Overbeek) potential which considers the interaction between charged surfaces through a liquid medium, combining short range Van der Waals attraction and longer range electrostatic repulsion. The attractive force between the molecules increases with decreasing Debye length. In other words, the range of interaction between molecules decreases in the remaining liquid, which drives liquid–liquid phase separation of the solution.[101] Clusters and fractal aggregates of lysozyme have been known to form in such cases.[142] In this experiment, aggregates are formed as the droplet evaporates. Some larger aggregates are influenced by the capillary flow, F_C, and are swept to the periphery, forming Region II in the mm-scale droplets. With an increase in initial NaCl concentration, aggregates are formed at earlier stages of evaporation and transported to the periphery. This results in a decrease in the width of Region I and corresponding increase in width of Region II with increasing NaCl concentration. In the smaller, micro-scale deposits, there are only two

distinct regions, the peripheral ring in Region I and the central region, which contains crystallites and dendritic structures with higher NaCl concentrations. Employing the above reasoning for the region formation, we propose that in smaller drops, the shorter evaporation times prevent the larger aggregates from forming at earlier stages of evaporation and thus there is no intermediate region between the periphery and central region.

The relationship between the ring width and NaCl concentration fits a power-law dependence with an exponent of -0.48, given in Figure 9.6. Power law relationships between w and φ have been previously observed in colloidal droplet evaporation studies.[16-18] This relationship can be deduced with a simple geometric argument. In a single-component system, if the volume of the ring is proportional to the initial concentration of solute, $V_R \propto \varphi$, a higher initial concentration should lead to a larger ring volume. The ring width scales approximately as the square root of the ring volume, $w \propto (V_R)^{1/2}$. Since the ring volume is proportional to the concentration, the ring width should also scale as the square root of the initial concentration, $w \propto \varphi^{1/2}$. In this study, we consider a multi-component system, but the above reasoning is consistent with the results presented in Figure 9.6. We consider the initial concentration of NaCl, which leads to a negative square root dependence, or, $w \propto -(\varphi^{1/2})$. The formation of aggregates at earlier times with increasing NaCl inhibits formation of the lysozyme-rich ring, resulting in this negative square root dependence. It should be noted that this power law dependence was not observed in the deposits containing only lysozyme (Chapters 6 – 8). In the pure lysozyme systems, the geometry of the deposit varied little with concentration and was dependent only on the initial spherical cap geometry and the angle at which depinning occurs, or the receding angle, θ_r.[33,34]

In recent studies on the influence of salts in evaporating colloidal droplets, the central region was believed to be composed of mostly salt crystals.[62,95,96] In this experiment however, we propose that many of the structures observed in Regions II and III are lysozyme aggregates and crystals, dependent on initial NaCl solution concentration. While the drop evaporates and lysozyme adsorbs to the substrate and collects in the ring, the ionic strength of the liquid increases driving liquid-liquid phase separation and formation of hierarchical protein structures. In solutions with higher salt content, the proteins in the central region are less soluble, resulting in a "salting-out" effect and formation of protein and salt crystals in the deposit.[111]

The various structures observed in the optical and SEM images are similar to the tetragonal lysozyme crystals reported in the literature.[97,98,101,112-114] Lysozyme crystals can be grown in sodium chloride solutions, resulting in the common tetragonal structure or variations of this structure (orthorhombic) at different temperatures and levels of supersaturation.[97,98,101,112-114] The aspect ratio of tetragonal lysozyme crystals is known to change with supersaturation, from elongated crystals at low supersaturation to plate-like crystals at high supersaturation. If the supersaturation is yet higher, precipitation occurs instead of crystallization.[112] The effect of pH on lysozyme crystallization has also been studied. Single tetragonal crystals are formed at low pH and "needle like" crystals develop as the pH increases.[98,101,113,114] It should also be noted that longer times are required for proper alignment of the molecules to ordered structures.[98,99] Therefore, it is expected that random aggregation will be energetically favored for much of the far-from-equilibrium evaporation process.

Though a variety of morphologies for lysozyme aggregates and crystals have been observed in the literature, dendritic lysozyme structures have not yet been reported to the authors' knowledge. However, dendritic structures have been observed in crystallization of

aqueous solutions of bovine serum albumin (BSA) and NaCl.[143,144] These studies examined the anion and cation effects on crystallization of BSA, a globular protein, and found primarily linear structures with branching in BSA-NaCl crystals. Interestingly, the mechanism of branching was shown to depend on single facial capping by NaCl crystallites. Dendritic growth in the lysozyme system may be occurring in a similar fashion. The dark aggregates on the tip of some dendritic lysozyme branches may be NaCl crystals capping the branch. The results of our EDXS analysis support this theory as well as the formation of the various regions in these lysozyme solution droplets containing electrolytes.

The micro- scale deposits in this study also contain these dendritic structures, similar in appearance and diameter to those observed in the larger mm- scale deposits. Therefore, we assume that the pattern formation process is similar in these two size regimes. As the deposit diameter decreases, the structures are apparent, but fewer structures are found in each deposit. This indicates that formation of these dendrites and crystallites occur in a similar fashion, but perhaps do not have as much time to align in the micro-scale deposits, as the evaporation time is much shorter. Based on the AFM topographical images, the entire deposits from solutions containing salt are not as smooth and indicate aggregate formation throughout the central region of the deposit, consistent with our observations for mm- scale deposits. The micro- scale deposits containing various concentrations of NaCl are examined further in Chapter 10 by image analysis and pattern recognition of the deposit images to compare the patterns in a quantitative manner.

10.0 PATTERN RECOGNITION FOR IDENTIFICATION OF LYSOZYME DROPLET SOLUTION CHEMISTRY

In this study, a novel pattern recognition program is presented to differentiate between deposit patterns from lysozyme solution droplets with varying concentrations of NaCl. The solution concentrations considered contain lysozyme (φ_L = 1.00 g/100mL) with no salt and with NaCl in concentrations of φ_N = 0.10, 0.50, and 1.00 g/100mL. Droplets were deposited onto clean Si wafers using a drop-on-demand printing device (MicroFab Technologies, Inc., JetLab4®). The droplets were printed in micro-arrays with spacing of ~100 μm and had deposit diameters of ~100 μm.

10.1 IMAGE ACQUISITION AND PREPROCESSING

Deposits were observed after evaporation with the Keyence digital optical microscope. The colors were adjusted by setting the white balance and the images were collected in the "image enhancement" mode. The entire deposit array was captured as a single image and then individual drops were cropped from the original image. *ImageJ*, an open source image processing program, was used to crop and rescale the images. Deposit images were cropped from the array image in a region slightly larger than the deposit to minimize the background.

The deposit images were then rescaled to 150 x 150 pixels. Deposits with large defects or highly irregular shapes were not used in the experiment. Representative deposit images for the concentrations considered in this study are collected in Figure 10.1.

Further image processing was performed using the Insight Segmentation and Registration Toolkit (ITK).[145] ITK is an open source software toolkit which is implemented in C++. The cropped and scaled deposit images were converted to grayscale using a grayscale filter which scales the pixel values from 0 to 255. A program was developed to perform the grayscale conversion, feature extraction, select training and test images at random, and classify the images. This program was also developed in C++ and is further described in the following sections. The source code for the program is given in Appendix A.

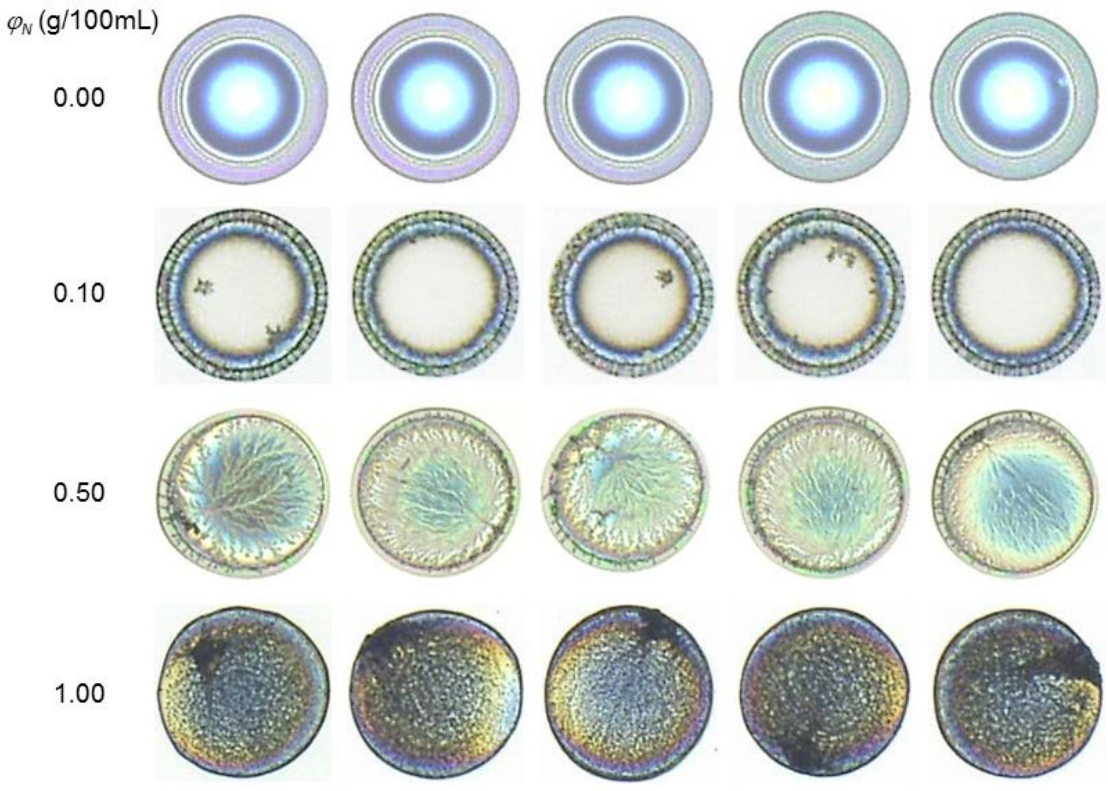

Figure 10.1. Representative deposits from printed droplets containing φ_N = 0.00, 0.10, 0.50, and 1.00 g/100mL.

10.2 FEATURE EXTRACTION

In order to classify the images, specific image information must be extracted and used as the vector for classification. This process is referred to as "feature extraction." Wavelet transforms have become a popular way to represent images and are used in a number of pattern recognition applications. This is due to the robust and informative nature of the wavelet. The wavelet represents the time-frequency localization of a signal and most of the energy of the signal can be represented by a few expansion coefficients. This method involves the decomposition of a raw signal onto a set of basis functions (here, the image) by dilation, contraction, scaling, and/or shifting of the signal. This includes applying successive filters which decompose the data into sets of coefficients which contain information about the signal at various scales. Daugman originally developed this method of using convolution with bandpass filters for extracting textural information from iris images using a 2D Gabor wavelet function.[118] The mother wavelet $\Psi(x, y)$ is parameterized as:

$$\Psi_{m\theta}(x, y) = 2^{-2m}\Psi(x', y') \,. \tag{10.1}$$

The variables (x', y') contain dilations of the size of the wavelet by 2^m and translations in angle by θ:

$$\begin{aligned} x' &= 2^{-m}[xcos(\theta) + ysin(\theta)] \\ y' &= 2^{-m}[-xsin(\theta) + ycos(\theta)] \end{aligned} \tag{10.2}$$

Daugman chose the Gabor wavelet as it is an excellent model of the receptive field profiles of individual neurons in the visual cortex.[146-148] The response, $v(x, y)$, of a neuron to an arbitrary image is the product of a "receptive field function," $g(x, y)$, and the image luminance distribution, $I(x, y)$. This response can be treated as a 2D spatial filter[146]

$$v(x,y) = \iint_{\Omega} I(x,y)g(x,y)dxdy, \qquad 10.3$$

where Ω is the set of all image points and $(x,y) \in \Omega$. Daugman modeled the "receptive field function" with the complex two dimensional Gabor function as $g(x,y)$.[149] This 2D Gabor function (parameterized as in References [147,148]) is given by:

$$g_{\Gamma,\sigma,\lambda,\vartheta,m,\theta}(x,y) = e^{-(\frac{x'^2+\Gamma^2 y'^2}{2\sigma^2})}\cos(2\pi\frac{x'}{\lambda}+\vartheta) \qquad 10.4$$

The Gabor function in Equation 10.4 is determined for specified values of the parameters, $\Gamma, \sigma, \lambda, \vartheta, m, \theta$. The eccentricity of the receptive field ellipse, or the spatial aspect ratio, is described by Γ. When $\Gamma = 1$, the receptive field is a circle. In this study, it is taken as $\Gamma = 0.5$. The size of the receptive field is given by σ, which is the standard deviation of the Gaussian factor, $\sigma = 0.56\lambda$, where λ is the wavelength or spatial frequency, $1/\lambda$, of the harmonic factor $\cos(2\pi\, x'/\lambda + \vartheta)$. The phase offset in the harmonic factor is described by ϑ. When $\vartheta = 0$ and $\vartheta = \pi$, the function $g(x,y)$ is symmetric, or even, and when $\vartheta = \pm\,(1/2)\pi$, the function $g(x,y)$ is antisymmetric, or odd. The variables m and θ appear in (x', y'), as given in Equation 10.2. The dilation of the wavelet is described by 2^m and m is the number of "scales." The angle, θ, describes the orientation to the normal (x' axis) with $\theta = k(\pi/8)$, where k is the number of orientations. The values used for the calculations in this experiment are collected in Table 10.1.

Table 10.1. Parameters used in the Gabor function calculation.

Parameter	Value
Γ	0.5
σ	0.56λ
λ	2
ϑ	0, ±0.5π
m	6, 8, 10, 12
k	8

The Gabor function is determined numerically with the parameters given in Table 10.1. Then, the inner product of $g(x,y)$ and the image $I(x,y)$ is taken. The response $\nu(x,y)$ is a collection of coefficients which is a vector of size ($m*k$ x 1). These Gabor coefficients are complex-valued. For computational simplicity, the magnitude of the complex number, $\nu(x,y)$, is determined by $|\nu| = \sqrt{\nu_{Re}^2 + \nu_{Im}^2}$. This array of $|\nu|$ values is used as the measurement vector of the image for classification and is a vector of size ($m*k$ x 1).

10.3 PATTERN RECOGNITION

The measurement vector described above is used to represent each image for classification. There are a number of ways to design a classifier and several are outlined in Section 3.6.2. In general, the classifier takes an unknown image, represented by the measurement vector, and assigns the unknown to the class it most likely belongs, based on a decision rule. In this experiment, a linear decision rule is used, which is based on the Euclidean distance between measurement vectors, $d = \sqrt{(x_1 - y_1)^2 + (x_2 - y_2)^2}$. In machine learning, classification is often associated with supervised learning, which depends on the availability of a training set. The training set is represented statistically for each class and the new instance is compared and classified accordingly. In unsupervised learning, the data is not identified by class *a priori*. In an unsupervised learning or clustering algorithm, the measurement vectors are grouped into classes by some measure of similarity (distance, connectivity, etc).[121] In this study, both supervised and unsupervised methods were used to examine the accuracy of both of these methods in recognition of the patterns from evaporated colloidal droplets.

The k-means algorithm was used in both the supervised and unsupervised methods in this experiment. In k-means classification, the training sets are assigned to their classes and the means of the measurement vectors for each class are determined. In general, the k-means algorithm in this study consisted of four steps:[121]

1. Assign samples to clusters or choose cluster centers and assign all samples to the nearest cluster.
2. Determine the mean of each cluster.
3. Compare new samples to the cluster means and assign to the nearest cluster.
4. Reassign each sample to belong to the nearest cluster mean.

In the unsupervised learning test, the cluster means (four clusters, representing each class) are initialized to zero and the k-means clustering algorithm is applied. The measurement vectors for all test images are compared and the four clusters are formed based on Euclidean distance to one another. The number of classes is specified *a priori*. In the supervised learning test, the method of classification is similar, but the initial means are determined from the measurement vectors of training images for each class. Then the measurement vectors of the test images are compared to the mean by Euclidean distance and classified by assigning each measurement vector to the closest cluster mean.

10.4 RESULTS

For each solution concentration, the deposits were reproducible and unique. Distinctive structures were observed, which depend on the NaCl solution concentration, consistent with our previous observations (Chapter 9). A representative deposit from each concentration is illustrated in more detail in Figure 10.2.

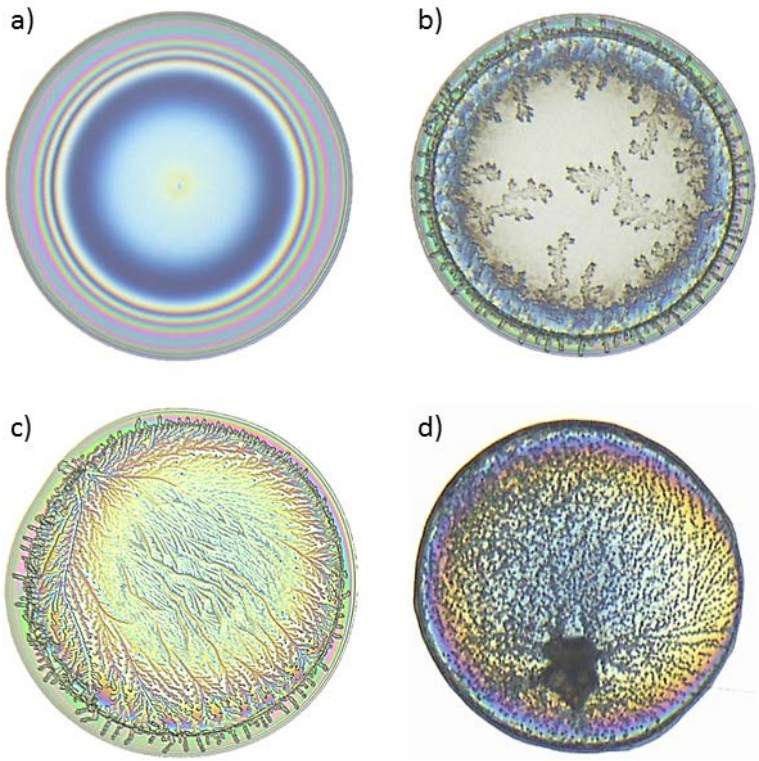

Figure 10.2. Deposits from solutions containing φ_L = 1.00 g/100mL and φ_N = a) 0.00, b) 0.10, c) 0.50, and d) 1.00 g/100mL.

All deposits covered the entire wetted area, with no obvious spreading or receding. The morphologies of all deposits observed were consistent with our previous observations, discussed in Chapter 9 and References [33-35]. At least 30 images from each concentration were cropped from the array images, scaled to 150 x 150 pixels, and converted to grayscale. The Gabor wavelet function was applied to each image, resulting in individual measurement vectors containing the Gabor coefficients, $|\nu|$. The Gabor wavelet was used with scales of m = 6, 8, 10, and 12, and with k = 8 orientations. This collection of coefficients was taken as the measurement vector, with a size of (m*k x 1) coefficients. Examples of the wavelet coefficients from representative images of pure lysozyme and lysozyme with 1.00 g/100mL of NaCl are collected in stem plots in Figure 10.3.

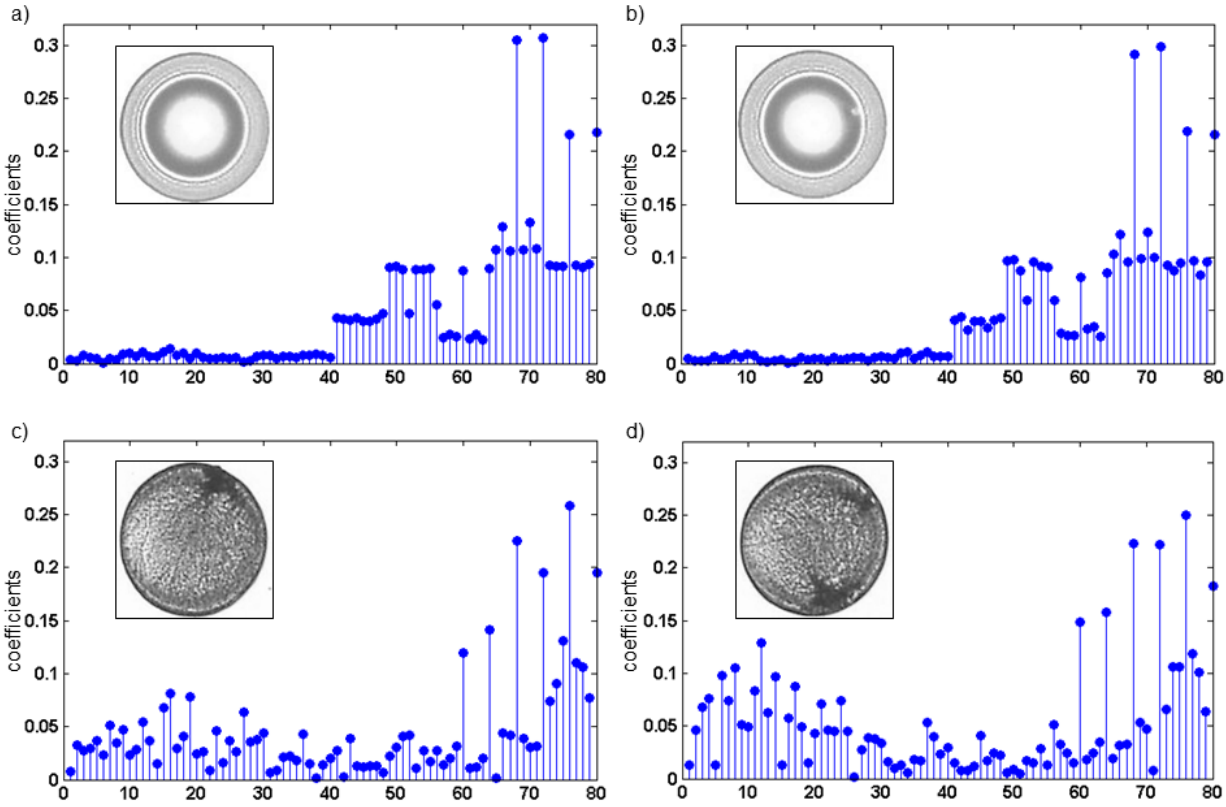

Figure 10.3. Stem plots of the Gabor wavelet coefficients (absolute value) with 10 scales for drops containing a), b) no NaCl and c), d) 1.00 g/100mL NaCl.

Figure 10.3 shows stem plots of the Gabor wavelet coefficients with 10 scales and 8 orientations (resulting in 80 coefficients). It should be noted that the coefficients shown actually represent the magnitude of the complex numbered coefficients and for illustration purposes, the absolute values of the coefficients were plotted. This figure illustrates the coefficients for two different images from each class: lysozyme with no NaCl (Fig. 10.3; a - b) and φ_N = 1.00 g/100mL NaCl (Fig. 10.3; c - d). From these plots, it is clear that the distribution of coefficients is similar overall for members of the same class, but distinct differences exist between the two classes. This was also true in comparing stem plots for the other two classes. Therefore, we assume this measurement vector should be a suitable representation for the drop deposit images.

10.4.1 Unsupervised Learning Algorithm

The k-means clustering algorithm was used, as described above, to group the deposit images in their respective classes, without *a priori* information. The initial cluster means for the four concentrations were initialized to zero and ten images were chosen at random as test images. The k-means clustering algorithm was applied to the Gabor wavelet coefficients (measurement vector) for each of the test images. The mean accuracy results for the various scales of the Gabor wavelet function with the unsupervised learning algorithm was 25%, 25%, 31%, and 34% for scales of 6, 8, 10, and 12, respectively. The program was run at least 5 times (with different test images selected at random) to determine the mean accuracy. The accuracy improved as the number of scales increased, though the overall accuracy of this method was poor. In this case, the φ_N = 0.10 g/100mL concentration was often misclassified as φ_N = 0.00 and the 0.50 g/100mL concentration was frequently misclassified as φ_N = 1.00 g/100mL. This suggests that these images are likely too similar for unsupervised learning techniques.

10.4.2 Supervised Learning Algorithm

To test the supervised learning algorithm, ten training images were chosen at random from the collection of images. The initial means for each class were calculated from the measurement vectors of these ten training images. Ten more images were chosen at random from the remaining images, which were considered test images. The algorithm was tested for the Gabor wavelet function with 6, 8, 10, and 12 scales and 8 orientations. Each of the test images were compared to the means and classified by minimizing the Euclidean distance to the mean. The classification accuracy for the supervised learning algorithm is given in Figure 10.4.

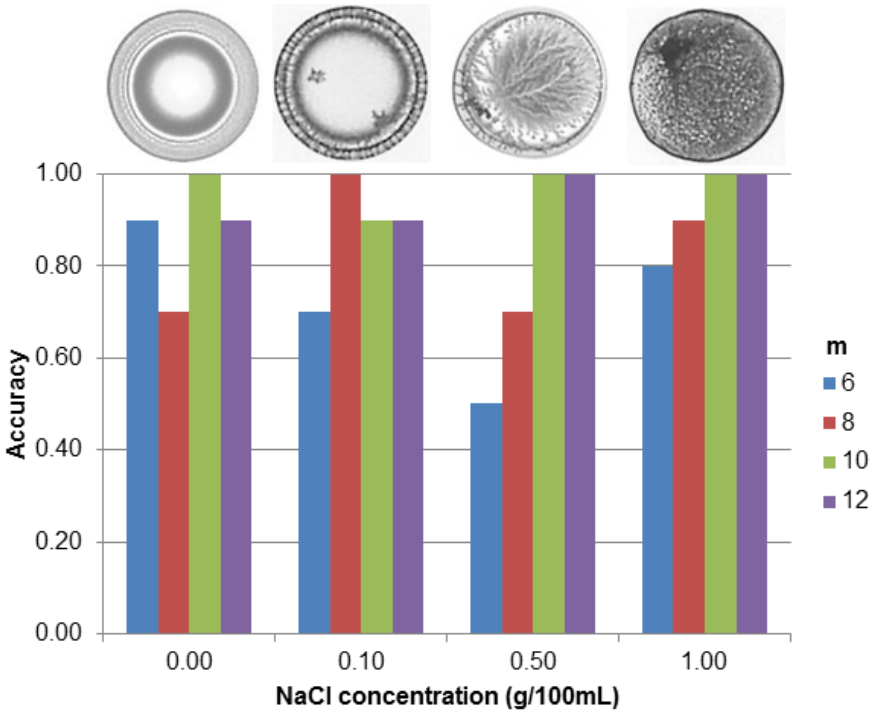

Figure 10.4. Mean accuracy results of the supervised learning algorithm for the Gabor wavelet function with 8 orientations and 6, 8, 10, and 12 scales.

Overall, the supervised learning method produced a mean accuracy of 73%, 82.5%, 97.5%, and 95% for scales of 6, 8, 10, and 12, respectively. The program was run at least 5 times to generate the mean accuracy with ten different training and test images selected at random. As the number of scales of the Gabor wavelet function increased, the accuracy improved. The algorithm was most successful with 10 and 12 scales and 8 orientations, with an overall accuracy of 97.5% and 95%. Like the unsupervised learning test, the most frequent misclassification occurred between φ_N = 0.00 and 0.10 g/100mL and between φ_N = 0.50 and 1.00 g/100mL.

10.5 DISCUSSION

Although this pilot study was largely designed as a proof of concept, the results for the supervised training algorithm are remarkable. These results are more accurate than those reported in the literature,[9,14] where a combination of several parameters (including the Gabor wavelet) were used as the measurement vector.

The unsupervised learning (k-means clustering) algorithm had an overall accuracy of 25%, 25%, 31%, and 34% for scales of 6, 8, 10, and 12, respectively. These poor results suggest that the drop images are too similar to properly cluster the measurement vectors into the appropriate classes with this algorithm. However, with the addition of training images in the supervised learning algorithm, the accuracy was greatly improved to 73%, 82.5%, 97.5%, and 95% for scales of 6, 8, 10, and 12, respectively. Of the four classes, the most frequently misclassified was the 0.50 g/100mL concentration. These were often misclassified as the 1.00 g/100mL concentration. In addition, the 0.10 g/100mL deposits were frequently misclassified for the deposits containing no salt. These misclassifications are likely due to the similarity of the patterns for some of these deposits.

As the number of scales of the Gabor wavelet function increased, the accuracy improved for both the unsupervised and supervised algorithms. The improvement in accuracy with the number of scales is a result of the multi-resolution nature of the wavelet. Taking the mother wavelet $\Psi(x, y)$ as in Equation 10.1, the variables *x'* and *y'* contain dilations of the size of the wavelet by 2^m and translations in angle by $\theta = k(\pi/8)$. The parameters *m* and *k* are the number of scales and number of orientations of the wavelet, which are the variables in this experiment. The parameter *k* changes the location of the wavelet, or represents the location of events in time or space. As the scaling parameter, *m*, changes, the shape of the wavelet changes resulting in a

representation of detail or resolution. For example, if the set of signals can be represented by the above equation with $m = 1$ and $k = 1$, then a larger set can be represented by $m = 2$ and $k = 2$. The basic signal is made half as wide and translated in steps half as wide, so this will represent a larger class of signals or in other words, give a better approximation of the signal. For example, in this experiment 10 scales and 8 orientations results in 80 Gabor filters, which is a suitable representation of the image, based on the results of this study. A perfect representation of the 150 x 150 pixel image would require 150 x 150 filters.[150]

The scalable nature of this algorithm is very attractive and can be easily optimized for various applications. In addition, the program is quite robust. The nature of the wavelet itself is well-suited to this type of computation. There is no calculus involved, just multiplication and addition, which are fundamental to a digital computer. The amount of time it takes for the program to determine the wavelet coefficients, compare to the means, and classify accordingly is on the order of seconds on a personal computer.

Overall, this study demonstrates that the patterns remaining after evaporation of simplified, model biofluids may act as a "fingerprint" for identifying the nature of the fluid. The results of this study with a supervised learning classification algorithm are remarkable and could have future implications in diagnostics applications. The next steps in development of this program include a larger training set and a greater number of classes. This method may also be improved by image preprocessing such as edge-detection as well as using higher resolution images.

11.0 CONCLUSIONS

The results contained in this PhD dissertation provide insight into the evaporative behavior and pattern formation in droplets of simplified model biological fluids containing lysozyme, DI water, and NaCl. The patterns that form depend sensitively on the evaporation conditions, characteristic time and length scales, and the physiochemical properties of the solution. These patterns are unique, dependent on solution chemistry, and may act as a "fingerprint" in identifying fluid properties. The research discussed in this dissertation highlights experiments that tested the primary hypothesis: that "incremental changes in experimental conditions will result in reproducible and statistically interpretable variations in the self-assembled patterns that develop during sessile droplet evaporation of simplified model biological fluids." The supplementary hypothesis was also explored: "the unique morphological patterns from simplified biofluids can act as a "fingerprint" for identification of these patterns based on solution chemistry."

The evaporation and pattern formation of lysozyme and DI water solutions on silicon wafer substrates is examined in Chapter 6 and summarized as follows. Just-deposited liquid drops exhibit a spherical cap shape with an initial contact angle of ~ 55º. Lysozyme molecules tend to adsorb on the substrate, covering the entire contact area at the liquid/substrate interface. Adsorption of the lysozyme molecules on the SiO_2 substrate pins the contact line of the droplet. The contact angle decreases with time and the non-uniform evaporation of the pinned sessile

droplet generates radial flows which carry un-adsorbed molecules to the perimeter of the drop where the evaporative flux is the highest. Simultaneously, a gel-like skin tends to form at the free surface while the protein molecules accumulate in the peripheral ring. A gel transition begins at the periphery and proceeds inward toward the center of the drop. The remaining liquid in the central region depins and recedes until evaporation is complete.

The patterns that remain on the substrate for drops with 20 μm < D < 50 μm showed negligible concentration dependence in the width and height of the ring, total volume of the deposit, and fraction of the total deposit contained in the outer ring. However, the volume fraction of lysozyme molecules in the deposit increased linearly with concentration. Thus, drops with higher lysozyme concentration in solution produced a denser, much more tightly packed lysozyme deposit, although the overall morphology was similar to that of the lower solution concentrations. In Chapter 6, this result was attributed to formation of a loosely packed gel-like structure of lysozyme molecules at the air-water interface which maintains the geometric shape observed in the deposit. This deposit geometry also depends on the contact angle at which the drop begins to recede, θ_r.

The influence of the characteristic time and length scales of the problem were examined in Chapter 7. Patterns were examined for drop diameters ranging from ~ 1 – 50 μm and two deposit regimes were observed: cap-like deposits for very small D and ring-like deposits when D > 20 μm. In this system, a critical diameter, D_C, exists for ring formation which depends on initial lysozyme concentration. When $D > D_C$, ring-like shapes are formed due to the transport of molecules to the periphery by capillary flow. The drop undergoes a phase transition, beginning from the highly concentrated ring area and moving inward toward the center of the still-liquid drop. When the contact angle reaches a critical value, the remaining liquid depins and

recedes toward the center of the droplet. The geometry of the lysozyme deposit is ring-like with an undulating interior and does not dependent on concentration. This was found for all deposits in this study with $D > 20$ μm.

When $D < D_C$, the deposit is uniform with a spherical cap-like shape. This shape occurs when diffusion is the dominant transport mechanism in this system. The transition between the two regimes can be described by finding the Peclet number for the experimental system. When $Pe > 1$, the deposit is ring-like as a result of dominant advection (radial flow). When $Pe < 1$, the deposit patterns are strongly dependent on concentration, with diffusion playing a major role in the transport of lysozyme particles. As Pe decreases, the deposit shapes become cap-like as a result of the dominant diffusive transport. As the initial lysozyme concentration increases, the critical diameter for ring formation increases. In Chapter 7, we proposed that the concentration dependent cap-like deposit was due to the droplet reaching the gelation concentration before reaching the critical receding angle, θ_r.

The influence of heat transfer on this system was examined in Chapter 8. The lysozyme solution droplets were deposited via aerosol on SiO_2 substrates heated to 30, 50, and 80°C. An increase in the substrate temperature led to a lower initial contact angle and a greater evaporation rate. In deposits formed on heated substrates, the peripheral rings were narrower, with higher peaks, compared to those deposited at room temperature. This effect was more pronounced with increased temperature. In addition, the thickness in the central region of the deposits on annealed substrates was much less than the room temperature deposits. This suggests that more lysozyme reaches the periphery when the substrate temperature is increased. Increasing the substrate temperature provides additional kinetic energy to help the molecules escape from the substrate. More lysozyme molecules will remain unadsorbed and able to reach the periphery of

the drop by the fluid flow. The rate of fluid flow is increased by the increase in the evaporative flux. This results in higher ring peaks and thinner central regions of the deposits at elevated substrate temperatures.

In Chapter 9, the effect of NaCl concentration on pattern formation in aqueous lysozyme sessile droplets is examined. The overall evaporation process for these solutions is as follows. As-deposited liquid drops exhibit a spherical cap shape with an initial contact angle of ~ 55º. Lysozyme molecules adsorb onto the substrate, pinning the droplet. The contact angle decreases during evaporation and the non-uniform evaporation of the pinned droplet generates radial flows which carry the un-adsorbed molecules to the perimeter of the drop. Protein molecules accumulate in the perimeter ring, undergoing a phase transition which proceeds inward toward the center of the drop. In solutions with minimal salt, the remaining liquid in the central region depins and recedes until evaporation is complete. In lysozyme solutions with higher salt concentrations, the contact angle continues to decrease while the remaining liquid evaporates. In the final stages of evaporation, the remaining liquid percolates through the solid deposit and is accompanied by extensive cracking in the perimeter ring and the formation of crystallites in the central region of the deposit.

The patterns that remain on the substrate show significant dependence on initial NaCl concentration. Three regions are generally formed and consist of a lysozyme-rich amorphous peripheral ring (Region I), a secondary ring like area consisting of larger lysozyme aggregates (Region II), and a central region which contains dendritic and crystalline structures (Region III). Unlike the lysozyme deposits studied in Chapters 6 – 8, the geometry of the deposits containing NaCl depend on the initial NaCl concentration. The width of the ring (Region I) decreases with increasing NaCl content. This is attributed to the formation of lysozyme aggregates at an earlier

time during evaporation which leads to the formation of Region II. Scanning Electron Microscopy (SEM) images shown in Chapter 9 reveal the multi-scale hierarchical nature of these lysozyme structures.

These patterns are further investigated in Chapter 10, where a novel image analysis and pattern recognition algorithm is presented. This program was developed to classify deposit images based on their solution concentrations. Deposit images were cropped from the original image, rescaled to 150 x 150 pixels, and converted to grayscale. The Gabor wavelet was utilized to extract feature information from the deposit images, as in iris recognition, for example. The number of scales of the wavelet (resolution) was varied, using scales of 6, 8, 10, and 12. Two different algorithms for classification were tested: unsupervised and supervised learning. The unsupervised learning algorithm was based on the k-means clustering algorithm, grouping the samples into clusters depending on the Euclidean distance to the nearest measurement vectors. The supervised learning algorithm was also based on the k-means algorithm, but incorporated training images to generate the initial cluster means.

The unsupervised learning algorithm achieved results of 25%, 25%, 31%, and 34% for Gabor wavelet scales of 6, 8, 10, and 12, respectively. These results were poor, but suggest that the drop images are too similar to properly cluster the measurement vectors into the appropriate classes with unsupervised learning. However, with the addition of training images in the supervised learning algorithm, the accuracy was greatly improved to 73%, 82.5%, 97.5%, and 95% for scales of 6, 8, 10, and 12, respectively. The improvement in accuracy with the number of scales is a result of the multi-resolution nature of the wavelet. In addition to the accuracy, the scalable and robust nature of this algorithm is remarkable and can be easily optimized for various applications.

Overall, this PhD dissertation demonstrates that incremental changes in experimental conditions results in "reproducible and statistically interpretable variations in the self-assembled patterns that develop during sessile droplet evaporation of simplified model biological fluids," as stated in the primary hypothesis. This research also revealed that the patterns remaining after evaporation of simplified, model biofluids (lysozyme, NaCl, and DI water) may act as a "fingerprint" for identifying the nature of the fluid, supporting the supplementary hypothesis. The patterns that remain from evaporation of simplified biofluids (lysozyme + NaCl) are broadly similar to the patterns from evaporation of human biofluids that have been reported in the literature. Therefore by studying these model systems, we can begin to understand more about the nature of pattern formation in more complicated "real" systems. Furthermore, the results of the pattern recognition algorithm in this study were exceptional and could lead to future applications in diagnostics.

There are several opportunities for extending this work. Further investigation could include using more realistic models of biofluids (e.g., tears) synthesized by adding various components to the solution or by using the real biofluids themselves to create a database of images. Further development of the pattern recognition program includes using larger training sets and a greater number of classes to better optimize these methods. The algorithm may also be improved by making use of image preprocessing such as edge-detection.

APPENDIX A

CODE FOR PATTERN RECOGNITION PROGRAM

The theory and results for the image analysis and pattern recognition algorithm were presented in Chapter 10. The basic C++ code for this pattern recognition program is presented in this Appendix. Three separate programs were written using C++ and the Insight ToolKit (ITK)[145] to preprocess the images and apply the Gabor wavelet, determine the means for each class, and to cluster or classify the image. A script was written to automate the process of selecting the images and performing the operations. First, the training images are selected for each class at random from each class's training image folder and the rest of the images are stored in a folder for test images. The script then calls GaborWavelet.exe on each training image and all of the images in the test images folder. The GaborWavelet program outputs similarly-named text files, each containing the wavelet coefficients of one input image. The script then calls MeanMaker.exe to find the mean wavelet coefficients of each class from the training images. These means are used as the initial means for the k-means algorithm, performed in SampleTester.exe. The SampleTester performs the clustering or classification based on the k-means algorithm. The source code for GaborWavelet.exe, MeanMaker.exe, and SampleTester.exe is given in the following appendices.

A.1 GABOR WAVELET

```
/*****************************************************************************
*                                                                            *
*      File:  GaborWavelet.cxx                                               *
*      Author:  Heather Meloy Gorr                                           *
*      Explanation:  Reads an input RGB image, converts to grayscale, specifies a  *
*      region of interest, applies the Gabor wavelet transform to the input image  *
*                                                                            *
*****************************************************************************/

// ITK header files
#include "itkRGBPixel.h"
#include "itkRGBToLuminanceImageFilter.h"
#include "itkRegionOfInterestImageFilter.h"
#include "itkVector.h"
#include "itkImageFileReader.h"
#include "itkImageRegionIterator.h"
#include "itkImageRegionIterator.h"
#include "itkImage.h"
#include "itkImageFileReader.h"
#include "itkImageFileWriter.h"
#include "itkRescaleIntensityImageFilter.h"
#include "itkGradientMagnitudeRecursiveGaussianImageFilter.h"

// Standard
#include <iomanip>
#include <time.h>
#include <cmath>
#include <iostream>
#include <fstream>
#include <cstdio>
#include <complex>
#include <vector>
#include <array>

#define      MAX_STRING 50
#define      MAX_ARRAY 30

using namespace std;

const unsigned int Dimension = 2;
const double pi = 3.141592658977;
const complex<double> i = complex<double>(0.0,1.0);

// Specify input and output pixel types and image types
typedef   itk::RGBPixel< unsigned char >            InputPixelType;
typedef   itk::Image<InputPixelType, Dimension>     InputImageType;
typedef   double                                    OutputPixelType;
typedef   itk::Image<OutputPixelType, Dimension>    OutputImageType;
```

```
// First the color image file is read, then converted to grayscale and cropped to the
// top-left RxR pixels
// Returns a pointer to the itkImage.

// Function which reads the input image
vector<complex<double>> getInputImage( char* fileName,int R);
OutputImageType::Pointer getInputImage( char* fileName);
// Function which generates transform coefficient matrix to be multiplied by the
// image intensity matrix
void gaborWavelet(int R, double Kmax, double f, int currentOrientation,
      int numOrientations, int currentScale, double delt2,
      vector<vector<complex<double>>> &GW);
// Function which does the matrix multiplication! returns GW_ALL * image
vector<complex<double>> multiplyMatrix( vector<vector<complex<double>>> GW_ALL,
vector<complex<double>> image);
// Function outputs grayscale of input image
void grayscale(char* inFile, char* outFile);

int main (int argc,char* argv[]) {
      if( argc < 5 )
      {
            // Inputs arguments from command line
            cerr << "\n\n Usage: " << argv[0] << " inputImageDimension numScales
            numOrientations inputImageFilename [coefficientTextFilename]\n\n";
            return EXIT_FAILURE;
      }

      int element = 5;                        // Initialize element counter
      int R = atoi(argv[1]);                  // Num of pixels in x (or y) direction
      int numScales = atoi(argv[2]);          // Number of scales
      int numOrientations = atoi(argv[3]);    // Number of orientations
      // Number of coefficients = numScales * numOrientations
      int numCoefficients = numScales*numOrientations;
      double Kmax = pi / 2;                   // Mathematical constants for wavelet
      double f = sqrt(2.0);
      double delt = 2 * pi;
      double delt2 = delt * delt;

      // Holds transform matrix generated by gaborWavelet Function
      vector<vector<complex<double>>> GW;
      // Holds GW multipled by each direction of the wavelet transform
      vector<vector<complex<double>>> GW_ALL;
      // Holds wavelet coefficients (measurement vector)
      vector<complex<double>> waveletCoefficients;
      // Holds the pixel values of the input image in a 1D list
      vector<complex<double>> image;

      // Set size of GW matrix
      GW.resize(R);
      for (int i = 0; i < R;i++) {
            GW[i].resize(R);
      }
```

```
// Set size of GW_ALL matrix
GW_ALL.resize(numCoefficients);
for (int i = 0; i < numCoefficients;i++) {
	GW_ALL[i].resize(R*R);
}
// Set size of wavelet coefficients matrix
waveletCoefficients.resize(numCoefficients);

// for loop to generate the GW_ALL matrix, makes several GW matrices
for (int currentScale = 0; currentScale < numScales; currentScale++) {
	//cout << "currentScale =" << currentScale <<endl;
	for (int currentOrientation = 1; currentOrientation <= numOrientations;
		currentOrientation++) {
		//cout << " currentOrientation=" << currentOrientation << endl;

		gaborWavelet ( R, Kmax, f, currentOrientation, numOrientations,
			currentScale, delt2, GW);

		int row = 0, col = 0;
		for (int element = 0; element < R*R;element++) {
			GW_ALL[(currentScale*8+currentOrientation)-1][element] =
				GW[row][col++];
			if(col == R) {
				row++;
				col = 0;
			}
		}
	}
}

// Returns the image pixel values as a vector of doubles
image = getInputImage(argv[4],R);

// Get the wavelet coefficients by doing matrix multiplication on the GW_ALL
// matrix and the vector of pixels
waveletCoefficients = multiplyMatrix(GW_ALL, image);

// Display the wavelet coefficients on screen
for (int i = 0; i < numCoefficients; i++) {
	double magnitude =
		sqrt(waveletCoefficients[i].real()*waveletCoefficients[i].real()+
		waveletCoefficients[i].imag()*waveletCoefficients[i].imag());
	cout << magnitude << endl;
}

// Output wavelet coefficients to a text file if a filename is provided
if( argc == 6 ) {
	ofstream fout;
	fout.open(argv[5]);
	for (int i = 0; i < numCoefficients; i++) {
		double magnitude =
		sqrt(waveletCoefficients[i].real()*waveletCoefficients[i].real()+
		waveletCoefficients[i].imag()*waveletCoefficients[i].imag());
		fout << magnitude << " \n";
	}
```

```
			fout.close();
		}

}

// gaborWavelet function
void gaborWavelet(int R, double Kmax, double f, int currentOrientation,
		int numOrientations, int currentScale, double delt2,
		vector<vector<complex<double>>> &GW) {

		complex<double> k = (Kmax / (pow(f,currentScale))) * exp( i *
			(currentOrientation * pi / numOrientations));
		double kn2 = abs(k*k);
		int index = 0;

		// Initialize GW matrix to zeros
		for (int r = 0 ;r<R;r++) {
			for (int c = 0;c<R;c++) {
				GW[r][c] = 0.0;
			}
		}
		// Creating the Gabor Wavelet coefficient matrix
		for (int m = -R/2 +1 ; m < R/2; m++) {
			for (int n = -R/2 +1 ;n < R/2; n++) {
				// Gabor function g(x,y)
				GW[m+R/2][n+R/2] = (kn2 / delt2) * exp(-0.5 * kn2 * (m*m + n*n) /
					delt2) * (exp(i * (k.real() * m + k.imag() * n)) - exp (-
					0.5 * delt2));
			}

		}

}

  // getInputImage, returns vector of doubles
  vector<complex<double>> getInputImage( char* fileName,int R) {
  vector<complex<double>> image;
  int element = 0;
  // Read the initial RGB image
  typedef itk::ImageFileReader< InputImageType >  ReaderType;
  ReaderType::Pointer reader = ReaderType::New();
  reader->SetFileName( fileName );


  // Use itk::RGBToLuminanceImageFilter to convert RGB image to grayscale
  typedef itk::RGBToLuminanceImageFilter< InputImageType, OutputImageType >
  		GrayscaleFilterType;
  GrayscaleFilterType::Pointer grayfilter = GrayscaleFilterType::New();
  // RegionOfInterestImageFilter is used to crop the image
  typedef itk::RegionOfInterestImageFilter< OutputImageType, OutputImageType >
  		ROIFilterType;
  ROIFilterType::Pointer ROIfilter = ROIFilterType::New();
```

```
  // Input region dimensions
  // Specify where region starts and how many pixels in each dimension
  OutputImageType::IndexType start;
  start[0] = 0;
  start[1] = 0;

  OutputImageType::SizeType size;
  size[0] = R;
  size[1] = R;

  OutputImageType::RegionType desiredRegion;
  desiredRegion.SetSize(  size  );
  desiredRegion.SetIndex( start );

  ROIfilter->SetRegionOfInterest( desiredRegion );

  // Filter pipeline
  grayfilter->SetInput( reader->GetOutput() );
  ROIfilter->SetInput( grayfilter->GetOutput() );
  ROIfilter->Update();

  // Iterate through the image region of interest
  typedef itk::ImageRegionIterator < OutputImageType > IteratorType;
  IteratorType iterator(ROIfilter->GetOutput(),ROIfilter->GetOutput()->
                  GetRequestedRegion());
  // Set size of image pixel vector
  image.resize(R*R);

       // Puts the pixel values of the input image into a 1D vector of doubles
       // Iterates through image

       for ( iterator.GoToBegin(); !iterator.IsAtEnd() ; ++iterator)    {
             image[element++] = iterator.Value();
       }
       return image;
}

// Read the image and grayscale
OutputImageType::Pointer getInputImage( char* fileName) {
  // Read the RGB image
  typedef itk::ImageFileReader< InputImageType >  ReaderType;
  ReaderType::Pointer reader = ReaderType::New();
  reader->SetFileName( fileName );


  // Use RGBToLuminanceImageFilter to convert to grayscale
  typedef itk::RGBToLuminanceImageFilter< InputImageType, OutputImageType >
                  GrayscaleFilterType;
  GrayscaleFilterType::Pointer grayfilter = GrayscaleFilterType::New();
  // RegionOfInterestImageFilter to crop the image
  typedef itk::RegionOfInterestImageFilter< OutputImageType, OutputImageType >
                  ROIFilterType;
  ROIFilterType::Pointer ROIfilter = ROIFilterType::New();
```

```
  // Input region dimensions
  // Specify where region starts and how many pixels in each dimension
  OutputImageType::IndexType start;
  start[0] = 0;
  start[1] = 0;
  OutputImageType::SizeType size;
  size[0] = R;
  size[1] = R;
  OutputImageType::RegionType desiredRegion;
  desiredRegion.SetSize(  size  );
  desiredRegion.SetIndex( start );

  ROIfilter->SetRegionOfInterest( desiredRegion );

  // Filter pipeline
  grayfilter->SetInput( reader->GetOutput() );
  ROIfilter->SetInput( grayfilter->GetOutput() );
  ROIfilter->Update();
  return ROIfilter->GetOutput();
}
// Matrix multiplication!
vector<complex<double>> multiplyMatrix(vector<vector<complex<double>>> GW_ALL,
                          vector<complex<double>> image)
{
      int i,k;
      vector<complex<double>> coef;
      coef.resize(GW_ALL.size());
      for( i = 0; i < GW_ALL.size(); i++) {
            coef[i]= 0;
            for (k = 0; k < GW_ALL[0].size();k++) {
                  coef[i] += GW_ALL[i][k]*image[k];
            }
      }
      return coef;
}
// Grayscale
void grayscale(char* inFile, char* outFile) {
      typedef itk::ImageFileWriter< OutputImageType >  WriterType;
       WriterType::Pointer writer = WriterType::New();
      writer->SetFileName( outFile );
      writer->SetInput( getInputImage(inFile));
  try
    {
    writer->Update();
    }
  catch( itk::ExceptionObject & excp )
    {
    std::cerr << "Exception Thrown" << std::endl;
    std::cerr << excp << std::endl;
    }
}
```

A.2 MEAN MAKER

```
/*****************************************************************************
*                                                                            *
*      File:  MeanMaker.cxx                                                  *
*      Author:  Heather Meloy Gorr                                           *
*      Explanation:  Takes mean of measurement vectors for training images from    *
*      each class                                                            *
*                                                                            *
*****************************************************************************/
/*
INPUTSCRIPT FILE FORMAT:
outFile (library)
mvSize
numClasses
ClassID 0
numFiles
FileNames
.
.
ClassID 1
numFiles
FileNames
.
.

OUTPUT FILE FORMAT:
mvSize
totalNumberOfFiles
FileNames
numClasses
classID
mean vector . . . . .
classID
mean vector . . . . .
*/
#include "itkListSample.h"
#include <fstream>
#include <cstdio>
#include <iostream>
#include <cmath>
#include <iomanip>
#include <string>
#include <list>
#include <queue>
using namespace std;

// Define measurement vector type
typedef itk::Array< float> MeasurementVectorType;
typedef itk::Statistics::ListSample< MeasurementVectorType > SampleType;
```

```
int main( int argc, char * argv[])
{
	if( argc < 2 )
	{
		std::cerr << std::endl << "Usage: " << argv[0] << " ScriptFile" <<
			std::endl;
		return EXIT_FAILURE;
	}

	int mvSize;
	int numClasses;
	int sanity;
	int numFiles;
	int classID;
	int totalNumberOfFiles = 0;
	string fileName;
	string outputFileName;
	string line;
	ifstream inFile;
	ofstream outFile;
	ifstream inputScript;
	queue<string> fileNameQueue;
	queue<int> classIDQueue;
	queue<MeasurementVectorType> mvQueue;

	// Script file contains filenames, number of classes, measurement vector size
	inputScript.open(argv[1]);
	getline (inputScript,outputFileName);
	getline (inputScript,line);
	mvSize = atoi(line.c_str());
	getline (inputScript,line);
	numClasses = atoi(line.c_str());

	SampleType::Pointer sample = SampleType::New();

	MeasurementVectorType mv(mvSize);
	MeasurementVectorType mvSUM(mvSize);
	sample->SetMeasurementVectorSize( mvSize );
	sanity = 4;


	for (int classCounter = 0; classCounter < numClasses; classCounter++) {
		getline (inputScript,line);
		classID = atoi(line.c_str());
		cout << classID << endl;
		getline (inputScript,line);
		numFiles = atoi(line.c_str());
		mvSUM.Fill(0);
		classIDQueue.push(classID);

		for (int fileCounter = 0; fileCounter < numFiles; fileCounter++) {
			getline (inputScript,fileName);
			cout << fileName << endl;
			inFile.open(fileName);
			fileNameQueue.push(fileName);
```

```
                totalNumberOfFiles++;

                for (int i = 0; i < mvSize ;i++) {
                        getline (inFile,line);
                        mv.SetElement(i,atof(line.c_str()));
                // This is holding the sum of all the measurement vectors so
                // later we can divide by numFiles to get MEAN of all MVs
                        mvSUM.SetElement(i,mvSUM.GetElement(i)+mv.GetElement(i));
                        if ( i % sanity == 0) cout << mv[i] << std::endl;
                }
                sample->PushBack( mv );
                inFile.close();
        }
        // Divides each elemental sum by the number of files to generate the
        // mean measurement vector for the class.
        // Use these mean MVs to seed the K-d Tree based K-means clustering
        // algorithm
        cout << "**************MEANS**************\n";
        for (int i = 0; i < mvSize; i++) {
                mvSUM.SetElement(i,mvSUM.GetElement(i)/numFiles);
        }
        mvQueue.push(mvSUM);
    }

    // Output file contains means
    outFile.open(outputFileName);
    outFile << mvSize << endl << totalNumberOfFiles << endl;
    for (int files = 0; files < totalNumberOfFiles; files++) {
        outFile << fileNameQueue.front() << endl;
        fileNameQueue.pop();
    }
    outFile << numClasses << endl;
    for (int classes = 0; classes < numClasses; classes++) {
        outFile << classIDQueue.front() << endl;
        classIDQueue.pop();
        mvSUM = mvQueue.front();
        mvQueue.pop();
        for (int i = 0; i < mvSize; i++) {
                outFile << mvSUM.GetElement(i) << " ";
                cout  << mvSUM.GetElement(i) << " ";
        }
        outFile << endl;
    }

    outFile.close();
    return 0;
}
```

A.3 SAMPLE TESTER

```
/*=========================================================================*
*                                                                          *
*      File:  SampleTester.cxx                                             *
*      Author:  Heather Meloy Gorr                                         *
*      Explanation:  Classification and clustering using k-d tree based k-means    *
*      clustering algorithm.  For unsupervised learning, initial means are set to  *
*      zero, for supervised learning, initial means are taken from MeanMaker.      *
*                                                                          *
*=========================================================================*/
/*INPUT FILE FORMAT:
mvSize
totalNumberOfFiles
FileNames
.
.
numClasses
classID
mean vector . . . . .
classID
mean vector . . . . .
.
.
*/

// ITK header files
#include "itkVector.h"
#include "itkListSample.h"
#include "itkKdTree.h"
#include "itkWeightedCentroidKdTreeGenerator.h"
#include "itkKdTreeBasedKmeansEstimator.h"
#include "itkMinimumDecisionRule.h"
#include "itkMembershipSample.h"
#include "itkSampleClassifierFilter.h"

// Standard
#include <fstream>
#include <cstdio>
#include <iostream>
#include <cmath>
#include <iomanip>
#include <string>
#include <list>
#include <math.h>
#include <cmath>

using namespace std;
const int sanity = 100;
```

```
int main( int argc, char * argv[])
{
	// If true, we are testing a new image.
	// If false, we are just displaying the current Library
	bool displayOnly = false;
	if (argc < 3) displayOnly = true;


	if( argc < 2 )
	{
		// Command line inputs
		std::cerr << std::endl << "Usage: " << argv[0] << " LibraryFile
			[newCoefficientsFile]" << std::endl;
		// "Library File" is the file generated by MeanMaker.exe
		// "newCoefficientsFile" is the optional new image coefficient file to
		// be classified by the sample tester

		return EXIT_FAILURE;
	}

	bool buggy = false;
	typedef itk::Array< float > MeasurementVectorType;
	typedef itk::Statistics::ListSample< MeasurementVectorType > SampleType;
	int choice = -1;
	int classID;
	int mvSize;
	int numClasses;
	int numFiles;
	int index = 0;
	int elementCounter = 0;
	char save = -1;
	float value;
	string line;
	string fileName;
	string newFileName;
	list<string> fileNameList;
	list<int> classIDList;
	list<MeasurementVectorType> estimatedMeanMVlist;
	list<string>::iterator currentFile;
	list<int>::iterator currentClassID;
	list<MeasurementVectorType>::iterator currentMViterator;
	ifstream meansFile;
	ifstream inFile;
	ofstream outFile;

	cout << "**********BEGIN INPUT SECTION**********\n";
	// This section reads the file generated by MeanMaker.exe (file names, class
	// ID's, initial means measurement vectors, etc..)
	// and puts them into variables and lists to be used later in the program.
	// It then adds the new file to be tested to the end of the file name list if
	// you are testing a new image
	meansFile.open(argv[1]);
	meansFile >> mvSize;
	meansFile >> numFiles;
	getline (meansFile,line);
```

```
MeasurementVectorType mv(mvSize);
MeasurementVectorType currentMV = MeasurementVectorType::Array(mvSize);

for (int fileCounter = 0; fileCounter < numFiles; fileCounter++) {
      getline (meansFile,fileName);
      fileNameList.push_back(fileName);
}
meansFile >> numClasses;
for (int classCounter = 0; classCounter < numClasses; classCounter++) {
      meansFile >> classID;
      classIDList.push_back(classID);
      for (int i = 0; i < mvSize;i++) {
            meansFile >> value;
            currentMV[i] = value;
      }
      estimatedMeanMVlist.push_back(currentMV);
}
meansFile.close();

// New file to be tested
if (!displayOnly) fileNameList.push_back(argv[2]);
cout << "**********************END INPUT SECTION**********************\n";

cout << "********************BEGIN STATISTICAL SECTION******************\n";

//********************BEGIN STATISTICAL SECTION*********************
SampleType::Pointer sample = SampleType::New();
sample->SetMeasurementVectorSize( mvSize );
SampleType::Pointer newSample = SampleType::New();
newSample->SetMeasurementVectorSize( mvSize );
// Generate k-d tree with vector sum and number of measurement vectors
typedef itk::Statistics::WeightedCentroidKdTreeGenerator< SampleType >
      TreeGeneratorType;
typedef TreeGeneratorType::KdTreeType TreeType;
// Use Euclidean distance (DistanceToCentroidMembershipFunction class) as
// membership function
typedef itk::Statistics::DistanceToCentroidMembershipFunction<
      MeasurementVectorType > MembershipFunctionType;
// Decision rule that returns the index of the membership functions that have
// the smallest value (minimum distance)
typedef itk::Statistics::MinimumDecisionRule DecisionRuleType;
DecisionRuleType::Pointer decisionRule = DecisionRuleType::New();

// To generate clusters, we create k instances of
// DistanceToCentroidMembershipFunction as the membership functions for each
// cluster
// Plug these and sample into the SampleClassifier object to get the
// membership sample which stores MVs and associated class labels
typedef itk::Statistics::SampleClassifierFilter< SampleType > ClassifierType;
typedef ClassifierType::ClassLabelVectorObjectType ClassLabelVectorObjectType;
typedef ClassifierType::ClassLabelVectorType ClassLabelVectorType;
typedef ClassifierType::ClassLabelType ClassLabelType;
typedef ClassifierType::MembershipFunctionVectorObjectType
      MembershipFunctionVectorObjectType;
```

```
typedef ClassifierType::MembershipFunctionVectorType
      MembershipFunctionVectorType;
// Produce k-mean estimates
typedef itk::Statistics::KdTreeBasedKmeansEstimator<TreeType> EstimatorType;



// This opens each file in the FileNameList and reads their measurement
// vectors into the sample (list of MV's)
for (currentFile = fileNameList.begin(); currentFile!=fileNameList.end() ;
      currentFile++) {
      inFile.open(*currentFile);
      if (buggy) std::cout << "hello " << *currentFile << "!" << std::endl;
      for (int i = 0; (i < sample->GetMeasurementVectorSize()) ;i++) {
            inFile >> value;
            mv.SetElement(i,value);
            if(buggy) if ( i % sanity == 0) std::cout << mv.GetElement(i) <<
                  std::endl;
      }
      sample->PushBack( mv );
      inFile.close();
}

// Generates K-d tree (of MVs) from the Sample (list of MVs)
TreeGeneratorType::Pointer treeGenerator = TreeGeneratorType::New();
treeGenerator->SetSample( sample );
treeGenerator->SetBucketSize( 16 );
treeGenerator->Update();


// Creates pointer to classifier
ClassifierType::Pointer classifier = ClassifierType::New();
// Classifier's decision rule is minimum decision rule
classifier->SetDecisionRule( decisionRule );
classifier->SetInput( sample );
// Number of classes based on input from MeansFile
classifier->SetNumberOfClasses( numClasses );
// Creates pointers to class label and membership function objects
ClassLabelVectorObjectType::Pointer classLabelsObject =
      ClassLabelVectorObjectType::New();
ClassLabelVectorType& classLabelsVector = classLabelsObject->Get();
MembershipFunctionVectorObjectType::Pointer membershipFunctionVectorObject =
      MembershipFunctionVectorObjectType::New();
MembershipFunctionVectorType& membershipFunctionVector =
      membershipFunctionVectorObject->Get();
EstimatorType::Pointer estimator = EstimatorType::New();
// Sets number of Initial Means elements to MVsize * number of classes
EstimatorType::ParametersType initialMeans(sample->
      GetMeasurementVectorSize()*numClasses);

classifier->SetClassLabels( classLabelsObject );
```

```
// This tells the classifier to use the means from the MeansFile as the
// initial means for classification
currentMViterator = estimatedMeanMVlist.begin();
for (list<int>::iterator currentClassID = classIDList.begin(); currentClassID
              != classIDList.end(); currentClassID++) {
       classLabelsVector.push_back( *currentClassID );
       if(buggy)cout << "my vectors! " << *currentClassID << endl;
       for (int i = 0; i < mvSize;i++) {
              value = currentMViterator->GetElement(i);
              if(buggy)if (i % sanity == 0) cout << value << endl;
              initialMeans.SetElement(elementCounter++,value);
       // The line below sets the initial means to 0 instead of the values from
       // the means file for unsupervised learning (comment out line above if
       // clustering
              //initialMeans.SetElement(elementCounter++,0);
       }
       currentMViterator++;
}
// Sending input parameters to the K-d Tree based K-means clustering estimator
estimator->SetParameters( initialMeans );
estimator->SetKdTree( treeGenerator->GetOutput() );
estimator->SetMaximumIteration( 200 );
estimator->SetCentroidPositionChangesThreshold(0.0);
estimator->StartOptimization();


// Displays the estimated means AFTER optimization.
// If you are not testing a new file, then these means should be the same as
// the initial means in the MeansFile
// They should vary slightly from the initial if you have added a new image
EstimatorType::ParametersType estimatedMeans = estimator->GetParameters();

for ( unsigned int i = 0 ; i < mvSize*numClasses ; ++i )
{
       if ( i % sanity == 0) {
              if(buggy) cout << "cluster[" << (i/mvSize)+1  << "] " <<
                     std::endl;
              if(buggy) cout << "    estimated mean : " << estimatedMeans[i] <<
                     std::endl;
       }
}
// Generating membership functions for each class by giving them the cluster
// means
index = 0;
for ( unsigned int i = 0 ; i < numClasses ; i++ )
{
       MembershipFunctionType::Pointer membershipFunction =
              MembershipFunctionType::New();
       MembershipFunctionType::CentroidType centroid( sample->
              GetMeasurementVectorSize() );
       for ( unsigned int j = 0 ; j < mvSize; j++ )
       {
              centroid[j] = estimatedMeans[index++];
       }
       membershipFunction->SetCentroid( centroid );
```

```
        membershipFunctionVector.push_back( membershipFunction.GetPointer() );
}
classifier->SetMembershipFunctions( membershipFunctionVectorObject );

classifier->Update();

// Create membership sample from classifier output. This gives us a list of
// the MVs and their class IDs
const ClassifierType::MembershipSampleType* membershipSample =
        classifier->GetOutput();
ClassifierType::MembershipSampleType::ConstIterator iter = membershipSample->
        Begin();
ClassifierType::MembershipSampleType::ConstIterator iter2 = iter;


// Iterate through membership sample, displaying file name and the class it
// belongs to.
// The membership sample holds only the MV's and their class ID's, not the
// file names, so we also iterate through the filename list to display the
// file name.
currentFile = fileNameList.begin();
bool increment = false;
while ( iter != membershipSample->End() )
{
        cout << "file: " << *currentFile
        << " class label = " << iter.GetClassLabel()
        << std::endl;
        ++iter;
        currentFile++;
        if (increment) {
                ++iter2;
        } else {
                increment = true;
        }
}

// This for-loop takes the new cluster means from the estimator and puts them
// back into the meanMV list so we can output the new cluster means to the new
// library file
elementCounter = 0;
estimatedMeanMVlist.clear();
estimatedMeans = estimator->GetParameters();
for (int classCounter = 0; classCounter < numClasses; classCounter++) {
        for (int i = 0; i < mvSize;i++) {
                currentMV[i] = estimatedMeans.GetElement(elementCounter++);
        }
        estimatedMeanMVlist.push_back(currentMV);
}
cout << "**********************END STATISTICAL SECTION**********************\n";
```

```
	// If we tested a new file and it was classified correctly, we can save our
	// new library (means) file to include updated filename lists and cluster
	// means
	if (!displayOnly) {
		cout << "\n\nfile: " << fileNameList.back()
			<< " class label = " << iter2.GetClassLabel()
			<< std::endl;
		string filename =
			fileNameList.back().substr(fileNameList.back().find('\\')+1);
		unsigned int trueClassID = atoi(filename.c_str());
		if(trueClassID == iter2.GetClassLabel()) {
			cout << "\n\n    *****CORRECT*****\n\n\n";
			return 42;
		} else {
			cout << "\n\n    *****XXwrongXX*****\n\n\n";
			return 66;
		}

		//"*********************BEGIN OUTPUT SECTION*********************\n";
		save = 'n';
		if (save == 'y' || save == 'Y') {


			cout << "Enter Output Filename: ";
			cin >> fileName;
			numFiles = fileNameList.size();
			outFile.open(fileName);
			outFile << mvSize << endl << numFiles << endl;
			for (currentFile = fileNameList.begin(); currentFile !=
				fileNameList.end() ; currentFile++) {
				outFile << *currentFile << endl;
			}
			outFile << numClasses << endl;

			currentMViterator = estimatedMeanMVlist.begin();
			for (list<int>::iterator currentClassID = classIDList.begin();
				currentClassID != classIDList.end(); currentClassID++) {
				outFile << *currentClassID << endl;
				for (int i = 0; i < mvSize;i++) {
					value = currentMViterator->GetElement(i);
					outFile << value << " ";
				}
				outFile << endl;
				currentMViterator++;
			}
			outFile.close();
		//cout << "*************END OUTPUT SECTION*********************\n";
		}
	}
	return 0;
}
```

BIBLIOGRAPHY

1. Ko, H.-Y.; Park, J.; Shin, H.; Moon, J. Rapid Self-Assembly of Monodisperse Colloidal Spheres in an Ink Jet Printed Droplet. *Chem. Mater.* **2004**, *16* (22), 4212-4215.

2. Park, J.; Moon, J. Control of Colloidal Particle Deposit Patterns within Picoliter Droplets Ejected by Ink-Jet Printing. *Langmuir* **2006,** *22*, 3506-3513.

3. Zhou, J. X.; Fuh, J. Y. H.; Loh, H. T.; Wong, Y. S.; Ng, Y. S.; Gray, J. J.; Chua, S. J. Characterization of Drop-on-Demand Microdroplet Printing. *Int. J. Adv. Manuf. Technol.* **2010,** *48*, 243-250.

4. Xu, J.; Attinger, D. Drop on Demand in a Microfluidic Chip. *Micromech. Microeng.* **2008,** *18*, 065020.

5. Small, W. R.; Walton, C. D.; Loos, J.; Panhuis, M. Carbon Nanotube Network Formation from Evaporating Sessile Drops. *J. Phys. Chem. B* **2006,** *110*, 13029-13036.

6. Dugas, V.; Broutin, J.; Souteyrand, E. Droplet Evaluation Study Applied to DNA Chip Manufacturing. *Langmuir* **2005,** *21*, 9130-9136.

7. Smalyukh, I. I.; Zribi, O. V.; Butler, J. C.; Lavrentovich, O. D.; Wong, G. C. L. Structure and Dynamics of Liquid Crystalline Pattern Formation in Drying Droplets of DNA. *Phys. Rev. Lett.* **2006,** *196*.

8. Rapis, E. A Change in the Physical State of a Nonequilibrium Blood Plasma Protein Film in Patients with Carcinoma. *Technical Physics* **2002,** *47* (4), 510-512.

9. Killeen, A. A.; Ossina, N.; McGlennen, R. C.; Minnerath, S.; Borgos, J.; Alexandrov, V.; Sarvazyan, A. Protein Self-Organization Patterns in Dried Serum Reveal Changes in B-Cell Disorders. *Mol. Diag. Ther.* **2006,** *10* (6), 371-380.

10. Yakhno, T. A.; Yakhno, V. G.; Sanin, A. G.; Sanina, O. A.; Pelyushenko, A. S.; Egorova, N.A.; Terentiev, I. G.; Smetanina, S. V.; Korochkina, O. V.; Yashukova, E. V. The Informative-Capacity Phenomenon of Drying Drops. *IEEE Eng. Med. Biol.* **2005,** *24* (2), 96-104.

11. Brutin, D.; Sobac, B.; Loquet, B.; Sampol, J. Pattern Formation in Drying Drops of Blood. *J. Fluid Mech.* **2011,** *667*, 85-95.

12. Sobac, B.; Brutin, D. Structural and Evaporative Evolutions in Desiccating Sessile Drops of Blood. *Phys. Rev. E* **2011,** *84*, 011603.

13. Shabalin, V. N.; Shatokhina, S. N. Diagnostic Markers in the Structures of Human Biological Liquids. *Singap. Med. J.* **2007,** *48* (5), 440-446.

14. Kim, N.; Li, Z.; Hurth, C.; Zenhausern, F.; Chang, S. F.; Attinger, D. Identification of Fluid and Substrate Chemistry Based on Automatic Pattern Recognition of Stains. *Anal. Methods* **2012,** *4*, 50-57.

15. Deegan, R. D.; Bakajin, O.; Dupont, T. F.; Huber, G.; Nagel, S. R.; Witten, T. A. Capillary Flow as the Cause of Ring Stains From Dried Liquid Drops. *Nature* **1997,** *389*, 827-829.

16. Deegan, R. D. Pattern Formation in Drying Drops. *Phys. Rev. E* **2000,** *61* (1), 475-485.

17. Deegan, R. D.; Bakajin, O.; Dupont, T. F.; Huber, G.; Nagel, S. R.; Witten, T. A. Contact Line Deposits in an Evaporating Drop. *Phys. Rev. E* **2000,** *62* (1), 756-762.

18. Popov, Y. O. Evaporative Deposition Patterns: Spatial Dimensions of the Deposit. *Phys. Rev. E* **2005,** *71*, 36313.

19. Fischer, B. J. Particle Convection in an Evaporating Colloidal Droplet. *Langmuir* **2002,** *18*, 60-67.

20. Hu, H.; Larson, R. G. Analysis of the Microfluid Flow in an Evaporating Sessile Droplet. *Langmuir* **2005,** *21*, 3963-3971.

21. Hu, H.; Larson, R. G. Marangoni Effect Reverses Coffee-Ring Depositions. *J. Phys. Chem. B.* **2006,** *110*, 7090-7094.

22. Bhardwaj, R.; Fang, X.; Attinger, D. Pattern Formation During the Evaporation of a Colloidal Nanoliter Drop: A Numerical and Experimental Study. *New J. Phys.* **2009,** *11*, 075020-075053.

23. Shen, X.; Ho, C.-M.; Wong, T.-S. Minimal Size of Coffee Ring Structure. *J. Phys. Chem. B* **2010,** *114*, 5269-5274.

24. Andreeva, L. V.; Koshkin, A. V.; Lebedev-Stepanov, P. V.; Petrov, A. N.; Alfimov, M. V. Driving Forces of the Solute Self-Organization in an Evaporating Liquid Microdroplet. *Colloid. Surface. A* **2007,** *300*, 300-306.

25. Bhardwaj, R.; Fang, X.; Somasundaran, P.; Attinger, D. Self-assembly of Particles From Evaporating Colloidal Droplets: Role of the pH and Proposition of a Phase Diagram. *Langmuir* **2010,** *26* (11), 7833-7842.

26. Yunker, P. J.; Still, T.; Lohr, M. A.; Yodh, A. G. Suppression of the Coffee-Ring Effect by Shape-Dependent Capillary Interactions. *Nature* **2011,** *476*, 308-311.

27. Pauchard, L.; Allain, C. Stable and Unstable Surface Evolution During the Drying of a Polymer Solution Drop. *Phys. Rev. E* **2003,** *68*.

28. Gorand, Y.; Pauchard, L.; Calligari, G.; Hulin, J. P.; Allain, C. Mechanical Instability Induced by the Desiccation of Sessile Drops. *Langmuir* **2004,** *20*, 5138-5140.

29. Okuzono, T.; Kobayashi, M.; Doi, M. Final Shape of a Drying Thin Film. *Phys. Rev. E* **2009,** *80*.

30. Socol, Y.; Guzman, I. S. Fast Ring-Shape Self-Assembling in Water-Based Ink-Jetted Droplets. *J. Phys. Chem. B* **2006,** *110*, 18347-18350.

31. Sangani, A. S.; Lu, C.; Su, K.; Schwarz, J. A. Capillary Force on Particles Near a Drop Edge Resting on a Substrate and a Criterion for Contact Line Pinning. *Phys. Rev. E* **2009,** *80*.

32. Wong, T.-S.; Chen, T.-H.; Shen, X.; Ho, C.-M. Nanochromatography Driven by the Coffee Ring Effect. *Anal. Chem.* **2011,** *83* (6), 1871-1873.

33. Gorr, H. M.; Zueger, J. Z.; Barnard, J. A. Lysozyme Pattern Formation in Evaporating Drops. *Langmuir* **2012,** *28* (9), 4039-4042.

34. Gorr, H. M.; Zueger, J. M.; Barnard, J. A. Characteristic Size for Onset of Coffee-Ring Effect in Evaporating Lysozyme-Water Solution Droplets. *J. Phys. Chem. B* **2012** *116* (40), 12213-12220.

35. Gorr, H. M.; Zueger, J. M.; McAdams, D. R.; Barnard, J. A. Salt-Induced Pattern Formation in Evaporating Droplets of Lysozyme Solutions. *Colloid. Surface. B* **2013**, *103*, 59-66.

36. Young, T. An Essay on the Cohesion of Fluids. *Philos. Trans. R. Soc.* **1805,** *95*, 65-87.

37. Maxwell, J. C.; Niven, W. D. *The Scientific Papers of James Clerk Maxwell*. Cambridge University Press, 1890.

38. de Gennes, P. G. Wetting: Statics and Dynamics. *Rev. Mod. Phys.* **1985,** *57* (3), 827-863.

39. de Gennes, P. G. Solvent Evaporation of Spin Cast Films: Crust Effects. *Eur. Phys. J. E.* **2002,** *7*, 31-34.

40. Guena, G.; Poulard, C.; Cazabat, A. M. The Leading Edge of Evaporating Droplets. *J. Colloid Interf. Sci.* **2007,** *312*, 164-171.

41. Maki, K. L.; Kumar, S. Fast Evaporation of Spreading Droplets of Colloidal Suspensions. *Langmuir* **2011,** *27*, 11347-11363.

42. de Gennes, P. G.; Brochard-Wyart, F.; Quere, D. *Capillarity and Wetting Phenomena. Drops, Bubbles, Pearls, Waves*. Springer: New York, 2004.

43. Hu, H.; Larson, R. G. Evaporation of a Sessile Droplet on a Substrate. **2002,** *106*, 1334-1344.

44. Langmuir, I. The Constitution and Fundamental Properties of Solids and Liquids. II. Liquids. *J. Am. Chem. Soc.* **1917,** *39* (9), 1848-1906.

45. Sommer, A. P.; Rozlosnik, N. Formation of Crystalline Ring Patterns on Extremely Hydrophobic Supersmooth Substrates: Extension of Ring Formation Paradigms. *Cryst. Growth Des.* **2005,** *5* (2), 551-557.

46. Hu, H.; Larson, R. G. Analysis of the Effects of Marangoni Stresses on the Microflow in an Evaporating Sessile Droplet. *Langmuir* **2005,** *21*, 3972-3980.

47. Sommer, A. P. Limits of the Impact of Gravity on Self-Organizing Nanospheres. *J. Phys. Chem. B* **2004,** *108*, 8096-8098.

48. Sommer, A. P.; Franke, R. P. Biomimicry Patterning with Nanosphere Suspensions. *Nano Letters* **2003,** *3* (5), 573-575.

49. Wang, J.; Evans, J. R. G. Drying Behaviour of Droplets of Mixed Powder Suspensions. *J. Eur. Ceram. Soc.* **2006,** *26*, 3123-3131.

50. Sandu, I.; Fleaca, C. T. The Influence of Gravity on the Distribution of the Deposit Formed onto a Substrate by Sessile, Hanging, and Sandwiched Hanging Drop Evaporation. *J. .Colloid Interf. Sci.* **2011,** *358*, 621-625.

51. Wang, J.; Evans, J. R. G. Segregation in Multicomponent Ceramic Colloids During Drying of Droplets. *Phys. Rev. E* **2006,** *73*.

52. Zhang, Y.; Chen, L.; Yang, S.; Evans, J. R. G. Control of Particle Segregation During Drying of Ceramic Suspension Droplets. *J.Eur. Ceram. Soc.* **2007,** *27*, 2229-2235.

53. Zhang, Y.; Yang, S.; Chen, L.; Evans, J. R. G. Shape Changes During the Drying of Droplets of Suspensions. *Langmuir* **2008,** *24* (8), 3752-3758.

54. Takhistov, P.; Chang, H.-C. Complex Stain Morphologies. *Ind. Eng. Chem. Res.* **2002,** *41*, 6256-6269.

55. Stefaniuk, T.; Wrobel, P.; Dominiak, R.; Gawlik, G.; Bajdor, K.; Zielecka, M.; Szoplik, T. Self-assembly of Arrays of Micro-Rings by Colloidal Evaporative Deposition. *Surf. Sci.* **2007,** *601*, 4922-4924.

56. Parisse, F.; Allain, C. Drying of Colloidal Suspension Droplets: Experimental Study and Profile Renormalization. *Langmuir* **1997,** *13*, 3598-3602.

57. Moffat, J. R.; Sefiane, K.; Shanahan, M. E. R. Effect of TiO_2 Nanoparticles on Contact Line Stick-Slip Behavior of Volatile Drops. *J. Phys. Chem. B* **2009,** *113*, 8860-8866.

58. Nellimoottil, T. T.; Rao, P. N.; Ghosh, S. S.; Chattopadhyay, A. Evaporation-Induced Patterns from Droplets Containing Motile and Nonmotile Bacteria. *Langmuir* **2007,** *23*, 8655-8658.

59. Yakhno, T. A.; Kazakov, V. V.; Sanina, O. A.; Sanin, A. G.; Yakhno, V. G. Drops of Biological Fluids Drying on a Hard Substrate: Variation of the Morphology, Weight, Temperature, and Mechanical Properties. *Technical Physics* **2010,** *55* (7), 17-23.

60. Yakhno, T. A.; Sanin, A. G.; Pelyushenko, A. S.; Kazakov, V. V.; Shaposhnikova, O.; Chernov, A.; Yakhno, V. G.; Vacca, C.; Falcione, F.; Johnson, B. Uncoated Quartz Resonator as a Universal Biosensor. *Biosens. Bioelectron.* **2007,** *22*, 2127-2131.

61. Annarelli, C. C.; Fornazero, J.; Bert, J.; Colombani, J. Crack Patterns in Drying Protein Solution Drops. *Eur. Phys. J. E* **2001,** *5*, 599-603.

62. Chen, G.; Mohamed, G. J. Complex Protein Patterns Formation via Salt-Induced Self-Assembly and Droplet Evaporation. *Eur. Phys. J. E* **2010,** *33*, 19-26.

63. Yan, Q.; Gao, L.; Sharma, V.; Chiang, Y.-M.; Wong, C. C. Particle and Substrate Charge Effects on Colloidal Self-Assembly in a Sessile Drop. *Langmuir* **2008,** *24*, 11518-11522.

64. Kajiya, T.; Kobayashi, W.; Okuzono, T.; Doi, M. Controlling the Drying and Film Formation Processes of Polymer Solution Droplets with Addition of Small Amount of Surfactants. *J. Phys. Chem. B* **2009,** *2009* (113), 15460-15466.

65. Kajiya, T.; Kobayashi, W.; Okuzono, T.; Doi, M. Controlling Profiles of Polymer Dots by Switching Between Evaporation and Condensation. *Langmuir* **2010,** *26* (13), 10429-10432.

66. Pauchard, L.; Parisse, F.; Allain, C. Influence of Salt Content on Crack Patterns Formed Through Colloidal Suspension Desiccation. *Phys. Rev. E* **1999,** *59*.

67. Li, F.-I.; Thaler, S. M.; Leo, P. H.; Barnard, J. A. Dendrimer Pattern Formation in Evaporating Drops. *J. Phys. Chem. B* **2006,** *110* (51), 25838-25843.

68. Li, F.-I.; Thaler, S. M.; Leo, P. H.; Barnard, J. A. Dendrimer Pattern Formation in Evaporating Drops: Solvent, Size, and Concentration Effects. *J. Phys. Chem. C* **2006**, *112* (37), 14266-14273.

69. Li, F.-I.; Leo, P. H.; Barnard, J. A. Temperature-Dependent Formation of Dendrimer Islands from Ring Structures. *J. Phys. Chem. B* **2008,** *112* (51), 16497-16504.

70. Girard, F.; Antoni, M.; Faure, S.; Steinchen, A. Influence of Heating Temperature and Relative Humidity in the Evaporation of Pinned Droplets. *Colloid. Surf. A* **2008,** *323*, 36-49.

71. Girard, F.; Antoni, M. Influence of Substrate Heating on the Evaporation Dynamics of Pinned Water Droplets. *Langmuir* **2008,** *24*, 11342-11345.

72. Girard, F.; Antoni, M.; Sefiane, K. On the Effect of Marangoni Flow on Evaporation Rates of Heated Water Drops. *Langmuir* **2008,** *24*, 9207-9210.

73. Sefiane, K.; Bennacer, R. An Expression for Droplet Evaporation Incorporating Thermal Effects. *J. Fluid Mech.* **2011,** *667*, 260-271.

74. Sefiane, K. On the Formation of Regular Patterns from Drying Droplets and Their Potential Use for Bio-Medical Applications. *J. Bionic Eng.* **2010**, S82-S93.

75. Kim, J. H.; Park, S. B.; Kim, J. H.; Zin, W. C. Polymer Transports Inside Evaporating Water Droplets at Various Substrate Temperatures. *J. Phys. Chem. C* **2011,** *115*, 15375-15383.

76. Girard, F.; Antoni, M.; Sefiane, K. Infrared Thermography Investigation of an Evaporating Sessile Water Droplet on Heated Substrates. *Langmuir* **2010,** *26* (7), 4576-4580.

77. Yakhno, T. A.; Sedova, O. A.; Sanin, A. G.; Pelyushenko, A. S. On the Existence of Regular Structures in Liquid Human Blood Serum (Plasma) and Phase Transitions in the Course of Its Drying. *Technical Physics* **2003,** *48* (4), 399-403.

78. Yakhno, T. A.; Yakhno, V. G. Structural Evolution of Drying Drops of Biological Fluids. *Technical Physics* **2009,** *54* (8), 1219-1227.

79. Kuo, M.-T.; Lin, C.-C.; Liu, H.-Y.; Chang, H.-C. Tear Analytical Model Based on Raman Microspectroscopy for Investigation of Infectious Diseases of the Ocular Surface. *Invest. Ophthalm. Vis. Sci.* **2011,** *52* (7), 4942-4950.

80. Ravazzoni, L.; Ghini, C.; Macri, A.; Rolando, M. Tear Ferning as a Predictive Test for Contact Lens Tolerance. *Invest. Ophthalm. Vis. Sci.* **1997,** *38* (4), s153.

81. Pearce, E. I.; Tomlinson, A. Spatial Location Studies on the Chemical Composition of Human Tear Ferns. *Ophthal. Physiol. Opt.* **2000,** *20* (4), 306-313.

82. Ortiz, C.; Zhang, D.; Xie, Y.; Ribbe, A. E.; Ben-Amotz, D. Validation of the Drop Coating Deposition Raman Method for Protein Analysis. *Anal. Biochem.* **2006,** *353*, 157-166.

83. Sariri, R.; Ghafoori, H. Tear Proteins in Health, Disease, and Contact Lens Wear. *Biochemistry (Moscow)* **2008,** *73* (4), 381-392.

84. Wang, L.; Mizaikoff, B. Application of Multivariate Data-analysis Techniques to Biomedical Diagnostics Based on Mid-infrared Spectroscopy. *Anal. Bioanal. Chem.* **2008,** *391*, 1641-1654.

85. Lee, Y.; Wong, D. T. Saliva: An Emerging Biofluid for Early Detection of Diseases. *Am. J. Dent.* **2009,** *22* (4), 241-248.

86. Hu, S.; Arellano, M.; Boontheung, P.; Wang, J.; Zhou, H.; Jiang, J.; Elashoff, D.; Wei, R.; Loo, J.; Wong, D. T. Salivary Proteomics for Oral Cancer Biomarker Discovery. *Clin. Cancer Res.* **2008,** *14* (19), 6246-6252.

87. Schattka, B.; Alexander, M.; Ying, S. L.; Man, A.; Shaw, R. A. Metabolic Fingerprinting of Biofluids by Infrared Spectroscopy: Modeling and Optimization of Flow Rates for Laminar Fluid Diffusion Interface Sample Preconditioning. *Anal. Chem.* **2011,** *83*, 555-562.

88. Omenn, G. S. Advancement of Biomarker Discovery and Validation Through the HUPO Plasma Protenome Project. *Dis. Markers* **2004,** *20*, 131-134.

89. Cardinaux, F.; Stradner, A.; Schurtenberger, P.; Sciortino, F.; Zaccarelli, E. Modeling Equilibrium Clusters in Lysozyme Solutions. *Europhys. Lett.* **2007,** *77*.

90. Trappe, V.; Prasad, V.; Cipelletti, L.; Segre, P. N.; Weitz, D. A. Jamming Phase Diagram for Attractive Particles. *Nature* **2001,** *411*, 772-775.

91. Pauchard, L.; Parisse, F.; Allain, C. Influence of Salt Content on Crack Patterns Formed Through Colloidal Suspension Desiccation. *Phys. Rev. E* **1999,** *59* (3), 3737-3740.

92. Pauchard, L.; Allain, C. Buckling Instability Induced by Polymer Solution Drying. *Europhys. Lett.* **2003,** *62* (6), 897-903.

93. Rapis, E. On the Nonequilibrium Phase Transition in Protein. *Technical Physics* **2007,** *552* (6), 787-792.

94. Pauchard, L. Patterns Caused by Buckle-Driven Delamination in Desiccated Colloidal Gels. *Europhys. Lett.* **2006,** *74* (1), 188-194.

95. Kaya, D.; Belyi, V. A.; Muthukumar, M. Pattern Formation in Drying Droplets of Polyelectrolyte and Salt. *J. Chem. Phys.* **2010,** *113*.

96. Yakhno, T. Salt-induced Protein Phase Transitions in Drying Drops. *J. Colloid Interf. Sci.* **2008,** *318*, 225-230.

97. Pusey, M. L.; Snyder, R. S.; Naumann, R. Protein Crystal Growth: Growth Kinetics for Tetragonal Lysozyme Crystals. *J. Biol. Chem.* **1986,** *261* (14), 6524-6529.

98. Liu, Y.; Wang, X.; Ching, C. B. Toward Further Understanding of Lysozyme Crystallization: Phase Diagram, Protein-Protein Interaction, Nucleation Kinetics, and Growth Kinetics. *Cryst. Growth Des.* **2010,** *10*, 548-558.

99. Umbach, P.; Georgalis, Y.; Saenger, W. Time-Resolved Small-Angle Static Light Scattering on Lysozyme During Nucleation and Growth. *J. Am. Chem. Soc.* **1998,** *120*, 2382-2390.

100. Selimovic, S.; Jia, Y.; Fraden, S. Measuring the Nucleation Rate of Lysozyme using Microfluidics. *Cryst. Growth Des.* **2009,** *9* (4), 1806-1810.

101. Muschol, M.; Rosenberger, F. Liquid-Liquid Phase Separation in Supersaturated Lysozyme Solutions and Associated Precipitate Formation/Crystallization. *J. Chem. Phys.* **1997,** *107* (6), 1953-1962.

102. Kim, D. T.; Blanch, H. W.; Radke, C. J. Direct Imaging of Lysozyme Adsorption onto Mica by Atomic Force Microscopy. *Langmuir* **2002,** *18*, 5841-5850.

103. Radmacher, M.; Fritz, M.; Cleveland, J. P.; Walters, D. A.; Hansma, P. K. Imaging Adhesion Forces and Elasticity of Lysozyme Adsorbed on Mica with the Atomic Force Microscope. *Langmuir* **1994,** *10*, 3809-3814.

104. Leisten, F.; Wiechmann, M.; Enders, O.; Kolb, H.-A. Generation of Nanostructures of Mica Supported Lysozyme Molecules in Aqueous Solution by Atomic Force Microscopy. *J. Colloid Interf. Sci.* **2006,** *298*, 508-514.

105. Blomberg, E.; Claesson, P. M.; Froberg, J. C.; Tilton, R. D. Interaction Between Adsorbed Layers of Lysozyme Studied with the Surface Force Technique. *Langmuir* **1994,** *10*, 2325-2334.

106. Daly, S. M.; Przybycien, T. M.; Tilton, R. D. Aggregation of Lysozyme and of Poly(ethylene glycol)-Modified Lysozyme After Adsorption to Silica. *Colloid. Surface. B* **2007,** *57*, 81-88.

107. Blake, C. C. F.; Koenig, D. F.; Mair, G. A.; North, A. C. T.; Phillips, D. C.; Sarma, V. R. Structure of Hen Egg-white Lysozyme. A Three-dimensional Fourier Synthesis at 2 Angstrom Resolution. *Nature* **1965,** *206*, 757-761.

108. Tilton, R. D.; Blomberg, E.; Claesson, P. M. Effect of Anionic Surfactant on Interactions Between Lysozyme Layers Adsorbed on Mica. *Langmuir* **1993,** *9*, 2102-2108.

109. Chang, B. H.; Bae, Y. C. Lysozyme-Lysozyme and Lysozyme-Salt Interactions in the Aqueous Saline Solution: A New Square-Well Potential. *Biomacromolecules* **2003,** *4*, 1713-1718.

110. Rozhkov, S. P.; Goryunov, A. S. Thermodynamic Study of Protein Phases Formation and Clustering in Model Water-Protein-Salt Solutions. *Biophys. Chem.* **2010,** *151*, 22-28.

111. Retailleau, P.; Ries-Kautt, M.; Ducruix, A. No Salting-In of Lysozyme Chloride Observed at Low Ionic Strength Over a Large Range of pH. *Biophys. J.* **1997,** *73*, 2156-2163.

112. Elgersma, A. V.; Ataka, M.; Katsura, T. Kinetic Studies on the Growth of Three Crystal Forms of Lysozyme Based on the Measurement of Protein and Cl^- Concentration Changes. *J. Cryst. Growth* **1992,** *122*, 31-40.

113. Georgalis, Y.; Umbach, P.; Soumpasis, D. M.; Saenger, W. Dynamics and Microstructure Formation During Nucleation of Lysozyme Solutions. *J. Am. Chem. Soc.* **1998,** *120*, 5539-5548.

114. Heijna, M. C. R.; Theelen, M. J.; van Enckevort, W. J. P.; Vlieg, E. Spherulitic Growth of Hen Egg-White Lysozyme Crystals. *J. Phys. Chem. B* **2007,** *111*, 1567-1573.

115. Price, W. S.; Tsuchiya, F.; Arata, Y. Lysozyme Aggregation and Solution Properties Studied Using PGSE NMR Diffusion Measurements. *J. Amer. Chem. Soc.* **1999,** *121* (49), 11503-11512.

116. Nesmelova, I. V.; Skirda, V. D.; Fedotov, V. D. Generalized Concentration Dependence of Globular Protein Self-Diffusion Coefficients in Aqueous Solutions. *Biopolymers* **2002,** *63*, 132-140.

117. Tokuyama, M.; Oppenheim, I. Dynamics of Hard-Sphere Suspensions. *Phys. Rev. E.* **1994,** *50*, R16-R19.

118. Daugman, J. U.S. Patent No. 5,291,560: Biometric Personal Identification System Based on Iris Analysis. **1994**.

119. Fong, S. Using Heirarchical Time Series Clustering Algorithm and Wavelet Classifier for Biometric Voice Classification. *J. Biomed. Biotechnol.* **2012,** *2012*, 1-12.

120. Istepanian, R. S. H.; Sungoor, A.; Nebel, J. Linear Predictive Coding and Wavelet Decomposition for Robust Microarray Data Clustering. *Conf. Proc. IEEE Eng. Med. Biol. Soc* **2007**, 4629-4632.

121. Snyder, W.; Qi, H. *Machine Vision*. Cambridge University Press: 2004.

122. Jolivalt, C.; Ries-Kautt, M.; Chevallier, P.; Ducruix, A. X-ray Fluorescence Used to Characterize the Salt Content of Proteins. *J. Synchrotron Rad.* **1997,** *4*, 28-35.

123. Su, T. J.; Lu, J. R.; Thomas, R. K.; Cui, Z. F.; Penfold, J. The Adsorption of Lysozyme at the Silica-Water Interface: A Neutron Reflection Study. *J. Colloid Interf. Sci.* **1998,** *203*, 419-429.

124. Daly, S. M.; Przybycien, T. M.; Tilton, R. D. Coverage-Dependent Orientation of Lysozyme Adsorbed on Silica. *Langmuir* **2003,** *19*, 3848-3857.

125. Vertegel, A. A.; Siegel, R. W.; Dordick, J. S. Silica Nanoparticle Size Influences the Structure and Enzymatic Activity of Adsorbed Lysozyme. *Langmuir* **2004,** *20*, 6800-6807.

126. Blossey, R.; Bosio, A. Contact Line Deposits on cDNA Microarrays: A "Twin-Spot Effect." *Langmuir* **2002,** *18*, 2952-2954.

127. NanoScope Command Reference Manual. 5.12 ed.; Veeco Metrology Group, 2001.

128. Klapetek, P.; Necas, D.; Anderson, C. Data Leveling and Background Subtraction. http://gwyddion.net/documentation/user-guide-en/.

129. Klapetek, P.; Nečas, D.; Campbellová, A.; Yacoot, A.; Koenders, L. Methods for Determining and Processing 3D Errors and Uncertainties for AFM Data Analysis. *Meas. Sci. Technol.* **2011,** *22*.

130. Liu, J.; Yang, W.-J. Thermophysical Properties of Lysozyme (Protein) Solutions. *J. Thermophys. Heat Tr.* **1992,** *6* (3), 531-536.

131. Sundaram, S.; Ferri, J. K.; Vollhardt, D.; Stebe, K. J. Surface Phase Behavior and Surface Tension Evolution for Lysozyme Adsorption onto Clean Interfaces and into DPPC Monolayers: Theory and Experiment. *Langmuir* **1998,** *14*, 1208-1218.

132. Alahverdjieva, V. S.; Grigoriev, D. O.; Ferri, J. K.; Fainerman, V. B.; Aksenenko, E. V.; Leser, M. E.; Michel, M.; Miller, R. Adsorption Behaviour of Hen Egg-White Lysozyme at the Air/Water Interface. *Colloid. Surface. A* **2008,** *323*, 167-174.

133. Wayne, R. O. *Light and Video Microscopy*. Academic Press/Elsevier: 2008.

134. Yan, H.; Frielinghaus, H.; Nykanen, A.; Ruokolainen, J.; Saiani, A.; Miller, A. F. Thermoreversible Lysozyme Hydrogels: Properties and an Insight Into the Gelation Pathway. *Soft Matter* **2008,** *4*, 1313-1325.

135. da Silva, M. A.; Areas, E. P. G. Solvent-Induced Lysozyme Gels: Rheology, Fractal Analysis, and Sol-Gel Kinetics. *J. Colloid Interf. Sci.* **2005,** *289*, 394-401.

136. Willmer, D. I.; Baldwin, K. A.; Kwartnik, C.; Fairhurst, D. J. Growth of Solid Conical Structures During Multistage Drying of Sessile Poly(Ethylene Oxide) Droplets. *Phys. Chem. Chem. Phys.* **2010,** *12*, 3998-4004.

137. Baldwin, K. A.; Granjard, M.; Willmer, D. I.; Sefiane, K.; Fairhurst, D. J. Drying and Deposition of Poly(ethylene oxide) Droplets Determined by Peclet number. *Soft Matter* **2011,** *7*, 7819-7826.

138. Bernardin, J. D.; Mudawar, I.; Walsh, C. B.; Franses, E. I. Contact Angle Temperature Dependence for Water Droplets on Practical Aluminum Surfaces. *Int. J. Heat Mass Transfer* **1997,** *40* (5), 1017-1033.

139. Pauchard, L. Influence of Salt Content on Crack Patterns Formed Through Colloidal Suspension Desiccation. *Phys. Rev. E* **1999,** *59* (3).

140. Marin, A. G.; Gelderblom, H.; Lohse, D.; Snoeijer, J. H. Order-to-Disorder Transition in Ring-Shaped Colloidal Stains. *Phys. Rev. Lett.* **2011,** *107*.

141. Esmonde-White, K. A.; Mandair, G. S.; Raaii, F.; Jacobson, J. A.; Miller, B. S.; Urquhart, A. G.; Roessler, B. J.; Morris, M. D. Raman Spectroscopy of Synovial Fluid as a Tool for Diagnosing Osteoarthritis. *J. Biomed. Opt.* **2009,** *14* (3).

142. Cardinaux, F.; Zaccarelli, E.; Stradner, A.; Bucciarelli, S.; Farago, B.; Egelhaaf, S.; Sciortino, F.; Schurtenberger, P. Cluster-driven Dynamical Arrest in Concentrated Lysozyme Solutions. *J. Phys. Chem. B.* **2011,** *115*, 7227-7237.

143. Annarelli, C. C.; Reyes, L.; Fornazero, J.; Bert, J.; Cohen, R.; Coleman, A. W. Ion and Molecular Recognition Effects on the Crystallisation of Bovine Serum Albumin-Salt Mixtures. *Crystal Engineering* **2000,** *3*, 173-194.

144. Lazar, A. N.; Shahgaldian, P.; Coleman, A. W. Anion Recognition Effects in the Structuring of Bovine Serum Albumin Films. *J. Supramol. Chem.* **2001,** *1,* 193-199.

145. Ibanez, L.; Schroeder, W.; Ng, L.; Cates, J.; Consortium, T. I. S.; Hamming, R. The ITK Software Guide, 2003.

146. Daugman, J. Uncertainty Relation for Resolution in Space, Spatial Frequency, and Orientation Optimized by Two-Dimensional Visual Cortical Filters. *J. Opt. Soc. Am. A* **1985,** *2* (7), 1160-1169.

147. Petkov, N. Biologically Motivated Computationally Intensive Approaches to Image Pattern Recognition. *Future Gener. Comp. Sy.* **1995,** *11*, 451-465.

148. Petkov, N.; Kruizinga, P. Computational Models of Visual Neurons Specialised in the Detection of Periodid and Aperiodic Oriented Visual Stimuli: Bar and Grating Cells. *Biol. Cybern.* **1997,** *76*, 83-96.

149. Daugman, J. Demodulation by Complex-Valued Wavelets for Stochastic Pattern Recognition. *Int. J. Wavelets Multi.* **2003,** *1* (1), 1-17.

150. Mallat, S. A Wavelet Tour of Signal Processing: The Sparse Way. 3rd ed.; Academic Press: 2009.